UNIVERSIDADE DE SÃO PAULO
Escola de Engenharia de São Carlos

A constrained minimization theory to prevent self-intersection in hyperelastic solids

Uma teoria de minimização com restrição para impedir auto-intersecção em sólidos hiperelásticos

Lucas Almeida Rocha

Tese de Doutorado do Programa de Pós-Graduação em Engenharia Civil (Engenharia de Estruturas) da Escola de Engenharia de São Carlos, Universidade de São Paulo.

EESC · USP

Lucas Almeida Rocha

A constrained minimization theory to prevent self-intersection in hyperelastic solids

CORRECTED VERSION

The original version is available at the São Carlos School of Engineering

Thesis presented to the São Carlos School of Engineering of the University of São Paulo in partial fulfillment of the requirements for the degree of Doctor of Science in Civil Engineering (Structural Engineering).

Research area: Structures

Advisor: Prof. Dr. Adair Roberto Aguiar

São Carlos

2025

Index card prepared by User Service at “Prof. Dr. Sergio Rodrigues Fontes Library” at EESC/USP

Rocha, Lucas Almeida
R672c A constrained minimization theory to prevent self-intersection in hyperelastic solids / Lucas Almeida Rocha; advisor Adair Roberto Aguiar. -- São Carlos, 2025.

Doctoral (Dissertation) - Graduate Program in Structural Engineering and Research area in Structures -- São Carlos School of Engineering, at University of São Paulo, 2025.

1. Nonlinear elasticity. 2. Orthotropy. 3. Phase-plane analysis. 4. Finite element method. 5. Constrained minimization. I. Título.

Prepared by Eduardo Graziosi Silva- CRB-8/8907

FOLHA DE JULGAMENTO

Candidato: Engenheiro **LUCAS ALMEIDA ROCHA.**

Título da tese: "Uma teoria de minimização com restrição para impedir auto-intersecção em sólidos hiperelásticos".

Data da defesa: 06/03/2025.

Comissão Julgadora	**Resultado**
Prof. Associado Adair Roberto Aguiar (Orientador) (Escola de Engenharia de São Carlos/EESC-USP)	APROVADO
Prof. Dr. Fernando Pereira Duda (Universidade Federal do Rio de Janeiro/UFRJ)	APROVADO
Prof. Dr. Philippe Remy Bernard Devloo (Universidade Estadual de Campinas/UNICAMP)	APROVADO
Prof. Dr. Antônio André Novotny (Laboratório Nacional de Computação Científica/LNCC)	APROVADO
Prof. Dr. Thomas James Pence (Michigan State University/MI-USA)	APROVADO

Coordenador do Programa de Pós-Graduação em Engenharia Civil (Engenharia de Estruturas):
Prof Associado **Ricardo Carrazedo**

Presidente da Comissão de Pós-Graduação:
Prof. Titular **Carlos De Marqui Junior**

ACKNOWLEDGEMENTS

First of all, I would like to thank my parents and my brother for their unconditional support throughout my life.

I am also grateful to my advisor Professor Adair Roberto Aguiar. I deeply appreciate his guidance and the opportunity to work with him.

My friends deserve my gratitude for all the discussions we had as well as distractions that made these past years much more pleasant.

I express my gratitude to the staff of the Department of Structural Engineering of EESC/USP for the assistance provided.

Last but not least, I acknowledge the financial supporters of this work. This study was financed in part by the Coordenação de Aperfeiçoamento de Pessoal de Nível Superior – Brasil (CAPES) – Finance Code 001 and by the São Paulo Research Foundation (FAPESP), grant n° 2022/07083-8.

ABSTRACT

Rocha, L. A. **A constrained minimization theory to prevent self-intersection in hyperelastic solids**. 2025. Thesis (PhD) - São Carlos School of Engineering, University of São Paulo, São Carlos, 2025.

The classical linear elasticity theory predicts self-intersection in the neighborhood of interior points of anisotropic solids, crack tips, and corners. This physically unrealistic behavior is characterized by the violation of the local injectivity condition $J > 0$, where J is the determinant of the deformation gradient. One way to impose this condition consists of minimizing the total potential energy of an elastic solid subjected to the constraint $J \geq \varepsilon > 0$, where ε is a small positive parameter. In the context of the classical linear elasticity theory, this approach was successfully used to eliminate the anomalous self-intersecting behavior. The resulting constrained linear theory gives rise to large deformations inside the solid, which is in contradiction to the basic assumption of infinitesimal strains of the classical linear theory. In this work, we present a constrained minimization theory for hyperelastic solids undergoing finite deformations and derive necessary conditions for a deformation field to be a minimizer. We then apply this formulation in the analysis of equilibrium of an annular disk made of an orthotropic St Venant-Kirchhoff material. This material is a natural constitutive extension of its classical linear counterpart. The disk is fixed on its inner surface and compressed by a constant pressure on its outer surface. The analysis of equilibrium of a solid disk is obtained by letting the inner radius tend to zero. The disk problem is formulated as both a boundary value problem (disk BVP) and a minimization problem (disk MP), and these problems are solved in the context of both the classical nonlinear theory, for which the condition $J > 0$ is not imposed, and the constrained nonlinear theory, for which $J > 0$ is imposed. In the context of the classical nonlinear theory, we find that there is a critical pressure $\bar{p}$, which tends to zero as the inner radius of the disk tends to zero, above which a solution of either problem becomes non-smooth and predicts $J \leq 0$. In addition, $\bar{p}$ is smaller than its counterpart from the classical linear theory and, therefore, serves as an upper bound below which this linear theory is valid. In the context of the constrained nonlinear theory, the solutions of both the disk BVP and MP agree very well and satisfy all the necessary conditions for a minimizer, including the injectivity condition. Finally, these results are also in very good agreement with their counterpart obtained in the context of the classical nonlinear elasticity for a disk made of an orthotropic and compressible Mooney-Rivlin material; in particular, when the parameter ε tends to zero.

Keywords: Nonlinear elasticity. Orthotropy. Phase-plane analysis. Finite element method. Constrained minimization.

RESUMO

Rocha, L. A. **Uma teoria de minimização com restrição para impedir auto-intersecção em sólidos hiperelásticos**. 2025. Tese (Doutorado) - Escola de Engenharia de São Carlos, Universidade de São Paulo, São Carlos, 2025.

A teoria de elasticidade linear clássica prediz auto-intersecção em vizinhanças de pontos interiores de sólidos anisotrópicos, em pontas de trincas e em cantos. Esse comportamento fisicamente inadmissível é caracterizado pela violação da restrição de injetividade local $J > 0$, em que J é o determinante do gradiente de deformação. Uma forma de impor essa condição consiste em minimizar o potencial total de energia de um sólido elástico sujeito à restrição $J \geq \varepsilon > 0$, em que ε é um parâmetro pequeno e positivo. No contexto da teoria de elasticidade linear clássica, essa abordagem foi utilizada para eliminar com sucesso a auto-intersecção. Essa teoria linear com restrição resulta em deformações elevadas o que contradiz a hipótese básica de deformações infinitesimais da teoria linear clássica. Neste trabalho, apresentamos uma teoria de minimização com restrição para sólidos hiperelásticos sujeitos a deformações finitas e obtemos condições necessárias para que um campo de deformação seja um minimizador. Aplicamos essa formulação na análise do equilíbrio de um disco anelar feito de um material de St Venant-Kirchhoff ortotrópico. Esse material corresponde a uma extensão natural de um material elástico linear. A superfície interna do disco está fixa e a externa está comprimida por uma pressão uniforme. A análise de equilíbrio de um disco sólido é obtida no caso limite do raio interno tendendo a zero. O problema do disco é formulado como um problema de valor de contorno (PVC do disco) e um problema de minimização (PM do disco). Esses problemas são resolvidos no contexto da teoria de elasticidade não linear clássica, em que $J > 0$ não é imposto, e da teoria não linear com restrição, em que $J > 0$ é imposto. No contexto da elasticidade não linear clássica, determinamos uma pressão crítica $\bar{p}$, que tende a zero à medida que o raio interno tende a zero, acima do qual as soluções de ambos os problemas se tornam não suaves e predizem $J \leq 0$. $\bar{p}$ é menor que seu valor correspondente predito pela elasticidade linear clássica e, portanto, é um limite superior abaixo do qual a teoria linear é válida. No contexto da teoria não linear com restrição, as soluções do PVC e do PM do disco estão de muito bom acordo e satisfazem todas as condições necessárias para mínimo, incluindo a condição de injetividade local. Por fim, esses resultados também estão de muito bom acordo com resultados análogos obtidos no contexto da teoria de elasticidade não linear clássica para um disco feito de um material de Mooney-Rivlin compressível e ortotrópico; em particular, quando o parâmetro ε tende a zero.

Palavras-chave: Elasticidade não linear. Ortotropia. Análise de plano de fase. Método dos elementos finitos. Minimização com restrição.

LIST OF FIGURES

CONTENTS

1 INTRODUCTION

1.1 Presentation and motivation

We are interested in singular points where there is an abrupt change of geometry, material properties, and boundary conditions. Crack tips, points on the interface between different materials, and interior points in anisotropic solids are typical examples of singular points. From an experimental point of view, large values of stress may occur in these points and cause the growth of cracks and debonding of interfaces between different materials, such as those found in films and substrates or welding and bimetallic joints. From a theoretical point of view, the linear elasticity theory may predict self-intersection, or material overlapping, in a neighborhood of the singular points, which is not physically admissible.

Fosdick and Royer-Carfagni (2001) proposed a constrained minimization theory, which is based on the minimization of the total potential energy functional $\mathcal{E}$ of the classical linear elasticity theory subjected to the constraint $J > 0$, where J is the determinant of the deformation gradient. This constrained minimization theory can properly represent the nonlinear constraint $J > 0$, whose imposition gives rise to reactive forces that prevent the material from overlapping itself. However, self-intersection is associated with large deformations that violate the hypothesis of infinitesimal strains upon which the linear elasticity theory is based. Therefore, in this work, we extend this constrained theory to the nonlinear elasticity theory by considering $\mathcal{E}$ as the total potential energy of a hyperelastic material.

We apply this theory to a relevant problem in engineering that has a non-homogeneous solution and, yet, is amenable to analysis. The problem consists of an elastic annular disk with uniform thickness in equilibrium in the absence of body force. The disk is fixed on its inner surface of radius $R_i \geq 0$ and compressed by a constant and uniform pressure $p > 0$ on the deformed configuration of its outer surface of radius $R_e > R_i$. The disk is made of an orthotropic material.

In the context of the classical linear elasticity theory, the solution of the disk problem is unique and, for $R_i = 0$, predicts that the stresses go monotonically to minus infinity as we approach the center of the disk, even for small values of p, when the stiffness in the radial direction is greater than the stiffness in the tangential direction (Lekhnitskii, 1968). This type of material property is found in carbon fibers with radial microstructure (Christensen, 1994) and in certain types of wood (Forest Products Laboratory, 2010).

Fosdick and Royer-Carfagni (2001) found that, in addition to stress singularities, Lekhnitskii's solution predicts self-intersection in a neighborhood of the center of the disk.

To prevent this anomalous behavior, the authors minimize the total potential energy of the linear elasticity theory subjected to the local injectivity condition $J > 0$. The authors found an analytical solution that does not exhibit self-intersection. Later, Aguiar, Fosdick and Sanchez (2008) considered the case $R_i > 0$ and showed that the solution of the linear elasticity theory predicts self-intersection if the pressure is greater than a certain value. Then, in the context of the constrained minimization theory of Fosdick and Royer-Carfagni (2001), the authors obtained an analytical solution that does not predict this anomalous behavior. They also proposed a numerical method based on a penalty formulation, which can be used to treat more general problems, and obtained sequences of numerical solutions that converge to the analytical solution.

The solutions reported above correspond to radial displacements only. However, in view of the constraint $J > 0$, the constrained minimization theory is highly nonlinear and may predict more than one solution. Fosdick, Freddi and Royer-Carfagni (2008) and Aguiar and Rocha (2021) considered the case $R_i = 0$ and obtained numerical and analytical solutions corresponding to a displacement field having both radial and tangential displacements not null. In addition, this secondary solution corresponds to a lower energy level when compared to the primary solution, which has null tangential displacements.

In the context of the nonlinear elasticity theory, Antman and Negrón-Marrero (1987) studied the disk problem in the case $R_i = 0$ and showed that, for a certain class of materials, the stress goes monotonically to minus infinity at the center of the disk if the material is radially reinforced. This result indicates that the stress singularity observed in the Lekhnitskii's solution is not an artifact of the linear elasticity theory, but it is intrinsic to radially reinforced materials.

In Chapter 3, we extend the constrained minimization theory of Fosdick and Royer-Carfagni (2001) to the nonlinear elasticity theory. In Chapter 4, we study the disk problem in the context of the classical nonlinear elasticity theory, that is, we do not impose the local injectivity condition. We use an orthotropic St Venant-Kirchhoff material model, which corresponds to a natural constitutive extension of the linear to the nonlinear elasticity theory and a first-order approximation of hyperelastic materials with the same material symmetry. For comparison purposes, we also consider an orthotropic and compressible Mooney-Rivlin material.

In Chapter 5, we use the constrained nonlinear theory developed in Chapter 3 to impose the local injectivity condition $J > 0$ in the disk problem using the orthotropic St Venant-Kirchhoff model. We obtain physically plausible solutions, which are in very good agreement with the solutions obtained with the orthotropic and compressible Mooney-Rivlin material. It is known that penalty formulations are susceptible to numerical errors caused by ill-conditioned systems. For this reason, we impose the constraint $J > 0$ using both penalty and augmented Lagrangian formulations and compare the results obtained

from both formulations. In Chapter 6, we present some concluding remarks and ideas for future investigations.

1.2 Objectives

We use analytical and numerical methods to investigate the mechanical behavior of anisotropic elastic solids near singular points. In particular, we extend our studies of the constrained minimization theory based on the classical linear elasticity to the nonlinear elasticity theory. As an example of application, we investigate the equilibrium problem of an annular disk with uniform thickness in the absence of body force. The disk is fixed on its inner surface of radius R_i and is compressed by a uniform pressure p on the deformed configuration of its outer surface of radius R_e. The disk is made of an orthotropic material, that is stiffer in the radial direction than in the tangential direction. Below we list some specific objectives.

1. Determine necessary conditions that a minimizer of the total potential energy functional of an hyperelastic material subjected to the local injectivity constraint must satisfy. These conditions are compared with those obtained by Fosdick and Royer-Carfagni (2001) for a linear elastic material.

2. Use an orthotropic St Venant-Kirchhoff model to investigate the disk problem. We obtain results that can be compared with results reported by Aguiar, Fosdick and Sanchez (2008) in the context of the classical linear elasticity theory. In Section 4.3, we find that there is a pressure $\bar{p}$ above which the solution of the disk problem predicts self-intersection and a jump in the deformation gradient.

3. Impose the local injectivity constraint $J > 0$ in the orthotropic St Venant-Kirchhoff model to obtain solutions of the disk problem that do not predict self-intersection for any value of p. For that, we use both a penalty and an augmented Lagrangian formulation, and compare the results obtained with both formulations. We obtain physically plausible deformation fields, which may not be smooth.

4. Use an alternative hyperelastic model with a strain energy function that goes to infinity as $J \to 0$; more specifically, a compressible Mooney-Rivlin material extended to the orthotropic case. We obtain solutions that do not violate the injectivity constraint and compare them with the corresponding results of the previous specific objective.

1.3 Structure of the thesis

In Chapter 2, we review the literature on the disk problem in the context of both linear and nonlinear elasticity theories, where, for the former, we include results concerning

the imposition of the constraint $J > 0$. In view of the non-smoothness found in the solution of the disk problem, which is presented in Section 4.3, we also review works that deal with topics such as ellipticity conditions and non-monotonic stress-strain relations.

In Chapter 3, we present background material on concepts of continuum mechanics and nonlinear elasticity theory that are relevant in this work. In addition, we extend the constrained minimization theory to the nonlinear case. We derive necessary conditions for a deformation field to be a minimizer of the energy functional, which include traction continuity and dissipation-free conditions across a surface of discontinuity of the deformation gradient.

In Chapter 4, we present results concerning the disk problem in the context of the classical nonlinear elasticity theory. In Section 4.1, we formulate the disk problem as both boundary value and minimization problems. In Section 4.2, we investigate some constitutive aspects and apply some of the results presented in Chapter 3 regarding the ellipticity of the equilibrium equations and the stability of non-smooth deformation fields. In Section 4.3, we study the disk boundary value problem using a phase-plane technique. We find that there is a value of pressure $\bar{p}$ above which the solution of the disk problem is non-smooth and predicts self-intersection. In Section 4.4, we solve the disk minimization problem using standard tools of nonlinear programming. In view of the discontinuity of the deformation gradient, we include the position of the discontinuity as a variable of the problem in addition to the degrees of freedom of the displacement field.

In Chapter 5, we apply the constrained nonlinear theory to the disk problem. In Section 5.1, we formulate the constrained disk problem as both boundary value and minimization problems. In Section 5.2, we adapt the phase-plane technique of Section 4.3 to the constrained nonlinear theory. In addition, we study the constrained disk boundary value problem analytically in the region where the constraint is active. In Section 5.3, we adapt the numerical procedure of Section 4.4 to impose the local injectivity constraint. We use and compare both penalty and augmented Lagrangian formulations. In addition, we find that the classical nonlinear elasticity and the constrained nonlinear theory yield solutions that are in very good agreement.

In Chapter 6, we present some final considerations, including topics for further investigations.

2 LITERATURE REVIEW

In this chapter, we review the literature on the constrained minimization theory, the disk problem in the context of both the linear and nonlinear theory of elasticity, and constitutive relations considered in this work.

In the context of the classical linear elasticity theory, Lekhnitskii (1968) studied the problem of a homogeneous cylindrically orthotropic disk in equilibrium without body force and compressed along its boundary by a uniform pressure. The author obtained a solution that predicts stress singularity in the center of the disk for any value of pressure when the elastic constant in the radial direction is greater than the elastic constant in the tangential direction. This type of material property is found in carbon fibers with radial microstructure (Christensen, 1994), fiber-reinforced composites (Daniel; Ishai, 2006), and some types of wood (Forest Products Laboratory, 2010).

Carbon fibers and fiber-reinforced composites are employed by many industries, such as aerospace, automotive, construction, energy, medical, and sport industries, because of their mechanical, thermal, and electrical properties. Stiffer response in the radial direction than in the tangential direction is obtained by the alignment of stiff fibers along the radial direction in the case of fiber-reinforced composites (Daniel; Ishai, 2006). For carbon fibers, such a relation is obtained from the alignment of the basal planes of the graphite crystals along the radial direction (Huang, 2009; Christensen, 1994).

The Lekhnitskii's solution predicts not only stress concentration but also self-intersection, as shown by Fosdick and Royer-Carfagni (2001). More precisely, there is a region around the center of the disk where the determinant of the deformation gradient is not positive, which, of course, has no physical meaning. One way to prevent self-intersection in elasticity consists of treating the local injectivity condition $\det \mathbf{F} > 0$, where $\mathbf{F}$ is the deformation gradient, via convexity and coercivity conditions that entail unbounded growth of energy as $\det \mathbf{F}$ approaches zero. For nonlinear elastic materials and provided that these conditions hold, Ball's theorem (Ball, 1976; Ciarlet, 1988) guarantees the existence of minimizers of the total potential energy that satisfy $\det \mathbf{F} > 0$.

Fosdick and Royer-Carfagni (2001) took another route and proposed a constrained minimization theory according to which the displacement field is determined by minimizing the total potential energy of the classical linear elasticity theory subjected to the constraint that the determinant of the deformation gradient must not be less than a small positive parameter. The authors proved an existence theorem for such minimizers and obtained a solution for the Lekhnitskii's disk problem that does not predict self-intersection.

Aguiar, Fosdick and Sanchez (2008) investigated the Lekhnitskii's disk problem

in the case of a disk that has a concentric circular opening of radius R_i. In the context of the classical linear elasticity theory, the authors found that, even though the stresses remain bounded, the solution of this problem predicts self-intersection near the inner radius if the pressure applied on the outer radius is large enough. Then, the authors considered this problem in the context of the constrained minimization theory of Fosdick and Royer-Carfagni (2001) and determined an analytical solution that does not predict self-intersection. The authors also obtained sequences of numerical solutions that converge to this analytical solution. Two different numerical procedures based on interior and exterior penalty formulations were used. The former constructs a sequence of functions that approaches the solution from within the set of admissible solutions, whereas, in the latter, the corresponding sequence approaches the solution from the outside of the admissible set.

Obeidat *et al.* (2001) proposed a numerical approach based on the variational form of the equilibrium equation of the solid disk problem. They solved this problem using a carefully designed algorithm that is difficult to implement when the region where the constraint is active is not known in advance. The interior penalty formulation was introduced by Aguiar (2006) in the solution of the problem of a spherically anisotropic solid sphere subjected to a uniform pressure in the context of the constrained minimization theory. In the context of the classical linear elasticity, this problem may also predict self-intersection, as reported by Ting (1998).

In the works mentioned above, the authors searched for a *radially symmetric* displacement field, in the sense that, it has only the radial component and it depends only on the radius. In the classical linear elasticity theory, this solution is unique; in the context of the in constrained minimization theory, however, it may not be so.

Fosdick, Freddi and Royer-Carfagni (2008) used a bi-dimensional finite element mesh and the penalty formulation of Aguiar (2006) to present a numerical solution, in the context of the constrained minimization theory, that does not predict overlapping and is not radially symmetric. When the shearing modulus is sufficiently small, there is a secondary solution that bifurcates from the radially symmetric solution obtained by Fosdick and Royer-Carfagni (2001). There is a region around the center of the disk where undeformed radial lines are deformed into spiral lines. The authors, however, did not present convergence results.

Recently, Aguiar and Rocha (2021) investigated the non-uniqueness of the solution of Lekhnitskii's problem in the context of the constrained minimization theory. The authors used a semi-analytic approach to obtain a *rotationally symmetric* solution, in the sense that, the displacement field depends only on the radius and has both radial and tangential components. This solution has similarities with the computational results of Fosdick, Freddi and Royer-Carfagni (2008), such as the rotation of a central region of the solid, but

also some differences; for instance, in the rotationally symmetric solution, the tangential displacement is a linear function of the radius near the center of the disk. Aguiar and Rocha (2021) also used sequences of bi-dimensional finite element meshes to obtain numerical solutions that converge to the rotationally symmetric solution.

We see from above that the imposition of the local injective constraint using a linearly elastic material induces reactive internal forces that prevent the solid from intersecting itself. Self-intersection, however, is associated with large strains, which contradicts the basic assumption of infinitesimal strains of the linear elasticity theory. Therefore, it is natural to study the disk problem in the context of the nonlinear elasticity theory.

Antman and Negrón-Marrero (1987) considered the problem of a cylindrically anisotropic solid cylinder subjected to a uniform pressure on its outer radius in the context of the nonlinear elasticity theory. Under some physically motivated assumptions for the response of the material, the authors show that the stress is a monotonic function of the radius and goes to minus infinity at the center of the cylinder if the material is radially reinforced. Therefore, the unbounded stress predicted by the Lekhnitskii's solution is not an artifact of the linear theory, but intrinsic to radially reinforced materials. To obtain this result, the authors rewrote the equation of equilibrium as a system of autonomous equations and used a phase-plane technique to study the solutions of the considered problem. In Sections 4.3 and 5.2.2, we use a similar technique to find the solution of the disk problem.

Stepanov and Antman (2016) studied radially symmetric deformations in annular cylinders and spherical shells. The authors used different mathematical tools, such as phase-plane analysis, direct methods of the calculus of variations, fixed-point theorems, and global continuation methods to investigate the existence, multiplicity, and qualitative behavior of solutions when the solid is subjected to different types of boundary conditions. The authors pointed out the advantages and disadvantages of each mathematical tool. For the considered problems, the phase-plane technique provided detailed qualitative behavior, addressing questions regarding the existence and uniqueness of solutions and the presence of extrema of strain and stress. As a disadvantage, the phase-plane technique is limited to homogeneous materials, unless a more complex version of the method is used.

A topic of great importance in the nonlinear elasticity theory is the ellipticity of the equilibrium equations. In the linear elasticity theory, ellipticity is guaranteed if the material constants satisfy certain relations such as, in the isotropic case, $\mu > 0$ and $\Lambda + 2\,\mu > 0$, where Λ e μ are the first and second Lamé constants, respectively (Gurtin, 1973). In the nonlinear elasticity theory, ellipticity conditions depend on both the material constants and the deformation.

Aguiar (2019) obtained necessary and sufficient conditions for the strong ellipticity of the equilibrium equations governing finite plane deformations of a class of orthotropic

and compressible hyperelastic solids. The ellipticity conditions of the classical linear elasticity theory of orthotropic solids were recovered as a particular case.

Merodio and Ogden (2005) studied the loss of ellipticity of the equations of equilibrium for fiber-reinforced nonlinear elastic materials. The authors associated fiber failure with the loss of ellipticity. El Hamdaoui, Merodio and Ogden (2015) studied the equilibrium of a circular cylindrical tube made of a fiber-reinforced nonlinear elastic material that undergoes certain combinations of axial stretch, inflation, and helical shear deformations. The authors used a neo-Hookean isotropic model augmented by a standard reinforcement model, which accounts for fiber stretching only. In the case of a cylinder reinforced with radial fibers under inflation, the authors concluded that the stronger the anisotropy, the smaller the deformation required for loss of ellipticity. El Hamdaoui, Merodio and Ogden (2018) replaced the standard reinforcement model with a model that, in addition to fiber stretching, also accounts for fiber shearing. In the case of radial fibers, the authors showed that shearing delays the loss of ellipticity associated with fiber contraction.

Merodio, Saccomandi and Sgura (2007) used the neo-Hookean and standard reinforcement models to study the problem of rectilinear shear of a fiber-reinforced slab. The authors found that the deformation gradient has a finite jump discontinuity in an interior surface of the slab when the amount of shear is sufficiently large and contracts the fibers. At this discontinuity, the leading term of the equilibrium equation is null, and the second derivative of the displacement is unbounded. The loss of ellipticity was also verified. As noted by Baek and Pence (2010), in this situation, the fiber goes through three different stages of deformation as the shear increases. First, it shortens until it reaches a minimum length, then it relaxes until it recovers its original length, and finally, it elongates. In the second state, the energy stored in the fibers is released, which may cause the shear stress to be a non-monotonic function of the amount of shear.

Both loss of ellipticity and non-monotonic stress-strain relations are associated with discontinuous deformation gradients. Knowles and Sternberg (1978) and Gurtin (1986) showed that the loss of ellipticity of the equilibrium equations at some deformation is a necessary condition for the existence of a deformed state with a finite jump in its gradient. Ericksen (1975) considered the problem of equilibrium of a unidimensional bar made of a material with a non-monotonic stress-strain relation. The author showed that this kind of constitutive relation results in a problem with infinite solutions because the strain at any point of the bar may assume more than one value. An energy criterion was used to render the solution unique for all, except one critical value of loading for which the strain in the bar can assume two different values, which correspond to two equally stable deformed states according to the adopted energy criterion.

Abeyaratne (1981) studied the problem of an annular cylinder fixed on its outer

surface and subjected to a prescribed twist ϕ_0 on its inner surface. The cylinder is made of an incompressible isotropic material with a non-monotonic relation between shear stress and the amount of shear. The author showed that there are values $0 < \phi_1 < \phi_2 < \phi_3 < \phi_4 < \phi_5 < \phi_6$ such that: (i) if $|\phi_0| \in (0, \phi_1) \cup (\phi_6, \infty)$, there is a unique solution, which is smooth, (ii) if $|\phi_0| \in (\phi_2, \phi_3) \cup (\phi_4, \phi_5)$, there is an infinite number of solutions, which are all non-smooth, and (iii) if $|\phi_0| \in (\phi_1, \phi_2) \cup (\phi_3, \phi_4) \cup (\phi_5, \phi_6)$, there is an infinite number of solutions, one of which is smooth whereas the others are non-smooth. The author has used an energy minimization criterion to render the solution unique for $|\phi_0| \in (\phi_1, \phi_6)$. The corresponding deformation gradient is continuous everywhere, except at a cylindrical surface internal to the cylinder, where it has a finite jump. Abeyaratne (1983) obtained necessary conditions for a non-smooth deformation field to be a minimizer of the total potential energy functional, which include continuity conditions across the surface of discontinuity of the deformation gradient.

Fosdick and Macsithigh (1986) investigated a problem similar to that of Abeyaratne (1981). The authors adopted a more general form for the displacement field and formulated the problem as a minimization problem. The authors found that the minimizer may have a finite jump in its gradient in a cylindrical surface internal to the cylinder if the twist belongs to a certain interval. Tommasi *et al.* (2001) also used a minimization approach to study non-smooth deformation fields in solids. The authors considered the problem of a rectangular cylinder subjected to dead-load surface traction composed of an incompressible isotropic material similar to that of Fosdick and Macsithigh (1986). They showed that the stable deformation field may be non-smooth depending on the applied surface forces.

A non-monotonic relation between stress and strain can model crystalline materials that may exist in more than one crystal structure, which is referred to as phase. Examples of such materials include the shape memory alloy NiTi, the ferroelectric alloy $BaTiO_3$, the ferromagnetic alloy FeNi, and the high-temperature superconducting ceramic alloy $ErRh_4B_4$. In this type of material, changes in the temperature and stress conditions can transform the material abruptly into a different phase. In the context of thermal variations, the phase preferable at low temperatures is called the martensitic phase, and the one preferable at high temperatures is called the austenitic phase. In the context of stress variations, the phases are referred to as low and high strain phases. In addition, these solid-solid transformations represent a particular case of more general phase transitions, which also include, for instance, liquid-solid transformations such as in a solidification process. (Abeyaratne; Knowles, 2006).

Non-monotonic stress-strain relations are also used to model strain localization associated with plasticity. Froli and Royer-Carfagni (2000) proposed a unidimensional model composed of elementary units. These units are composed of springs and frictional sliding blocks in such a way that the force-displacement response of the unit is non-

monotonic. The authors used this model to numerically reproduce their experimental results obtained previously (Froli; Royer-Carfagni, 1999) by carrying out a displacement-controlled tensile test on a steel bar. Froli and Royer-Carfagni (1999) used strain gauges along the bar to measure the local strain at different positions. The average stress-strain curve was also plotted. The authors identified three different stages as the load increases. First, all gauges recorded the same local strain and the average stress-strain response was linear. Then, the gauges gradually recorded finite jumps in the local strain followed by an approximately constant local strain. This second stage corresponds to the plastic plateau of the average stress-strain curve. Then, in the third stage, the recorded local strains increased again.

From the above discussion, we see that the choice of the material model is not trivial in the nonlinear elasticity theory. One of the simplest models is the St Venant-Kirchhoff material, which is isotropic and corresponds to a linear relation between the second Piola-Kirchhoff stress tensor and the Green-St Venant strain tensor.

Batra (2001) studied the behavior of the St Venant-Kirchhoff model under different homogeneous deformations. In simple extension, the relation between the axial load and the axial stretch ϵ is non-monotonic with an extremum point at $\epsilon = \sqrt{3}/3$, independently of the material constants. The load-stretch curves resulting from the biaxial and triaxial loading of a membrane and a cube, respectively, also present an extremum point at $\epsilon = \sqrt{3}/3$. In the case of simple shear, the shear stress monotonically increases with the shear strain.

The classical St Venant-Kirchhoff material, which is isotropic, can be extended to the anisotropic case. According to Bonet and Burton (1998), the anisotropic St Venant-Kirchhoff material model is simple to implement in finite element codes. However, as indicated by a numerical experiment, it is not adequate for problems involving large deformations since the determinant of the deformation gradient may assume negative values. This is expected since the strain energy function of this material remains finite as the determinant of the deformation gradient tends to zero. Nevertheless, this material is commonly used in the literature. Lewandowski and Stupkiewicz (2018) studied the wedge indentation of a single nickel crystal using a crystal plasticity model, whose elastic response is governed by an anisotropic St Venant-Kirchhoff model. This material model was also used by Yamashita, Jayakumar and Sugiyama (2016) to study the multi-layer fiber-reinforced rubber for steel belt and carcass layers in tires, by Eik, Puttonen and Herrmann (2015) to study constitutive relations for steel fiber reinforced concrete, and by Vu-Quoc and Tan (2003) to model the behavior of multilayered composites. Arndt *et al.* (2006) compared experimental results of compression tests on NiMnGa single crystals with numerical results. To model the martensitic transformation in the crystal, the authors used a free energy composed of the strain energy function of the anisotropic St Venant-Kirchhoff model and a term that depends on the temperature.

Materials that are more adequate to model large deformations must satisfy some growth conditions that are associated with the idea that extreme deformations must correspond to extreme stresses. A way of defining anisotropic hyperelastic models consist of defining its strain energy function W as the sum of both an isotropic and an anisotropic part, that is, $W = W_{\text{iso}} + W_{\text{aniso}}$. For W_{iso}, it is common to adopt the strain energy function of an isotropic material, such as the Neo-Hookean or the Mooney-Rivlin material, since they have appropriate growth properties. For W_{aniso}, it depends on the material symmetry; we comment on some models of the literature for transversely isotropic materials.

Bonet and Burton (1998) defined a transversely isotropic material as a compressible Neo-Hookean material augmented with the anisotropic part of a transversely isotropic St Venant-Kirchhoff material. In their studies, this material yielded physically plausible results in simulations where the St Venant-Kirchhoff material did not. In addition, its isotropic part can be replaced with more complex models, such as a Mooney-Rivlin or an Ogden material. In Section 3.3, we use this approach to define an orthotropic and compressible Mooney-Rivlin material.

Another common choice for W_{aniso} is the standard reinforcement model, which is a simple model that accounts only for the stretch in the direction of the symmetry of the material. Thinking of transversely isotropic materials as composites made of a matrix reinforced with uni-directional fibers, the standard reinforcement model is associated with the idea that the contribution of the fibers comes from their stretch only. Although the simplicity of this model allows for more analytical calculations, Murphy (2013) noted that this model imply that, for infinitesimal deformations, the shear moduli in the direction of the fiber and perpendicular to the fiber are the same if we assume that the undeformed reference configuration is stress-free. This relation is not observed for transversely isotropic materials, such as some soft tissues and fiber-reinforced composites, as can be seen from Tables 1 and 2 of Murphy (2013) and Table A.6 of Daniel and Ishai (2006).

It is also possible to define models based on some particular properties. For instance, Ball's theorem (Ball, 1976; Ciarlet, 1988) proves the existence of solutions for displacement-traction problems provided that the strain energy function is polyconvex and satisfy some growth conditions. Itskov and Aksel (2004) defined a class of transversely isotropic models that satisfies these properties. Schröder and Neff (2003) (see also Schröder (2010)) proposed a simple way to create polyconvex strain energy functions. These models yield stress-strain relations that are more complex to handle analytically than the models mentioned previously. In addition, for these models to be polyconvex, its material parameters, which are related to the elastic constants of the classical linear elasticity, must satisfy some relations. These relations are not satisfied for any plausible elastic constants.

In this work, we propose a constrained minimization theory in nonlinear elasticity, which represents an extension of the constrained minimization theory of Fosdick and Royer-

Carfagni (2001), who have used the generalized Hooke's law. We determine necessary conditions that a minimizer must satisfy and, as an example of application, we consider the equilibrium problem of an annular disk made of an orthotropic St Venant-Kirchhoff material under external pressure. In Section 4.2, we show that the relation between the radial normal stress and the radial stretch may be non-monotonic, in analogy to the non-monotonic behavior reported by Batra (2001) with the isotropic St Venant-Kirchhoff material. In Section 4.3, we will see that, when the pressure exceeds a critical value, the solution of the disk problem predicts self-intersection and a jump discontinuity in the deformation gradient. Self-intersection is an unphysical behavior that will be removed when we impose the local injectivity constraint. Jump discontinuity creates numerical difficulties that require special numerical strategies. In this work, we present two strategies, one of which is based on solving the equilibrium equations using a phase-plane technique adapted from the works of Antman and Negrón-Marrero (1987) and Stepanov and Antman (2016), whereas the other strategy is based on searching a minimizer of the energy functional using the finite element method together with standard nonlinear programming tools. In addition, in Section 5.3.2, we compare the results obtained from the constrained minimization theory with those obtained with an orthotropic and compressible Mooney-Rivlin material with no imposition of the local injectivity constraint. We will see that both solutions are in very good agreement with each other.

3 THEORETICAL BACKGROUND

In this chapter, we present some background material about continuum mechanics and the nonlinear theory of elasticity. We begin by presenting results regarding body and surface forces. Next, we introduce the balance laws and the constitutive assumptions used to model elastic materials. We also present the typical form of a boundary value problem of elasticity and conditions for the strong ellipticity of the governing equations. Finally, we study the constrained nonlinear theory mentioned in the previous chapters.

3.1 Applied forces

Let $\mathcal{B} \subset \mathbb{R}^3$ be the undistorted reference configuration of a solid body. Material points $\mathbf{x} \in \mathcal{B}$ are mapped into spatial points $\mathbf{y} \in \mathbb{R}^3$ by the deformation field $\mathbf{f} : \mathcal{B} \to \mathbb{R}^3$, that is, $\mathbf{y} = \mathbf{f}(\mathbf{x}) \in \mathbf{f}(\mathcal{B}) \subset \mathbb{R}^3$, where $\mathbf{f}(\mathcal{B})$ denotes the deformed configuration of the solid. A body force per unit of deformed volume $\mathbf{b_f} : \mathbf{f}(\mathcal{B}) \to \mathbb{R}^3$ is applied to the body. We associate to this field a body force per unit of undeformed volume $\mathbf{b} : \mathcal{B} \to \mathbb{R}^3$ given by

$$\mathbf{b}(\mathbf{x}) = \det \mathbf{F}(\mathbf{x})\, \mathbf{b_f}(\mathbf{y})\,, \qquad \mathbf{y} = \mathbf{f}(\mathbf{x})\,, \tag{3.1}$$

where $\mathbf{F}(\mathbf{x}) \triangleq \nabla \mathbf{f}(\mathbf{x})$ and ∇ is the gradient operator with respect to $\mathbf{x}$. Since $\det \mathbf{F}$ is the ratio between an infinitesimal volume element in the deformed configuration and its respective value in the reference configuration, it is usual to assume that $\mathbf{F} \in \mathrm{Lin}^+ \triangleq \{\mathbf{A} \in \mathrm{Lin} \,|\, \det \mathbf{A} > 0\}$, where Lin is the space of the linear transformations $\mathbf{A} : \mathbb{R}^3 \to \mathbb{R}^3$. However, when solving problems, such a constraint is usually not imposed but only verified a posteriori.

We denote $\partial\mathcal{B}$ as the boundary of $\mathcal{B}$, which is composed of two parts, $\partial_1\mathcal{B}$ and $\partial_2\mathcal{B}$, such that $\partial\mathcal{B} = \partial_1\mathcal{B} \cup \partial_2\mathcal{B}$ and $\partial_1\mathcal{B} \cap \partial_2\mathcal{B} = \emptyset$. In $\partial_1\mathcal{B}$, the deformation is known and given by

$$\mathbf{f}(\mathbf{x}) = \bar{\mathbf{f}}(\mathbf{x})\,, \qquad \mathbf{x} \in \partial_1\mathcal{B}\,. \tag{3.2}$$

In $\mathbf{f}(\partial_2\mathcal{B})$, we apply a surface force per unit of deformed area $\mathbf{t_f} : \mathbf{f}(\partial_2\mathcal{B}) \to \mathbb{R}^3$. We associate to this field a surface force per unit of undeformed area $\mathbf{t} : \partial_2\mathcal{B} \to \mathbb{R}^3$ given by

$$\mathbf{t}(\mathbf{x}) = \det \mathbf{F}(\mathbf{x})\, |\mathbf{F}(\mathbf{x})^{-T}\, \mathbf{N}|\, \mathbf{t_f}(\mathbf{y})\,, \qquad \mathbf{y} = \mathbf{f}(\mathbf{x})\,, \tag{3.3}$$

where $\mathbf{N}$ is the unit outer normal vector to $\partial_2\mathcal{B}$ at $\mathbf{x}$. In Figure 1, we show an illustration of the reference configuration and the applied forces.

In this work, we consider that the body and surface forces have the forms given by

$$\mathbf{b}(\mathbf{x}) = \hat{\mathbf{b}}(\mathbf{x}, \mathbf{f}(\mathbf{x}))\,, \tag{3.4}$$

Figure 1 – The reference configuration and the applied forces.

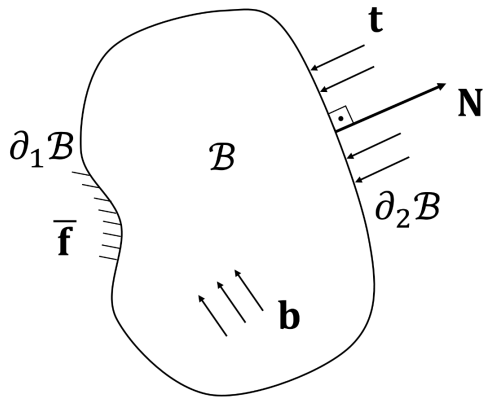

Source: The author.

$$\mathbf{t}(\mathbf{x}) = \hat{\mathbf{t}}(\mathbf{x}, \mathbf{F}(\mathbf{x}))\,, \tag{3.5}$$

respectively, where $\hat{\mathbf{b}} : \mathcal{B} \times \mathbb{R}^3 \to \mathbb{R}^3$ and $\hat{\mathbf{t}} : \partial_2\mathcal{B} \times \mathrm{Lin}^+ \to \mathbb{R}^3$. We also consider that both $\mathbf{b}$ and $\mathbf{t}$ are conservative. For $\mathbf{b}$, this means that there is a functional $B : \{\mathbf{f} : \mathcal{B} \to \mathbb{R}^3\} \to \mathbb{R}$ with the form

$$B(\mathbf{f}) = \int_{\mathcal{B}} \hat{B}(\mathbf{x}, \mathbf{f})\,\mathrm{d}\mathbf{x}\,, \tag{3.6}$$

such that its Gâteaux derivative in a direction $\mathbf{w}$ is given by

$$B'(\mathbf{f})\,\mathbf{w} = \int_{\mathcal{B}} \hat{\mathbf{b}}(\mathbf{x}, \mathbf{f}) \cdot \mathbf{w}\,\mathrm{d}\mathbf{x}. \tag{3.7}$$

The function $\hat{B} : \mathcal{B} \times \mathbb{R}^3 \to \mathbb{R}$ is called the potential of the applied body force. For the conservative surface force $\mathbf{t}$, there is a functional $T : \{\mathbf{f} : \mathcal{B} \to \mathbb{R}^3\} \to \mathbb{R}$ with the form

$$T(\mathbf{f}) = \int_{\partial\mathcal{B}} \hat{T}(\mathbf{x}, \mathbf{f}, \nabla\mathbf{f})\,\mathrm{d}A\,, \tag{3.8}$$

such that its Gâteaux derivative in a direction $\mathbf{w}$ is given by

$$T'(\mathbf{f})\,\mathbf{w} = \int_{\partial\mathcal{B}} \hat{\mathbf{t}}(\mathbf{x}, \nabla\mathbf{f}) \cdot \mathbf{w}\,\mathrm{d}A\,. \tag{3.9}$$

The function $\hat{T} : \partial\mathcal{B} \times \mathbb{R}^3 \times \mathrm{Lin}^+ \to \mathbb{R}^3$ is called the potential of the surface force.

A body (or surface) force is a dead load if its value per unit of undeformed volume (or area) does not depend on the deformation $\mathbf{f}$. Therefore, the applied forces $\mathbf{b}$ and $\mathbf{t}$ with the forms (3.4) and (3.5) are not necessarily dead loads. For dead loads, we have

$$B(\mathbf{f}) = \int_{\mathcal{B}} \mathbf{b} \cdot \mathbf{f}\,\mathrm{d}\mathbf{x}\,, \qquad T(\mathbf{f}) = \int_{\partial_2\mathcal{B}} \mathbf{t} \cdot \mathbf{f}\,\mathrm{d}A\,. \tag{3.10}$$

An applied force of interest in this work is the pressure load, which is given by

$$\mathbf{t}_{\mathbf{f}}(\mathbf{y}) = -p\,\mathbf{n}(\mathbf{y})\,, \qquad \mathbf{y} \in \mathbf{f}(\partial_2\mathcal{B})\,, \tag{3.11}$$

where $p > 0$ is a pressure and $\mathbf{n}(\mathbf{y})$ is the unit outer normal vector to the surface $\mathbf{f}(\partial_2\mathcal{B})$ at $\mathbf{y}$. From (3.11), (3.3), and the Nanson's formula,

$$\mathbf{n}\,\mathrm{d}a = (\det\mathbf{F})\,\mathbf{F}^{-T}\mathbf{N}\,\mathrm{d}A\,, \tag{3.12}$$

where $\mathrm{d}a$ and $\mathrm{d}A$ are infinitesimal areas in the deformed and undeformed configurations, respectively, we have that $\hat{\mathbf{t}}$ in (3.5) becomes

$$\hat{\mathbf{t}}(\mathbf{x},\mathbf{F}) = -p\,\mathrm{cof}\,\mathbf{F}\,\mathbf{N}(\mathbf{x}), \qquad \mathbf{x}\in\partial_2\mathcal{B}\,, \tag{3.13}$$

where $\mathrm{cof}\,\mathbf{F} \triangleq (\det\mathbf{F})\,\mathbf{F}^{-T}$. We see from (3.13) that the pressure load is not a dead load since $\hat{\mathbf{t}}$ depends on $\mathbf{f}$ through its gradient. It is possible to show that the uniform pressure is a conservative surface force whose functional T is given by, (Ciarlet, 1988),

$$T(\mathbf{f}) = -\frac{p}{3}\int_{\partial\mathcal{B}}(\mathrm{cof}\,\nabla\mathbf{f}\,\mathbf{N})\cdot\mathbf{f}\,\mathrm{d}A = -p\int_{\mathcal{B}}\det\nabla\mathbf{f}\,\mathrm{d}\mathbf{x}\,. \tag{3.14}$$

3.2 Stress

Static problems in continuum mechanics are based on the following principle.

Stress principle of Euler and Cauchy: *Consider a body occupying a deformed configuration* $\mathbf{f}(\mathcal{B})$ *and subjected to applied forces given by the densities* $\mathbf{b}_\mathbf{f} : \mathbf{f}(\mathcal{B}) \to \mathbb{R}^3$ *and* $\mathbf{t}_\mathbf{f} : \mathbf{f}(\partial_2\mathcal{B}) \to \mathbb{R}^3$*. Then, there is a vector field* $\mathbf{s}_\mathbf{f} : \mathbf{f}(\mathcal{B})\times\mathcal{N} \to \mathbb{R}^3$*, which is called the Cauchy stress vector, where* $\mathcal{N} \triangleq \{\mathbf{v}\in\mathbb{R}^3 : |\mathbf{v}| = 1\}$*, such that:*

(a) *For any subdomain* $\mathcal{S}_\mathbf{f}$ *of* $\mathbf{f}(\mathcal{B})$*, and at any point* $\mathbf{y}\in\mathbf{f}(\partial_2\mathcal{B})\cap\partial\mathcal{S}_\mathbf{f}$ *where the unit outer normal vector* $\mathbf{n}$ *to* $\mathbf{f}(\partial_2\mathcal{B})\cap\partial\mathcal{S}_\mathbf{f}$ *exists,* $\mathbf{s}_\mathbf{f}(\mathbf{y},\mathbf{n}) = \mathbf{t}_\mathbf{f}(\mathbf{y})$*.*

(b) *For any subdomain* $\mathcal{S}_\mathbf{f}$ *of* $\mathbf{f}(\mathcal{B})$*,*

$$\int_{\mathcal{S}_\mathbf{f}}\mathbf{b}_\mathbf{f}(\mathbf{y})\,\mathrm{d}\mathbf{y} + \int_{\partial\mathcal{S}_\mathbf{f}}\mathbf{s}_\mathbf{f}(\mathbf{y},\mathbf{n})\,\mathrm{d}a = \mathbf{0}\,, \tag{3.15}$$

$$\int_{\mathcal{S}_\mathbf{f}}\mathbf{r}(\mathbf{y})\times\mathbf{b}_\mathbf{f}(\mathbf{y})\,\mathrm{d}\mathbf{y} + \int_{\partial\mathcal{S}_\mathbf{f}}\mathbf{r}(\mathbf{y})\times\mathbf{s}_\mathbf{f}(\mathbf{y},\mathbf{n})\,\mathrm{d}a = \mathbf{0}\,, \tag{3.16}$$

where $\mathbf{n}$ *denotes the unit outer normal vector along* $\partial\mathcal{S}_\mathbf{f}$*,* $\mathbf{r}(\mathbf{y}) = \mathbf{y}-\mathbf{o}$ *is the position vector with respect to the origin* $\mathbf{o}$ *of a coordinate system, and* $\times$ *denotes the vector product.*

The equations (3.15) and (3.16) are referred to as the axioms of force and moment balance, respectively. The above stress principle is a particular case of the stress principle for dynamical problems.

Under some smoothness conditions of $\mathbf{b}_\mathbf{f}$ and $\mathbf{s}_\mathbf{f}$, the stress principle of Euler and Cauchy implies that there is a tensor field $\mathbf{T} : \mathbf{f}(\mathcal{B}) \to \mathrm{Lin}$, called the *Cauchy stress tensor*, such that

$$\mathbf{s}_\mathbf{f}(\mathbf{y},\mathbf{n}) = \mathbf{T}(\mathbf{y})\,\mathbf{n}\,, \qquad \forall\,\mathbf{y}\in\mathbf{f}(\mathcal{B}) \text{ and } \forall\,\mathbf{n}\in\mathcal{N}\,, \tag{3.17}$$

and

$$\operatorname{div}\mathbf{T}(\mathbf{y}) + \mathbf{b}_{\mathbf{f}}(\mathbf{y}) = \mathbf{0}\,, \qquad \forall\,\mathbf{y} \in \mathbf{f}(\mathcal{B})\,, \tag{3.18}$$

$$\mathbf{T}(\mathbf{y}) = \mathbf{T}(\mathbf{y})^T\,, \qquad \forall\,\mathbf{y} \in \mathbf{f}(\mathcal{B})\,, \tag{3.19}$$

$$\mathbf{T}(\mathbf{y})\,\mathbf{n}(\mathbf{y}) = \mathbf{t}_{\mathbf{f}}(\mathbf{y})\,, \qquad \forall\,\mathbf{y} \in \mathbf{f}(\partial_2\mathcal{B})\,. \tag{3.20}$$

where div is the divergence operator with respect to $\mathbf{y}$. The expressions (3.17)-(3.20) are the main results of the Cauchy's theorem.

We can associate to the Cauchy stress tensor $\mathbf{T}$ a tensor field $\mathbf{P} : \mathcal{B} \to \mathrm{Lin}$, called the *first Piola-Kirchhoff stress tensor*, by

$$\mathbf{P}(\mathbf{x}) \triangleq (\det\mathbf{F}(\mathbf{x}))\,\mathbf{T}(\mathbf{y})\,\mathbf{F}(\mathbf{x})^{-T}\,, \qquad \mathbf{y} = \mathbf{f}(\mathbf{x})\,. \tag{3.21}$$

Equations (3.18)-(3.20) can be rewritten in terms of $\mathbf{P}$ as

$$\operatorname{Div}\mathbf{P}(\mathbf{x}) + \mathbf{b}(\mathbf{x}) = \mathbf{0}\,, \qquad \forall\,\mathbf{x} \in \mathcal{B}\,, \tag{3.22}$$

$$\mathbf{P}(\mathbf{x})\,\mathbf{F}(\mathbf{x})^T = \mathbf{F}(\mathbf{x})\,\mathbf{P}(\mathbf{x})^T\,, \qquad \forall\,\mathbf{x} \in \mathcal{B}\,, \tag{3.23}$$

$$\mathbf{P}(\mathbf{x})\,\mathbf{N}(\mathbf{x}) = \mathbf{t}(\mathbf{x})\,, \qquad \forall\,\mathbf{x} \in \partial_2\mathcal{B}\,, \tag{3.24}$$

where Div is the divergence operator with respect to $\mathbf{x}$. This is more convenient than (3.18)-(3.20) for solving problems in solid mechanics since we usually know $\mathcal{B}$ instead of $\mathbf{f}(\mathcal{B})$.

In the study of constitutive relations, it is often convenient to work with the *second Piola-Kirchhoff tensor* $\mathbf{S} : \mathcal{B} \to \mathrm{Sym}$, where $\mathrm{Sym} \triangleq \{\mathbf{A} \in \mathrm{Lin} \,|\, \mathbf{A} = \mathbf{A}^T\}$, which is symmetric and defined by

$$\mathbf{S}(\mathbf{x}) \triangleq \mathbf{F}(\mathbf{x})^{-1}\,\mathbf{P}(\mathbf{x})\,. \tag{3.25}$$

3.3 Constitutive relations

Constitutive relations are functions that relate a measure of stress, for instance, $\mathbf{T}$, $\mathbf{P}$, and $\mathbf{S}$, with the deformation $\mathbf{f}$. A material is said to be *elastic* if $\mathbf{T}$ depends on $\mathbf{f}$ only through its gradient $\mathbf{F} = \nabla\mathbf{f}$. That is, there is a function $\hat{\mathbf{T}} : \mathcal{B} \times \mathrm{Lin}^+ \to \mathrm{Sym}$, called the *response function for the Cauchy stress*, such that $\mathbf{T}(\mathbf{y}) = \hat{\mathbf{T}}(\mathbf{x}, \mathbf{F})$. We see from (3.21) and (3.25) that there are also functions $\hat{\mathbf{P}} : \mathcal{B} \times \mathrm{Lin}^+ \to \mathrm{Lin}$ and $\hat{\mathbf{S}} : \mathcal{B} \times \mathrm{Lin}^+ \to \mathrm{Sym}$ such that, for all $\mathbf{x} \in \mathcal{B}$,

$$\mathbf{P}(\mathbf{x}) = \hat{\mathbf{P}}(\mathbf{x}, \mathbf{F}(\mathbf{x}))\,, \tag{3.26}$$

$$\mathbf{S}(\mathbf{x}) = \hat{\mathbf{S}}(\mathbf{x}, \mathbf{F}(\mathbf{x}))\,. \tag{3.27}$$

The functions $\hat{\mathbf{P}}$ and $\hat{\mathbf{S}}$ are called *response functions for the first and second Piola-Kirchhoff stress*, respectively. In addition, an elastic material is *homogeneous* if its response $\hat{\mathbf{T}}$ has no explicit dependence on $\mathbf{x}$. In this case, it follows from (3.21) and (3.25)-(3.27) that both $\hat{\mathbf{P}}$ and $\hat{\mathbf{S}}$ also do not depend explicitly on $\mathbf{x}$.

An elastic material is said to be *hyperelastic* if there is a function $W : \mathcal{B} \times \mathrm{Lin}^+ \to \mathbb{R}$, called the *strain energy density* or the *store energy function*, such that

$$\hat{\mathbf{P}}(\mathbf{x}, \mathbf{F}) = \frac{\partial W}{\partial \mathbf{F}}(\mathbf{x}, \mathbf{F}) \,, \tag{3.28}$$

where $\partial(\cdot)/\partial\mathbf{F}$ denotes the gradient with respect to $\mathbf{F}$.

The axiom of material frame-indifference, also known as the axiom of invariance under change of observer or axiom of objectivity, represents the idea that observable quantities, such as mass, temperature, and surface forces, should not depend on the observer. In the study of elastic materials, this axiom can be stated as

Axiom of material frame-indifference: *Let the deformed configuration* $\mathbf{f}(\mathcal{B})$ *be related to another deformed configuration* $\mathbf{g}(\mathcal{B})$ *through* $\mathbf{g} = \mathbf{Q}\,\mathbf{f}$ *for some* $\mathbf{Q} \in \mathrm{Rot}$*, where* $\mathrm{Rot} \triangleq \{\mathbf{A} \in \mathrm{Lin} \mid \det \mathbf{A} = 1 \,,\ \mathbf{A}^{-1} = \mathbf{A}^T\}$ *is the set of rotations in* $\mathbb{R}^3$*. Then*

$$\mathbf{s}_{\mathbf{g}}(\mathbf{g}(\mathbf{x}), \mathbf{Q}\,\mathbf{n}) = \mathbf{Q}\,\mathbf{s}_{\mathbf{f}}(\mathbf{f}(\mathbf{x}), \mathbf{n}) \,, \qquad \forall\, \mathbf{x} \in \mathcal{B} \,,\ \mathbf{n} \in \mathcal{N} \,, \tag{3.29}$$

where $\mathbf{s}_{\mathbf{g}} : \mathbf{g}(\mathcal{B}) \times \mathcal{N} \to \mathbb{R}^3$ *and* $\mathbf{s}_{\mathbf{f}} : \mathbf{f}(\mathcal{B}) \times \mathcal{N} \to \mathbb{R}^3$ *are the Cauchy stress vector fields in the deformed configurations* $\mathbf{g}(\mathcal{B})$ *and* $\mathbf{f}(\mathcal{B})$*, respectively.*

It is possible to show that this axiom is satisfied if and only if, for all $\mathbf{x} \in \mathcal{B}$ and $\mathbf{F} \in \mathrm{Lin}^+$, (Ciarlet, 1988),

$$\hat{\mathbf{T}}(\mathbf{x}, \mathbf{Q}\,\mathbf{F}) = \mathbf{Q}\,\hat{\mathbf{T}}(\mathbf{x}, \mathbf{F})\,\mathbf{Q}^T \,, \qquad \mathbf{Q} \in \mathrm{Rot} \,, \tag{3.30}$$

or, equivalently, if and only if, there exists a function $\tilde{\mathbf{S}} : \mathcal{B} \times \mathrm{Sym}_> \to \mathrm{Sym}$ such that, for all $\mathbf{x} \in \mathcal{B}$ and $\mathbf{F} \in \mathrm{Lin}^+$,

$$\hat{\mathbf{S}}(\mathbf{x}, \mathbf{F}) = \tilde{\mathbf{S}}(\mathbf{x}, \mathbf{C}) \,, \qquad \mathbf{C} \triangleq \mathbf{F}^T\,\mathbf{F} \,, \tag{3.31}$$

where $\mathbf{C} \in \mathrm{Sym}_>$ is the right Cauchy-Green strain tensor and $\mathrm{Sym}_> \triangleq \{\mathbf{A} \in \mathrm{Sym} \mid \mathbf{v}\cdot\mathbf{A}\,\mathbf{v} > 0 \,,\ \forall\, \mathbf{v} \in \mathbb{R}^3 \backslash \{\mathbf{0}\}\}$ is the set of positive definite linear transformations in $\mathbb{R}^3$. For later use, an alternative form of (3.31) can be written as

$$\hat{\mathbf{S}}(\mathbf{x}, \mathbf{F}) = \check{\mathbf{S}}(\mathbf{x}, \mathbf{E}) \,, \qquad \mathbf{E} \triangleq \frac{1}{2}(\mathbf{C} - \mathbf{I}) \,, \tag{3.32}$$

where $\mathbf{E}$ is the Green-St Venant strain tensor.

For hyperelastic materials, the axiom of frame-indifference is satisfied if and only if the strain energy function W satisfies, (Ciarlet, 1988),

$$W(\mathbf{x}, \mathbf{Q}\,\mathbf{F}) = W(\mathbf{x}, \mathbf{F}) \,, \qquad \mathbf{Q} \in \mathrm{Rot} \,, \tag{3.33}$$

for all $\mathbf{F} \in \mathrm{Lin}^+$, or, equivalently, if and only if there is a function $\tilde{W} : \mathcal{B} \times \mathrm{Sym}_> \to \mathbb{R}$ such that

$$W(\mathbf{x}, \mathbf{F}) = \tilde{W}(\mathbf{x}, \mathbf{C}) \,, \qquad \forall\, \mathbf{F} \in \mathrm{Lin}^+ \,. \tag{3.34}$$

We can also use material symmetry to impose further restrictions on the form of the response function. These restrictions take the form

$$\hat{\mathbf{T}}(\mathbf{x}, \mathbf{F}\,\mathbf{Q}) = \hat{\mathbf{T}}(\mathbf{x}, \mathbf{F})\,, \qquad \forall\,\mathbf{F} \in \mathrm{Lin}^+\,, \quad \forall\,\mathbf{Q} \in \mathcal{G}_{\mathbf{x}}\,. \tag{3.35}$$

where $\mathcal{G}_{\mathbf{x}} \subset \mathrm{Rot}$ is called the *symmetry group at* $\mathbf{x}$. For instance, if $\mathcal{G}_{\mathbf{x}} = \mathrm{Rot}$ we say that the material is isotropic at $\mathbf{x}$; otherwise, it is anisotropic. In the case of transverse isotropy with the material symmetry $\mathbf{m}_1 \in \mathbb{R}^3$, $\mathcal{G}_{\mathbf{x}}$ consists of rotations about $\mathbf{m}_1$. In this work, we consider orthotropic materials with respect to three orthogonal planes that are normal to the vectors $\mathbf{m}_1$, $\mathbf{m}_2$, $\mathbf{m}_3 \in \mathbb{R}^3$, for which $\mathcal{G}_{\mathbf{x}}$ consists of the identity transformation and rotations about $\mathbf{m}_1$, $\mathbf{m}_2$, $\mathbf{m}_3$ by π radians. In this case, since $\mathbf{m}_3 = \mathbf{m}_1 \times \mathbf{m}_2$, we say that a material is *orthotropic* with the material symmetries $\mathbf{m}_1$ and $\mathbf{m}_2$.

Equivalently, we can express the material symmetry condition (3.35) in terms of $\hat{\mathbf{P}}$ and $\hat{\mathbf{S}}$ as

$$\begin{aligned} &\hat{\mathbf{P}}(\mathbf{x}, \mathbf{F}\,\mathbf{Q}) = \hat{\mathbf{P}}(\mathbf{x}, \mathbf{F})\,\mathbf{Q}\,, \\ &\hat{\mathbf{S}}(\mathbf{x}, \mathbf{F}\,\mathbf{Q}) = \mathbf{Q}^T\,\hat{\mathbf{S}}(\mathbf{x}, \mathbf{F})\,\mathbf{Q}\,, \end{aligned} \qquad \forall\,\mathbf{F} \in \mathrm{Lin}^+\,, \quad \forall\,\mathbf{Q} \in \mathcal{G}_{\mathbf{x}}\,. \tag{3.36}$$

In the case of hyperelastic materials, it follows from (3.28) and (3.35) that the strain energy function W satisfies

$$W(\mathbf{F}\,\mathbf{Q}) = W(\mathbf{F})\,, \qquad \forall\,\mathbf{F} \in \mathrm{Lin}^+\,, \quad \forall\,\mathbf{Q} \in \mathcal{G}_{\mathbf{x}}\,. \tag{3.37}$$

The fourth-order elasticity tensor $\hat{\mathbb{C}}(\mathbf{x}, \mathbf{F})$, defined by

$$\hat{\mathbb{C}}(\mathbf{x}, \mathbf{F}) \triangleq \frac{\partial \hat{\mathbf{P}}}{\partial \mathbf{F}}(\mathbf{x}, \mathbf{F})\,, \tag{3.38}$$

is an important tensor in the study of elastic bodies. Assuming that the reference configuration is stress-free, that is, $\hat{\mathbf{P}}(\mathbf{x}, \mathbf{I}) = \hat{\mathbf{T}}(\mathbf{x}, \mathbf{I}) = \check{\mathbf{S}}(\mathbf{x}, \mathbf{0}) = \mathbf{0}$, it is possible to show that, (Gurtin, 1982),

$$\mathbb{C}(\mathbf{x}) \triangleq \hat{\mathbb{C}}(\mathbf{x}, \mathbf{I}) = \frac{\partial \hat{\mathbf{P}}}{\partial \mathbf{F}}(\mathbf{x}, \mathbf{I}) = \frac{\partial \hat{\mathbf{T}}}{\partial \mathbf{F}}(\mathbf{x}, \mathbf{I}) = \frac{\partial \check{\mathbf{S}}}{\partial \mathbf{E}}(\mathbf{x}, \mathbf{0})\,, \tag{3.39}$$

where $\hat{\mathbf{T}}(\mathbf{x}, \mathbf{F})$, $\hat{\mathbf{P}}(\mathbf{x}, \mathbf{F})$, and $\check{\mathbf{S}}(\mathbf{x}, \mathbf{E})$ are the response functions for the Cauchy stress and for the first and second Piola-Kirchhoff stress, respectively, introduced in the beginning of Section 3.3. In addition, $\mathbb{C}(\mathbf{x})$ is invariant under rotations $\mathbf{Q} \in \mathcal{G}_{\mathbf{x}}$ in the sense that, for any $\mathbf{A} \in \mathrm{Lin}$ and $\mathbf{Q} \in \mathcal{G}_{\mathbf{x}}$,

$$\mathbf{Q}\,\mathbb{C}(\mathbf{x})[\mathbf{A}]\,\mathbf{Q}^T = \mathbb{C}(\mathbf{x})[\mathbf{Q}\,\mathbf{A}\,\mathbf{Q}^T]\,. \tag{3.40}$$

If the material is homogeneous and the reference configuration is stress-free, we expand $\check{\mathbf{S}}(\mathbf{E})$ in a Taylor series about $\mathbf{E} = \mathbf{0}$ and use (3.39) to obtain

$$\check{\mathbf{S}}(\mathbf{E}) = \mathbb{C}[\mathbf{E}] + o(\mathbf{E})\,. \tag{3.41}$$

In addition, if the material is also isotropic, then it is possible to show that, (Ciarlet, 1988),

$$\check{\mathbf{S}}(\mathbf{E}) = \Lambda\,(\operatorname{tr}\mathbf{E})\,\mathbf{I} + 2\,\mu\,\mathbf{E} + o(\mathbf{E})\,, \tag{3.42}$$

where Λ and μ are the first and second Lamé constants, respectively, and $\operatorname{tr}(\cdot)$ is the trace operator, which linearly maps any $\mathbf{A} \in \mathrm{Lin}$ to a scalar and satisfies $\operatorname{tr}(\mathbf{v}_1 \otimes \mathbf{v}_2) = \mathbf{v}_1 \cdot \mathbf{v}_2$ for all $\mathbf{v}_1, \mathbf{v}_2 \in \mathbb{R}^3$, with $\otimes$ denoting the tensor product.

The classical St Venant-Kirchhoff material, which is isotropic, is defined as the material whose response function $\check{\mathbf{S}}$ is given by (3.42) neglecting the higher-order terms, that is,

$$\check{\mathbf{S}}(\mathbf{E}) = \Lambda\,(\operatorname{tr}\mathbf{E})\,\mathbf{I} + 2\,\mu\,\mathbf{E}\,. \tag{3.43}$$

This material is hyperelastic with a strain energy function $\check{W}(\mathbf{E}) = \hat{W}(\mathbf{F}) = \tilde{W}(\mathbf{C})$ given by

$$\check{W}(\mathbf{E}) = \frac{\Lambda}{2}(\operatorname{tr}\mathbf{E})^2 + \mu\operatorname{tr}(\mathbf{E}^2)\,. \tag{3.44}$$

Similarly, we can neglect the higher-order terms in (3.41) to define the *anisotropic St Venant-Kirchhoff material* as the material whose response $\check{\mathbf{S}}$ is given by the relation

$$\check{\mathbf{S}}(\mathbf{E}) = \mathbb{C}[\mathbf{E}]\,, \tag{3.45}$$

which corresponds to the strain energy function

$$\check{W}(\mathbf{E}) = \frac{1}{2}\,\mathbf{E}\cdot\mathbb{C}[\mathbf{E}]\,. \tag{3.46}$$

It follows from (3.41) and (3.45) that, if the reference configuration is stress-free, then the response of any homogeneous elastic material near the reference configuration reduces to that of the anisotropic St Venant-Kirchhoff material.

Using an orthonormal basis $\{\mathbf{e}_1, \mathbf{e}_2, \mathbf{e}_3\}$ of $\mathbb{R}^3$, the anisotropic case, given by (3.46), reduces to the isotropic one, given by (3.44), when the nonzero components of the fourth-order tensor $\mathbb{C} = \sum_{i,j,k,l=1}^{3} c_{ijkl}\,\mathbf{e}_i \otimes \mathbf{e}_j \otimes \mathbf{e}_k \otimes \mathbf{e}_l$, which has the symmetries $c_{ijkl} = c_{klij} = c_{jikl} = c_{ijlk}$, assume the values

$$\begin{aligned} &c_{11} = \Lambda + 2\,\mu\,, \qquad c_{12} = \Lambda\,, \\ &c_{22} = c_{33} = c_{11}\,, \qquad c_{13} = c_{23} = c_{12}\,, \qquad c_{44} = c_{55} = c_{66} = \frac{c_{11} - c_{12}}{2}\,, \end{aligned} \tag{3.47}$$

where we have used the symmetries of $\mathbb{C}$ and the rule $11 \to 1$, $22 \to 2$, $33 \to 3$, $23 \to 4$, $13 \to 5$, $12 \to 6$ to rewrite the four-index notation c_{ijkl}, where $i, j, k, l = 1, 2, 3$, into a two-index notation c_{ab}, where $a, b = 1, 2, 3, 4, 5, 6$.

If the material is orthotropic with $\mathbf{m}_i = \mathbf{e}_i$, $i = 1, 2, 3$, then the nonzero components of $\mathbb{C}$ are given by, (Sokolnikoff, 1956),

$$c_{11}\,, \quad c_{22}\,, \quad c_{33}\,, \quad c_{12}\,, \quad c_{13}\,, \quad c_{23}\,, \quad c_{44}\,, \quad c_{55}\,, \quad c_{66}\,. \tag{3.48}$$

These nine independent constants can be written in terms of the engineering constants E_1, E_2, E_3, v_{12}, v_{23}, v_{13}, G_{12}, G_{13}, G_{23} as

$$\begin{aligned}
&c_{11} = \frac{1-\mathrm{v}_{23}\,\mathrm{v}_{32}}{E_2\,E_3\,\bar{\mathrm{v}}}\,, \qquad c_{22} = \frac{1-\mathrm{v}_{13}\,\mathrm{v}_{31}}{E_1\,E_3\,\bar{\mathrm{v}}}\,, \qquad c_{33} = \frac{1-\mathrm{v}_{12}\,\mathrm{v}_{21}}{E_1\,E_2\,\bar{\mathrm{v}}}\,,\\
&c_{12} = \frac{\mathrm{v}_{21}+\mathrm{v}_{31}\,\mathrm{v}_{23}}{E_2\,E_3\,\bar{\mathrm{v}}}\,, \qquad c_{13} = \frac{\mathrm{v}_{13}+\mathrm{v}_{12}\,\mathrm{v}_{23}}{E_1\,E_2\,\bar{\mathrm{v}}}\,, \qquad c_{23} = \frac{\mathrm{v}_{32}+\mathrm{v}_{12}\,\mathrm{v}_{31}}{E_1\,E_3\,\bar{\mathrm{v}}}\,,\\
&c_{44} = G_{23}\,, \qquad c_{55} = G_{13}\,, \qquad c_{66} = G_{12}\,,
\end{aligned} \tag{3.49}$$

where

$$\begin{aligned}
&\bar{\mathrm{v}} = \frac{1}{E_1\,E_2\,E_3}\,\det\begin{bmatrix} 1 & -\mathrm{v}_{21} & -\mathrm{v}_{31}\\ -\mathrm{v}_{12} & 1 & -\mathrm{v}_{32}\\ -\mathrm{v}_{13} & -\mathrm{v}_{23} & 1\end{bmatrix}\,,\\
&\mathrm{v}_{21} = \mathrm{v}_{12}\,\frac{E_2}{E_1}\,, \qquad \mathrm{v}_{31} = \mathrm{v}_{13}\,\frac{E_3}{E_1}\,, \qquad \mathrm{v}_{32} = \mathrm{v}_{23}\,\frac{E_3}{E_2}\,,
\end{aligned} \tag{3.50}$$

with E, v, G denoting the Young's modulus, the Poisson's ratio, and the shear modulus, respectively, and the subscripts 1, 2, 3 denoting the directions $\mathbf{e}_1$, $\mathbf{e}_2$, $\mathbf{e}_3$, respectively.

For isotropic materials, it is usual to write the strain energy function as a function of the invariants of $\mathbf{C}$ given by

$$I_1 \triangleq \mathrm{tr}\,\mathbf{C}\,, \qquad I_2 \triangleq \frac{1}{2}[I_1^2 - \mathrm{tr}\,(\mathbf{C}^2)]\,, \qquad I_3 \triangleq \det\mathbf{C}\,, \tag{3.51}$$

and, for orthotropic materials with the material symmetries $\mathbf{m}_1$ and $\mathbf{m}_2$, the invariants

$$I_4 \triangleq \mathbf{m}_1\cdot\mathbf{C}\,\mathbf{m}_1\,, \quad I_5 \triangleq \mathbf{m}_1\cdot\mathbf{C}^2\,\mathbf{m}_1\,, \quad I_6 \triangleq \mathbf{m}_2\cdot\mathbf{C}\,\mathbf{m}_2\,, \quad I_7 \triangleq \mathbf{m}_2\cdot\mathbf{C}^2\,\mathbf{m}_2\,, \tag{3.52}$$

in addition to I_1, I_2, and I_3.

Let us rewrite the strain energy function $\check{W}(\mathbf{E})$ of the orthotropic St Venant-Kirchhoff material with the orthogonal material symmetries $\mathbf{m}_1$ and $\mathbf{m}_2$. Recall from above that, in this case, $\check{W}(\mathbf{E})$ is given by (3.46), where $\mathbb{C}$ has the nonzero components in (3.48). It follows from its symmetry group, introduced below (3.35), that $\check{W}(\mathbf{E})$ can be written as a function of the invariants, (Spencer, 1984),

$$\begin{aligned}
&\mathrm{tr}\,\mathbf{E}\,, \qquad \mathrm{tr}\,(\mathbf{E}^2)\,, \qquad \mathrm{tr}\,(\mathbf{E}^3)\,,\\
&\mathbf{m}_1\cdot\mathbf{E}\,\mathbf{m}_1\,, \qquad \mathbf{m}_1\cdot\mathbf{E}^2\,\mathbf{m}_1\,, \qquad \mathbf{m}_2\cdot\mathbf{E}\,\mathbf{m}_2\,, \qquad \mathbf{m}_2\cdot\mathbf{E}^2\,\mathbf{m}_2\,.
\end{aligned} \tag{3.53}$$

Since $\mathbf{E}$ is given by (3.32.b), the above invariants can be written in terms of the invariants $I_1, I_2, \ldots, I_7$ as

$$\begin{aligned}
&\mathrm{tr}\,\mathbf{E} = \frac{1}{2}\,(I_1-3)\,, \qquad \mathrm{tr}\,(\mathbf{E}^2) = \frac{1}{4}\left(I_1^2 - 2\,I_1 - 2\,I_2 + 3\right),\\
&\mathrm{tr}\,(\mathbf{E}^3) = \frac{1}{8}\left(I_1^3 - 3\,I_1^2 - 3\,I_1\,I_2 + 3\,I_1 + 6\,I_2 + 3\,I_3 - 3\right),\\
&\mathbf{m}_1\cdot\mathbf{E}\,\mathbf{m}_1 = \frac{1}{2}\,(I_4-1)\,, \qquad \mathbf{m}_1\cdot\mathbf{E}^2\,\mathbf{m}_1 = \frac{1}{4}\,(-2\,I_4 + I_5 + 1)\,,\\
&\mathbf{m}_2\cdot\mathbf{E}\,\mathbf{m}_2 = \frac{1}{2}\,(I_6-1)\,, \qquad \mathbf{m}_2\cdot\mathbf{E}^2\,\mathbf{m}_2 = \frac{1}{4}\,(-2\,I_6 + I_7 + 1)\,.
\end{aligned} \tag{3.54}$$

In addition, note from (3.46) that $\check{W}(\mathbf{E})$ is a quadratic form on $\mathbf{E}$, that is, it has the form $\check{W}(\mathbf{E}) = \beta(\mathbf{E}, \mathbf{E})$, where β is a linear function on both of its arguments. The most general quadratic form on $\mathbf{E}$ that can be written with the invariants in (3.53) is

$$\begin{aligned}\check{W}(\mathbf{E}) = \frac{\Lambda}{2}\,(\operatorname{tr}\mathbf{E})^2 + \mu\operatorname{tr}(\mathbf{E}^2) \\ + \alpha_1\,(\mathbf{m}_1\cdot\mathbf{E}\,\mathbf{m}_1)^2 + \alpha_2\,(\mathbf{m}_1\cdot\mathbf{E}^2\,\mathbf{m}_1) + \alpha_3\operatorname{tr}\mathbf{E}\,(\mathbf{m}_1\cdot\mathbf{E}\,\mathbf{m}_1) \\ + \alpha_4\,(\mathbf{m}_2\cdot\mathbf{E}\,\mathbf{m}_2)^2 + \alpha_5\,(\mathbf{m}_2\cdot\mathbf{E}^2\,\mathbf{m}_2) + \alpha_6\operatorname{tr}\mathbf{E}\,(\mathbf{m}_2\cdot\mathbf{E}\,\mathbf{m}_2) \\ + \alpha_7\,(\mathbf{m}_1\cdot\mathbf{E}\,\mathbf{m}_1)\,(\mathbf{m}_2\cdot\mathbf{E}\,\mathbf{m}_2)\,,\end{aligned} \tag{3.55}$$

where Λ, μ, α_i, $i = 1, 2, \ldots, 7$, are material parameters. Comparing (3.55) with (3.44), we see that the strain energy function of the orthotropic St Venant-Kirchhoff material can be written as the sum of the strain energy function of its classical isotropic version plus terms that depend on $\mathbf{m}_1$ and $\mathbf{m}_2$. This kind of representation is associated with the idea of representing an orthotropic material as a composite made of an isotropic matrix reinforced with fibers in the directions $\mathbf{m}_1$ and $\mathbf{m}_2$.

Substituting (3.54) into (3.55), we obtain the strain energy function of the orthotropic St Venant-Kirchhoff material in the form $\check{W}(\mathbf{E}) = \bar{W}(I_1, I_2, I_4, I_5, I_6, I_7)$, where

$$\begin{aligned}\bar{W}(I_1, I_2, I_4, I_5, I_6, I_7) &= \bar{W}_{\text{iso}}(I_1, I_2) + \bar{W}_{\text{aniso}}(I_1, I_4, I_5, I_6, I_7) \\ \bar{W}_{\text{iso}}(I_1, I_2) &= \mu\,(I_1 - 3) + \frac{\Lambda + 2\,\mu}{8}(I_1 - 3)^2 - \frac{\mu}{2}\,(I_2 - 3)\,, \\ \bar{W}_{\text{aniso}}(I_1, I_4, I_5, I_6, I_7) &= \frac{1}{4}\Big[\alpha_1\,(I_4 - 1)^2 + \alpha_2\,(-2\,I_4 + I_5 + 1) \\ &\quad + \alpha_3\,(I_1 - 3)\,(I_4 - 1) + \alpha_4\,(I_6 - 1)^2 \\ &\quad + \alpha_5\,(-2\,I_6 + I_7 + 1) + \alpha_6\,(I_1 - 3)\,(I_6 - 1) \\ &\quad + \alpha_7\,(I_4 - 1)\,(I_6 - 1)\Big]\,.\end{aligned} \tag{3.56}$$

It is not difficult to verify that $\bar{W}$ given by (3.56) is the same strain energy function used by Raible *et al.* (2005) to study wrinkling in membranes. In addition, by taking $\alpha_4 = \alpha_5 = \alpha_6 = \alpha_7 = 0$, $\bar{W}$ reduces to the stain energy function used by Bonet and Burton (1998) to represent a transversely isotropic St Venant-Kirchhoff material.

Next, we introduce some restrictions on the strain energy function $\bar{W}$ of an orthotropic hyperelastic model, so that it corresponds to a stress-free undeformed reference configuration and is consistent with the classical linear elasticity of orthotropic materials, whose elastic constants are given by (3.48).

It follows from (3.25), (3.28), and (3.31.b) that

$$\begin{aligned}\mathbf{S} &= 2\,\frac{\partial \tilde{W}(\mathbf{x},\mathbf{C})}{\partial \mathbf{C}} = 2\sum_{i=1}^{7}\frac{\partial \bar{W}}{\partial I_i}\,\frac{\partial I_i}{\partial \mathbf{C}} \\ &= 2\Big[\bar{W}_1\,\mathbf{I} + \bar{W}_2\,(I_1\,\mathbf{I}-\mathbf{C}) + \bar{W}_3\,I_3\,\mathbf{C}^{-1} \\ &\qquad + \bar{W}_4\,\mathbf{m}_1\otimes\mathbf{m}_1 + \bar{W}_5\,(\mathbf{C}\mathbf{m}_1\otimes\mathbf{m}_1 + \mathbf{m}_1\otimes\mathbf{C}\mathbf{m}_1) \\ &\qquad + \bar{W}_6\,\mathbf{m}_2\otimes\mathbf{m}_2 + \bar{W}_7\,(\mathbf{C}\mathbf{m}_2\otimes\mathbf{m}_2 + \mathbf{m}_2\otimes\mathbf{C}\mathbf{m}_2)\Big]\,,\end{aligned} \tag{3.57}$$

where $\bar{W}_i \triangleq \partial\bar{W}/\partial I_i$, $i = 1, 2, \ldots, 7$. Then, to ensure that the stress is null at the reference configuration, where $\mathbf{C} = \mathbf{I}$, $I_1 = I_2 = 3$, and $I_3 = I_4 = I_5 = I_6 = I_7 = 1$, we must have

$$\mathring{W}_1 + 2\,\mathring{W}_2 + \mathring{W}_3 = 0\,, \qquad \mathring{W}_4 + 2\,\mathring{W}_5 = 0\,, \qquad \mathring{W}_6 + 2\,\mathring{W}_7 = 0\,, \tag{3.58}$$

with $\mathring{W}_i$, $i = 1, 2, ..., 7$, denoting $\bar{W}_i$ evaluated at the undeformed reference configuration.

Linearizing $\mathbf{S}$ with respect to $\mathbf{E}$ around the reference configuration yields[1]

$$\begin{aligned}\mathbf{S} = 2\Big[&2\,\mathbf{I}\,(k_1\,\mathrm{tr}\,\mathbf{E} + k_3\,\mathbf{m}_1\cdot\mathbf{E}\,\mathbf{m}_1 + k_7\,\mathbf{m}_2\cdot\mathbf{E}\,\mathbf{m}_2) + k_2\,\mathbf{E} \\ &+ 2\,\mathbf{m}_1\otimes\mathbf{m}_1\,(k_3\,\mathrm{tr}\,\mathbf{E} + k_4\,\mathbf{m}_1\cdot\mathbf{E}\,\mathbf{m}_1 + k_5\,\mathbf{m}_2\cdot\mathbf{E}\,\mathbf{m}_2) \\ &+ 2\,\mathbf{m}_2\otimes\mathbf{m}_2\,(k_7\,\mathrm{tr}\,\mathbf{E} + k_5\,\mathbf{m}_1\cdot\mathbf{E}\,\mathbf{m}_1 + k_8\,\mathbf{m}_2\cdot\mathbf{E}\,\mathbf{m}_2) \\ &+ k_6\,(\mathbf{E}\,\mathbf{m}_1\otimes\mathbf{m}_1 + \mathbf{m}_1\otimes\mathbf{E}\,\mathbf{m}_1) \\ &+ k_9\,(\mathbf{E}\,\mathbf{m}_2\otimes\mathbf{m}_2 + \mathbf{m}_2\otimes\mathbf{E}\,\mathbf{m}_2)\Big]\,,\end{aligned} \tag{3.59}$$

where

$$\begin{aligned}k_1 &\triangleq \mathring{W}_2 + \mathring{W}_3 + \mathring{W}_{11} + 4\,\mathring{W}_{22} + \mathring{W}_{33} + 4\,\mathring{W}_{12} + 2\,\mathring{W}_{13} + 4\,\mathring{W}_{23} \\ k_2 &\triangleq -2\,\mathring{W}_2 - 2\,\mathring{W}_3 \\ k_3 &\triangleq \mathring{W}_{14} + 2\,\mathring{W}_{24} + \mathring{W}_{34} + 2\,\mathring{W}_{15} + 4\,\mathring{W}_{25} + 2\,\mathring{W}_{35} \\ k_4 &\triangleq \mathring{W}_{44} + 4\,\mathring{W}_{55} + 4\,\mathring{W}_{45} \\ k_5 &\triangleq \mathring{W}_{46} + 2\,\mathring{W}_{47} + 2\,\mathring{W}_{56} + 4\,\mathring{W}_{57} \\ k_6 &\triangleq 2\,\mathring{W}_5 \\ k_7 &\triangleq \mathring{W}_{16} + 2\,\mathring{W}_{26} + \mathring{W}_{36} + 2\,\mathring{W}_{17} + 4\,\mathring{W}_{27} + 2\,\mathring{W}_{37} \\ k_8 &\triangleq \mathring{W}_{66} + 4\,\mathring{W}_{77} + 4\,\mathring{W}_{67} \\ k_9 &\triangleq 2\,\mathring{W}_7\,.\end{aligned} \tag{3.60}$$

with $\mathring{W}_{ij}$, $i, j = 1, 2, ..., 7$, denoting $\bar{W}_{ij}$ evaluated at the undeformed reference configuration.

[1] In Appendix A, we show how to obtain (3.59) in detail.

Then, for $\mathbf{m}_1 = \mathbf{e}_1$ and $\mathbf{m}_2 = \mathbf{e}_2$, we can write the components of $\mathbf{S}$, given by (3.59), in terms of the components of $\mathbf{E}$, both with respect to the basis $\{\mathbf{e}_1, \mathbf{e}_2, \mathbf{e}_3\}$, as

$$\begin{aligned}
S_{11} &= (4\,k_1 + 2\,k_2 + 8\,k_3 + 4\,k_4 + 4\,k_6)\,E_{11} + 4\,(k_1 + k_3 + k_5 + k_7)\,E_{22} \\
&\quad + 4\,(k_1 + k_3)\,E_{33}\,, \\
S_{22} &= 4\,(k_1 + k_3 + k_5 + k_7)\,E_{11} + (4\,k_1 + 2\,k_2 + 8\,k_7 + 4\,k_8 + 4\,k_9)\,E_{22} \\
&\quad + 4\,(k_1 + k_7)\,E_{33}\,, \\
S_{33} &= 4\,(k_1 + k_3)\,E_{11} + 4\,(k_1 + k_7)\,E_{22} + (4\,k_1 + 2\,k_2)\,E_{33}\,, \\
S_{23} &= 2\,(k_2 + k_9)\,E_{23}\,, \qquad S_{13} = 2\,(k_2 + k_6)\,E_{13}\,, \qquad S_{12} = 2\,(k_2 + k_6 + k_9)\,E_{12}\,.
\end{aligned} \tag{3.61}$$

On the other hand, in the classic linear elasticity, where $\mathbf{E}$ is assumed to be infinitesimal, the stress components are given by

$$\begin{aligned}
\sigma_{11} &= c_{11}\,E_{11} + c_{12}\,E_{22} + c_{13}\,E_{33}\,, \\
\sigma_{22} &= c_{12}\,E_{11} + c_{22}\,E_{22} + c_{23}\,E_{33}\,, \\
\sigma_{33} &= c_{13}\,E_{11} + c_{23}\,E_{22} + c_{33}\,E_{33}\,, \\
\sigma_{23} &= 2\,c_{44}\,E_{23}\,, \qquad \sigma_{13} = 2\,c_{55}\,E_{13}\,, \qquad \sigma_{12} = 2\,c_{66}\,E_{12}\,.
\end{aligned} \tag{3.62}$$

Therefore, it follows from (3.61), (3.62), and (3.60) that

$$\begin{aligned}
c_{11} &= 4\,\left(\mathring{W}_{11} + \mathring{W}_{33} + \mathring{W}_{44}\right) + 8\,\left(\mathring{W}_{13} + \mathring{W}_{14} + \mathring{W}_{34} + \mathring{W}_{5}\right), \\
&\quad + 16\,\left(\mathring{W}_{12} + \mathring{W}_{15} + \mathring{W}_{22} + \mathring{W}_{23} + \mathring{W}_{24} + \mathring{W}_{35} + \mathring{W}_{45} + \mathring{W}_{55}\right) + 32\,\mathring{W}_{25}\,, \\
c_{22} &= 4\,\left(\mathring{W}_{11} + \mathring{W}_{33}\right) + 8\,\mathring{W}_{13} + 16\,\left(\mathring{W}_{12} + \mathring{W}_{22} + \mathring{W}_{23}\right), \\
c_{33} &= 4\,\left(\mathring{W}_{11} + \mathring{W}_{33} + \mathring{W}_{66}\right) + 8\,\left(\mathring{W}_{13} + \mathring{W}_{16} + \mathring{W}_{36} + \mathring{W}_{7}\right), \\
&\quad + 16\,\left(\mathring{W}_{12} + \mathring{W}_{17} + \mathring{W}_{22} + \mathring{W}_{23} + \mathring{W}_{26} + \mathring{W}_{37} + \mathring{W}_{67} + \mathring{W}_{77}\right) + 32\,\mathring{W}_{27}\,, \\
c_{12} &= 4\,\left(\mathring{W}_{11} + \mathring{W}_{14} + \mathring{W}_{2} + \mathring{W}_{3} + \mathring{W}_{33} + \mathring{W}_{34}\right) + 8\,\left(\mathring{W}_{13} + \mathring{W}_{15} + \mathring{W}_{24} + \mathring{W}_{35}\right), \\
&\quad + 16\,\left(\mathring{W}_{12} + \mathring{W}_{22} + \mathring{W}_{23} + \mathring{W}_{25}\right), \\
c_{13} &= 4\,\left(\mathring{W}_{11} + \mathring{W}_{14} + \mathring{W}_{16} + \mathring{W}_{2} + \mathring{W}_{3} + \mathring{W}_{33} + \mathring{W}_{34} + \mathring{W}_{36} + \mathring{W}_{46}\right), \\
&\quad + 8\,\left(\mathring{W}_{13} + \mathring{W}_{15} + \mathring{W}_{17} + \mathring{W}_{24} + \mathring{W}_{26} + \mathring{W}_{35} + \mathring{W}_{37} + \mathring{W}_{47} + \mathring{W}_{56}\right), \\
&\quad + 16\,\left(\mathring{W}_{12} + \mathring{W}_{22} + \mathring{W}_{23} + \mathring{W}_{25} + \mathring{W}_{27} + \mathring{W}_{57}\right), \\
c_{23} &= 4\,\left(\mathring{W}_{11} + \mathring{W}_{16} + \mathring{W}_{2} + \mathring{W}_{3} + \mathring{W}_{33} + \mathring{W}_{36}\right) + 8\,\left(\mathring{W}_{13} + \mathring{W}_{17} + \mathring{W}_{26} + \mathring{W}_{37}\right), \\
&\quad + 16\,\left(\mathring{W}_{12} + \mathring{W}_{22} + \mathring{W}_{23} + \mathring{W}_{27}\right), \\
c_{44} &= 2\,\left(-\mathring{W}_{2} - \mathring{W}_{3} + \mathring{W}_{7}\right), \\
c_{55} &= 2\,\left(-\mathring{W}_{2} - \mathring{W}_{3} + \mathring{W}_{5} + \mathring{W}_{7}\right), \\
c_{66} &= 2\,\left(-\mathring{W}_{2} - \mathring{W}_{3} + \mathring{W}_{5}\right).
\end{aligned} \tag{3.63}$$

It is possible to verify that the restrictions (3.58) and (3.63) are equivalent to the restrictions (15) and (17) of Aguiar (2019).

Equations (3.56), (3.58), and (3.63) form a system of equations, which can be solved for Λ, μ, α_i, $i = 1, 2, \ldots, 7$, to find that

$$\Lambda = c_{33} - 2\,(c_{44} + c_{55} - c_{66})\,, \qquad \mu = c_{44} + c_{55} - c_{66}\,, \tag{3.64}$$

and

$$\begin{aligned}
&\alpha_1 = \frac{c_{11}}{2} - c_{13} + \frac{c_{33}}{2} - 2\,c_{55}\,, && \alpha_2 = 2\,(-c_{44} + c_{66})\,,\\
&\alpha_3 = c_{13} - c_{33} + 2\,(c_{44} + c_{55} - c_{66})\,, && \alpha_4 = \frac{c_{22}}{2} - c_{23} + \frac{c_{33}}{2} - 2\,c_{44}\,,\\
&\alpha_5 = 2\,(-c_{55} + c_{66})\,, && \alpha_6 = c_{23} - c_{33} + 2\,(c_{44} + c_{55} - c_{66})\,,\\
&\alpha_7 = c_{12} - c_{13} - c_{23} + c_{33} - 2\,(c_{44} + c_{55} - c_{66})\,.
\end{aligned} \tag{3.65}$$

In the case of the orthotropic St Venant-Kirchhoff material the relations (3.64) and (3.65) can also be obtained by comparing (3.46) and (3.56) since they are equivalent. However, for other orthotropic materials, we need to use (3.58) and (3.63).

We see from (3.56) that $\bar{W}$ does not depend on $I_3 = \det \mathbf{F}$ and, thus, it remains finite as $\det \mathbf{F} \to 0$. This is in disagreement with the intuitive idea that an infinite amount of energy should be required to make the volume of a body null. Therefore, the orthotropic St Venant-Kirchhoff is expected to yield unphysical results for large compressive deformations.

A simple way to satisfy this idea consists in adopting a strain energy function of the form $\bar{W} = \bar{W}_{\text{iso}} + \bar{W}_{\text{aniso}}$, where $\bar{W}_{\text{iso}} = \bar{W}_{\text{iso}}(I_1, I_2, I_3)$ goes to infinity as $I_3 \to 0$ and $\bar{W}_{\text{aniso}}$ depends on the symmetries $\mathbf{m}_1$ and $\mathbf{m}_2$ through I_4, I_5, I_6, and I_7. Typically, the term $\bar{W}_{\text{iso}}$ corresponds to the strain energy function of some isotropic material, such as a compressible Mooney-Rivlin material, whereas $\bar{W}_{\text{aniso}}$ accounts for the anisotropy. A simple form for $\bar{W}_{\text{aniso}}$ is given by

$$\bar{W}_{\text{aniso}} = \alpha_1\,(I_4 - 1)^2 + \alpha_2\,(I_5 - 1)^2 + \alpha_3\,(I_6 - 1)^2 + \alpha_4\,(I_7 - 1)^2\,, \tag{3.66}$$

where α_i, $i = 1, 2, 3, 4$, are material parameters. The terms $(I_4 - 1)^2$ and $(I_6 - 1)^2$ are measures of the stretch in the directions $\mathbf{m}_1$ and $\mathbf{m}_2$, respectively; thus, it is associated with the energy required to stretch fibers aligned with $\mathbf{m}_1$ and $\mathbf{m}_2$. The fiber contribution in deformations involving shearing comes from the terms $(I_5 - 1)^2$ and $(I_7 - 1)^2$. A disadvantage of adopting (3.66) is that this model is consistent with linear elasticity only when the elastic constants satisfy certain relations. For instance, in this case, $\mathring{W}_4 = \mathring{W}_5 = \mathring{W}_6 = \mathring{W}_7 = 0$ and we see from the last three equations in (3.63) that this model corresponds to $c_{44} = c_{55} = c_{66}$, which, in general, is not adequate for orthotropic materials.

Bonet and Burton (1998) proposed a strain energy function in the form $\bar{W} = \bar{W}_{\text{iso}} + \bar{W}_{\text{aniso}}$, where $\bar{W}_{\text{iso}} \to \infty$ as $\det \mathbf{F} \to 0$ and $\bar{W}_{\text{aniso}}$ is given by (3.56.c). We use this approach to define the strain energy of the *orthotropic and compressible Mooney-Rivlin*

material as

$$\begin{aligned}\bar{W}(I_1, I_2, I_3, I_4, I_5, I_6, I_7) &= \bar{W}_{\text{iso}}(I_1, I_2, I_3) + \bar{W}_{\text{aniso}}(I_1, I_4, I_5, I_6, I_7)\,,\\ \bar{W}_{\text{iso}}(I_1, I_2, I_3) &= a\,(I_1 - 3) + b\,(I_2 - 3) + c\,(I_3 - 1) - \frac{d}{2}\log I_3\,,\end{aligned} \tag{3.67}$$

where $\bar{W}_{\text{aniso}}$ is given by (3.56.c). Assuming that the material symmetries are given by $\mathbf{m}_1 = \mathbf{e}_1$ and $\mathbf{m}_2 = \mathbf{e}_2$, the restrictions (3.58) and (3.63) yield

$$a = c - \frac{c_{33}}{4} + c_{44} + c_{55} - c_{66}\,, \qquad b = -c + \frac{c_{33}}{4} - \frac{1}{2}\,(c_{44} + c_{55} - c_{66})\,, \qquad d = \frac{c_{33}}{2}\,, \tag{3.68}$$

and (3.65). Therefore, the behavior of this orthotropic and compressible Mooney-Rivlin material is not completely defined by its behavior for infinitesimal deformations. Instead, it has an additional constant, c, which can be used to achieve a good fit between predicted and observed responses for a larger range of deformations in addition to infinitesimal ones. The equation (3.68) can be rewritten so that a or b is the additional constant instead of c. As we will see in Chapter 4, this model yields physically plausible solutions for the disk problem considered therein, whereas the St Venant-Kirchhoff model does not unless we impose the local injectivity condition $\det \mathbf{F} > 0$.

3.4 Elasticity problems

The applied forces introduced in Section 3.1, the equilibrium equation presented in Section 3.2, and the constitutive relations of Section 3.3 yield the necessary tools to define the boundary value problem of the elasticity theory. It follows from (3.2), (3.5), (3.22), (3.24), and (3.26) that the boundary value problem of equilibrium of a hyperelastic solid body consists of finding the deformation field $\mathbf{f}$ that satisfies

$$\begin{cases} \operatorname{Div} \hat{\mathbf{P}}(\mathbf{x}, \nabla\mathbf{f}) + \mathbf{b}(\mathbf{x}) = \mathbf{0}\,, & \mathbf{x} \in \mathcal{B}\,,\\ \mathbf{f}(\mathbf{x}) = \bar{\mathbf{f}}(\mathbf{x})\,, & \mathbf{x} \in \partial_1\mathcal{B}\,,\\ \hat{\mathbf{P}}(\mathbf{x}, \nabla\mathbf{f})\,\mathbf{N}(\mathbf{x}) = \hat{\mathbf{t}}(\mathbf{x}, \nabla\mathbf{f})\,, & \mathbf{x} \in \partial_2\mathcal{B}\,. \end{cases} \tag{3.69}$$

The boundary value problem (3.69) is equivalent to the variational problem of finding a smooth field $\mathbf{f} : \mathcal{B} \to \mathbb{R}^3$ that satisfies the essential boundary condition $\mathbf{f}(\mathbf{x}) = \bar{\mathbf{f}}(\mathbf{x})$ for $\mathbf{x} \in \partial_1\mathcal{B}$ together with the integral equation

$$\int_{\mathcal{B}} \hat{\mathbf{P}}(\mathbf{x}, \nabla\mathbf{f}) \cdot \nabla\mathbf{w}\,\mathrm{d}\mathbf{x} = \int_{\mathcal{B}} \hat{\mathbf{b}}(\mathbf{x}, \mathbf{f}) \cdot \mathbf{w}\,\mathrm{d}\mathbf{x} + \int_{\partial_2\mathcal{B}} \hat{\mathbf{t}}(\mathbf{x}, \nabla\mathbf{f}) \cdot \mathbf{w}\,\mathrm{d}A\,, \tag{3.70}$$

for all smooth enough fields $\mathbf{w} : \mathcal{B} \to \mathbb{R}^3$ such that $\mathbf{w}(\mathbf{x}) = \mathbf{0}$ for $\mathbf{x} \in \partial_1\mathcal{B}$. This variational problem is the mathematical statement of the principle of virtual work in the reference configuration.

In addition, since we assume that $\mathbf{b}$ and $\mathbf{t}$ are conservative forces and the material is hyperelastic, (3.70) can be written as the variation of a functional $\mathcal{E} = \mathcal{E}(\mathbf{f})$ being

null. Therefore, the minimizers of $\mathcal{E}$ are solutions of the variational problem (3.70) and, if they are smooth enough, solutions of the boundary value problem (3.69) as well. This observation leads to a minimization problem, which is of interest to the constrained minimization theory used in this work. This problem consists of finding $\mathbf{f}$ such that

$$\begin{aligned} \mathbf{f} &= \underset{\mathbf{g}\in\mathcal{A}}{\operatorname{argmin}}\, \mathcal{E}(\mathbf{g})\,, \\ \mathcal{E}(\mathbf{g}) &\triangleq \int_{\mathcal{B}} W(\mathbf{x}, \nabla\mathbf{g})\, \mathrm{d}\mathbf{x} - B(\mathbf{g}) - T(\mathbf{g})\,, \end{aligned} \tag{3.71}$$

where $\mathcal{A}$ is a space of smooth enough functions $\mathbf{g} : \mathcal{B} \to \mathbb{R}^3$ such that $\mathbf{g} = \bar{\mathbf{f}}$ in $\partial_1\mathcal{B}$ and B and T are given by (3.6) and (3.8), respectively. The functional $\mathcal{E}$ is called the *total potential energy* and we refer to its minimizers as *stable* deformation fields.

It is common in textbooks to use the axioms of force and moment balance (3.15)-(3.16) to deduce the equation of equilibrium (3.18), which is associated with (3.69.a), and then show the equivalence between (3.69) and the variational problem (3.70) for smooth enough deformation fields. It is also possible to deduce (3.70) directly from the axioms of force and moment balance (3.15)-(3.16) (Ciarlet, 1988). Observe from the problems (3.69) and (3.70) that $\mathbf{f}$ is required to be twice differentiable in the first problem and only differentiable in the second problem. Thus, the smoothness requirement on $\mathbf{f}$ is weaker in the variational problem (3.70) than in the boundary value problem (3.69). For this reason, the forms (3.69) and (3.70) of an elasticity problem are referred to as strong and weak forms, respectively. We have seen from above that the minimization problem (3.71) comes from the variational problem (3.70), which, therefore, does not require $\mathbf{f}$ to be twice differentiable either.

Numerical procedures based on both the variational problem (3.70) and the minimization problem (3.71) are naturally more adequate to find deformation fields $\mathbf{f}$ that are not smooth, such as the case of a finite jump in its gradient, $\nabla\mathbf{f}$, along a certain surface within the body. In this case, Abeyaratne (1983) obtained necessary conditions for $\mathbf{f}$ to be a minimizer of $\mathcal{E}$ considering that the body is subjected to a surface force that is a dead load.

Recall from the paragraph containing (3.11) that we are interested in the case of a pressure load, which is a live load in the sense that it depends on the deformation of the body. Therefore, below, we follow arguments similar to those given by Abeyaratne (1983) to obtain the necessary conditions in the case the surface force is a pressure load.

Let us assume that we search for a minimizer $\mathbf{f}$ of (3.71.b), which is required to be continuous in $\mathcal{B}$ and smooth in $\mathcal{B}\setminus\mathcal{S}$, where $\mathcal{S}\subset\mathcal{B}$ is a regular surface where $\mathbf{F}$ may suffer a finite jump. Also, the surface of discontinuity $\mathcal{S}$, which is not known *a priori*, divides $\mathcal{B}$ into two non-intersecting sub-regions $\mathcal{B}_+$ and $\mathcal{B}_-$ such that $\mathcal{B} = \mathcal{B}_+ \cup \mathcal{B}_- \cup \mathcal{S}$ with the unit outer normal to $\mathcal{S}$ pointing to $\mathcal{B}_+$. This situation is illustrated in Figure 2.

Figure 2 – Illustration of the surface of discontinuity $\mathcal{S}$.

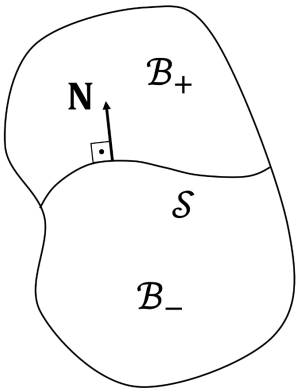

Source: The author.

The continuity of $\mathbf{f}$ implies that $[\mathbf{F}]^+_- \, (\mathbf{I} - \mathbf{N} \otimes \mathbf{N}) \, \mathbf{v} = \mathbf{0}$, $\forall \mathbf{v} \in \mathbb{R}^3$, where $\mathbf{N}$ is a unit normal to $\mathcal{S}$ and $[f]^+_- \triangleq f^+ - f^-$ with f^+ and f^- denoting the limiting values of a field f obtained from approaching a point in $\mathcal{S}$ from $\mathcal{B}_+$ and $\mathcal{B}_-$, respectively (Gurtin, 1993). Since $(\mathbf{I} - \mathbf{N} \otimes \mathbf{N}) \, \mathbf{v} = \mathbf{v} - (\mathbf{v} \cdot \mathbf{N}) \, \mathbf{N}$ is the projection of $\mathbf{v}$ onto the plane normal to $\mathbf{N}$, we find that

$$[\mathbf{F}]^+_- \, \mathbf{L} = \mathbf{0} \, , \tag{3.72}$$

for any vector $\mathbf{L}$ that is tangent to $\mathcal{S}$. Then, using the fact that any $\mathbf{v} \in \mathbb{R}^3$ can be written as $\mathbf{v} = (\mathbf{v} \cdot \mathbf{N}) \, \mathbf{N} + (\mathbf{v} \cdot \mathbf{L}) \, \mathbf{L}$ for some $\mathbf{L}$ orthogonal to $\mathbf{N}$, we can write

$$[\mathbf{F}]^+_- \, \mathbf{v} = [\mathbf{F}]^+_- \, [(\mathbf{v} \cdot \mathbf{N}) \, \mathbf{N} + (\mathbf{v} \cdot \mathbf{L}) \, \mathbf{L}] = (\mathbf{v} \cdot \mathbf{N}) \, [\mathbf{F}]^+_- \, \mathbf{N} = \Big[\Big([\mathbf{F}]^+_- \, \mathbf{N} \Big) \otimes \mathbf{N} \Big] \, \mathbf{v} \tag{3.73}$$

on $\mathcal{S}$ for all $\mathbf{v} \in \mathbb{R}^3$. Therefore, we have that

$$[\mathbf{F}]^+_- = \mathbf{a} \otimes \mathbf{N} \, , \qquad \mathbf{a} \triangleq [\mathbf{F}]^+_- \, \mathbf{N} \, , \qquad \text{on } \mathcal{S} \, . \tag{3.74}$$

Consider that the solid is homogeneous, there is no body force, and the surface load is a pressure load given by (3.13), then, in (3.71.b), $W(\mathbf{x}, \nabla \mathbf{g}) = W(\nabla \mathbf{g})$, $B(\mathbf{g}) = 0$, and $T(\mathbf{g})$ is given by (3.14).

Therefore, the total potential energy functional (3.71.b) can be written as

$$\mathcal{E}(\mathbf{f}) = \mathcal{E}^W(\mathbf{f}) + T(\mathbf{f}) \, , \tag{3.75}$$

where

$$\mathcal{E}^W \triangleq \int_{\mathcal{B}} W(\mathbf{F}) \, \mathrm{d}\mathbf{x} \tag{3.76}$$

and $T(\mathbf{f})$ is given by (3.14). To find necessary conditions for $\mathbf{f}$ to be a minimizer of the functional $\mathcal{E}$, we first determine its variation $\delta\mathcal{E}$ with respect to virtual deformations $\mathbf{f}^* \in \mathcal{A}$, where we recall from (3.71) that $\mathcal{A}$ is the space of admissible deformation fields.

We consider virtual deformations $\mathbf{f}^* : \mathcal{B} \to \mathbb{R}^3$ of the form

$$\mathbf{f}^*(\mathbf{x}^*) = \mathbf{f}(\mathbf{x}) + \delta\mathbf{f}(\mathbf{x})\,, \qquad \mathbf{x}^*(\mathbf{x}) = \mathbf{x} + \delta\mathbf{x}(\mathbf{x})\,, \tag{3.77}$$

where the perturbations $\delta\mathbf{f}$ and $\delta\mathbf{x}$ are smooth with $\delta\mathbf{f} = \mathbf{0}$ on $\partial_1\mathcal{B}$ and $\delta\mathbf{x} = \mathbf{0}$ on $\partial\mathcal{B}$. Since $\partial\mathbf{f}$ is smooth and $\mathbf{f}$ is not smooth on $\mathcal{S}$, we see from (3.77) that $\mathbf{f}^*$ is not smooth on a surface $\mathcal{S}^*$, which is different than $\mathcal{S}$ because of the perturbation $\delta\mathbf{x}$. Therefore, in particular, $\delta\mathbf{x}$ has the effect of perturbing the surface of discontinuity $\mathcal{S}$.

The variations of $\mathcal{E}^W$ and T are given by, respectively,

$$\delta\mathcal{E}^W = \int_{\mathcal{B}} \Big[\mathrm{Div}\,(\mathbf{P}^T\,\overline{\delta\mathbf{f}} + W\,\delta\mathbf{x}) - \overline{\delta\mathbf{f}}\cdot\mathrm{Div}\,\mathbf{P}\Big]\,\mathrm{d}\mathbf{x}\,, \tag{3.78}$$

$$\delta T = p\int_{\mathcal{B}} \left[\mathrm{Div}\,\left(\frac{\partial J}{\partial \mathbf{F}}^T\,\overline{\delta\mathbf{f}} + J\,\delta\mathbf{x}\right) - \overline{\delta\mathbf{f}}\cdot\mathrm{Div}\,\left(\frac{\partial J}{\partial \mathbf{F}}\right)\right]\mathrm{d}\mathbf{x}\,, \tag{3.79}$$

$$\overline{\delta\mathbf{f}} = \delta\mathbf{f} - \mathbf{F}\,\delta\mathbf{x}\,. \tag{3.80}$$

These expressions are obtained by using (B.7) with $g = W$ and $g = -p\,\det\mathbf{F}$. Although Appendix B is focused on the calculations of Section 3.6 below, the equation (B.7) is also valid here.

We then use the divergence theorem, $\delta\mathbf{f} = \mathbf{0}$ on $\partial_1\mathcal{B}$, $\delta\mathbf{x} = \mathbf{0}$ on $\partial\mathcal{B}$, $\partial J/\partial\mathbf{F} = \mathrm{cof}\,\mathbf{F}$, and the Piola's Identity $\mathrm{Div}\,(\mathrm{cof}\,\mathbf{F}) = \mathbf{0}$ to find that

$$\begin{aligned}\delta\mathcal{E}^W = &\int_{\mathcal{S}} \Big\{\delta\mathbf{f}\cdot[\mathbf{P}\,\mathbf{N}]^-_+ + \delta\mathbf{x}\cdot\Big[W\,\mathbf{N} - \mathbf{F}^T\,\mathbf{P}\,\mathbf{N}\Big]^-_+\Big\}\,\mathrm{d}A\\ &+\int_{\partial\mathcal{B}}\delta\mathbf{f}\cdot\mathbf{P}\,\mathbf{N}\,\mathrm{d}A - \int_{\mathcal{B}}\Big(\delta\mathbf{f}\cdot\mathrm{Div}\,\mathbf{P} - \delta\mathbf{x}\cdot\mathbf{F}^T\,\mathrm{Div}\,\mathbf{P}\Big)\,\mathrm{d}A\,,\end{aligned} \tag{3.81}$$

$$\delta T = p\int_{\mathcal{S}}\delta\mathbf{f}\cdot[\mathrm{cof}\,\mathbf{F}\,\mathbf{N}]^-_+\,\mathrm{d}A + p\int_{\partial_2\mathcal{B}}\delta\mathbf{f}\cdot\mathrm{cof}\,\mathbf{F}\,\mathbf{N}\,\mathrm{d}A\,. \tag{3.82}$$

If $\mathbf{f}$ is a minimizer of $\mathcal{E}$, the variation $\delta\mathcal{E} = \delta\mathcal{E}^W + \delta T$ is null. Then, recalling that $\mathbf{F}$ is not defined on $\mathcal{S}$, it follows from (3.81), (3.82), the fundamental lemma of calculus of variations, and the arbitrariness of $\delta\mathbf{f}$ and $\delta\mathbf{x}$, that

$$\begin{cases}\mathrm{Div}\,\mathbf{P} = \mathbf{0} & \text{in } \mathcal{B}\setminus\mathcal{S}\,,\\ \mathbf{f} = \bar{\mathbf{f}} & \text{on } \partial_1\mathcal{B}\,,\\ \mathbf{P}\,\mathbf{N} = -p\,\mathrm{cof}\,\mathbf{F}\,\mathbf{N} & \text{on } \partial_2\mathcal{B}\,,\end{cases} \tag{3.83}$$

and

$$[\mathbf{P}\,\mathbf{N}]^+_- + p\,[\mathrm{cof}\,\mathbf{F}\,\mathbf{N}]^+_- = \mathbf{0} \qquad \text{on } \mathcal{S}\,, \tag{3.84}$$

$$\Big[W\,\mathbf{N} - \mathbf{F}^T\,\mathbf{P}\,\mathbf{N}\Big]^+_- = \mathbf{0} \qquad \text{on } \mathcal{S}\,. \tag{3.85}$$

It follows from (3.74) that $\mathbf{F}^+ = \mathbf{F}^-\,(\mathbf{I} + \bar{\mathbf{a}}\otimes\mathbf{N})$, where $\bar{\mathbf{a}} \triangleq (\mathbf{F}^-)^{-1}\,\mathbf{a}$. Then, using $\mathrm{cof}\,\mathbf{F} = (\det\mathbf{F})\,\mathbf{F}^{-T}$ and the identities, (Gurtin, 1986),

$$\begin{aligned}\det(\mathbf{I} + \bar{\mathbf{a}}\otimes\mathbf{N}) &= 1 + \bar{\mathbf{a}}\cdot\mathbf{N}\,,\\ (\mathbf{I} + \bar{\mathbf{a}}\otimes\mathbf{N})^{-1} &= \mathbf{I} - (1 + \bar{\mathbf{a}}\cdot\mathbf{N})^{-1}\,\bar{\mathbf{a}}\otimes\mathbf{N}\,,\end{aligned} \tag{3.86}$$

it is not difficult to show that $[\operatorname{cof}\mathbf{F}\,\mathbf{N}]^+_- = \mathbf{0}$. Therefore, (3.84) becomes

$$[\mathbf{P}\,\mathbf{N}]^+_- = \mathbf{0} \qquad \text{on } \mathcal{S}\,. \tag{3.87}$$

Next, note that (3.85) corresponds to three scalar equations, which can be obtained by taking the dot product of (3.85) with three linearly independent vectors. Let us take the dot product of (3.85) with the unit normal $\mathbf{N}$ and two non-collinear tangent vectors $\mathbf{L}_1$ and $\mathbf{L}_2$. The dot product with $\mathbf{N}$ yields the scalar equation

$$[W - \mathbf{F}\,\mathbf{N}\cdot\mathbf{P}\,\mathbf{N}]^+_- = 0 \qquad \text{on } \mathcal{S} \tag{3.88}$$

and, using (3.87), the dot product with $\mathbf{L}_\alpha$, $\alpha = 1, 2$, yields

$$\left([\mathbf{F}]^+_-\,\mathbf{L}_\alpha\right)\cdot\mathbf{P}^+\,\mathbf{N} = 0 \qquad \text{on } \mathcal{S}\,, \qquad \alpha = 1, 2\,, \tag{3.89}$$

which is trivially satisfied because of (3.72). Therefore, the vector equation (3.85) is equivalent to the scalar equation (3.88).

Thus, (3.83) together with the continuity conditions (3.87) and (3.88) are necessary conditions for a continuous and non-smooth deformation field $\mathbf{f}$ with a jump in $\mathbf{F}$ across $\mathcal{S} \subset \mathcal{B}$ to be a minimizer of the total potential energy functional in the case the surface force is a pressure load, the solid is homogeneous, and there is no body force.

Except for (3.83.c), which is clearly specific for the pressure load given by (3.13), these necessary conditions are the same conditions obtained by Abeyaratne (1983), who considered that the surface force is a dead load. In addition, if $\mathbf{f}$ is smooth, then (3.83), (3.87), and (3.88) reduce to (3.69), when $\mathbf{b}(\mathbf{x}) = \mathbf{0}$ and $\hat{\mathbf{t}}$ is given by (3.13).

Note that, if we were to consider a virtual deformation given by (3.77) with $\delta\mathbf{x} \equiv \mathbf{0}$, the terms that multiply $\delta\mathbf{x}$ in (3.81) and (3.82) would not appear. Therefore, we would find (3.83) and (3.87), but not (3.88). Recall from the discussion below (3.77) that the case $\delta\mathbf{x} \equiv \mathbf{0}$ correspond to a virtual deformation which does not perturb the surface $\mathcal{S}$. Thus, the continuity condition (3.88) comes from a perturbation of the surface $\mathcal{S}$, whereas the other conditions can be found without perturbing $\mathcal{S}$.

The continuity condition (3.87) corresponds to the requirement that the traction $\mathbf{PN}$ be continuous across $\mathcal{S}$ and is, therefore, known as the *traction continuity condition*. As shown by Knowles (1979), this condition corresponds to an equilibrium of forces at a point on $\mathcal{S}$. By considering a quasi-static time-dependent family of equilibrium states, this author introduced a dissipation condition, which is given by (3.88) with the $=$ sign replaced with $\geq$. For this reason, we refer to (3.88) as the *dissipation-free condition*. In addition, (3.88) is also known as Maxwell relation (Silhavy, 1997). In one dimension, the conditions (3.87) and (3.88) correspond to the Weierstrass-Erdmann corner conditions in the context of continuum mechanics and yield the equal-area rule presented by Ericksen (1975).

In this work, we only consider the type of non-smoothness defined above, that is, a *non-smooth field* that is continuous and has a finite jump in its spatial derivative at a point or on a surface within its domain.

3.5 Strong Ellipticity conditions

We say that the equation of equilibrium (3.69.a) and the elasticity tensor $\hat{\mathbb{C}}(\mathbf{x}, \nabla\mathbf{f})$, given by (3.38), are strongly elliptic at $\mathbf{x}$ and $\mathbf{f}$ if

$$(\mathbf{a}\otimes\mathbf{b})\cdot\hat{\mathbb{C}}(\mathbf{x},\nabla\mathbf{f})[\mathbf{a}\otimes\mathbf{b}] > 0\,, \qquad \forall\,\mathbf{a},\mathbf{b}\in\mathbb{R}^3\setminus\{\mathbf{0}\}\,. \tag{3.90}$$

Let us consider a class of hyperelastic orthotropic materials, which has the material symmetry directions $\mathbf{m}_1, \mathbf{m}_2 \in \mathbb{R}^3$ and a strain energy function $\tilde{W}(\mathbf{x}, \mathbf{C})$ that can be written as

$$\tilde{W}(\mathbf{x},\mathbf{C}) = \bar{W}(\mathbf{x}, \iota_{\mathbf{C}})\,, \tag{3.91}$$

where $\bar{W} : \mathbb{R}^3 \times (\mathbb{R})^7 \to \mathbb{R}$ and $\iota_{\mathbf{C}}$ is the list of the sevens invariants I_i, $i = 1, 2, ..., 7$, given by (3.51) and (3.52) Also, let $\{\mathbf{e}_1, \mathbf{e}_2, \mathbf{e}_3\}$ denote the principal directions of $\mathbf{C}$ or, equivalently, of the right stretch tensor $\mathbf{U} \triangleq \sqrt{\mathbf{C}}$. If $\mathbf{m}_1 = \mathbf{e}_1$, $\mathbf{m}_2 = \mathbf{e}_2$, and the deformation field $\mathbf{f}$ corresponds to a plane strain state in the plane spanned by $\mathbf{e}_1$ and $\mathbf{e}_2$, necessary and sufficient conditions to the strong ellipticity condition (3.90) to be satisfied for $\mathbf{a}$ and $\mathbf{b}$ in this plane are given by, (Aguiar, 2019),

$$Q_{11} > 0\,, \qquad Q_{22} > 0\,, \qquad Q_{12} > 0\,, \qquad Q_{21} > 0\,, \qquad Q_* > 0\,, \tag{3.92}$$

where

$$\begin{aligned}
Q_{11} &\triangleq 2\left\{u_1^{-2}(\bar{W}_1+\bar{W}_4) + 2\left[\bar{W}_{11}+\bar{W}_{44}+\frac{1}{2}\,\bar{W}_3\,I_3\,u_1^{-4}\right.\right.\\
&\qquad \left.\left. + I_3\,u_1^{-2}\,(I_3\,\bar{W}_{33}\,u_1^{-2} + 2\,\bar{W}_{13}) + 2\,(\bar{W}_{14} + I_3\,\bar{W}_{34}\,u_1^{-2})\right]\right\},\\
Q_{22} &\triangleq 2\left\{u_2^{-2}\,\bar{W}_1 + 2\left[\bar{W}_{11} + \frac{1}{2}\,\bar{W}_3\,I_3\,u_2^{-4} + I_3\,u_2^{-2}\,(I_3\,\bar{W}_{33}\,u_2^{-2} + 2\,\bar{W}_{13})\right]\right\},\\
Q_{12} &\triangleq 2\,u_1^{-2}\,\bar{W}_1\,, \qquad Q_{21} \triangleq 2\,u_2^{-2}\,(\bar{W}_1+\bar{W}_4)\,,\\
Q_* &\triangleq \sqrt{Q_{11}\,Q_{22}} + \sqrt{Q_{12}\,Q_{21}} - 2\,|Q_{66}|\,,\\
Q_{66} &\triangleq \bar{W}_3 + 2\,(\bar{W}_{11} + I_3\,\bar{W}_{33} + I_1\,\bar{W}_{13} + \bar{W}_{14} + \bar{W}_{34}\,u_1^2)\,.
\end{aligned} \tag{3.93}$$

In (3.93), $\bar{W}_i \triangleq \partial\bar{W}/\partial I_i$, $\bar{W}_{ij} \triangleq \partial^2\bar{W}/\partial I_i\,\partial I_j$, $i, j = 1, 2, 3, ..., 7$, and u_1, u_2 are the principal stretches, that is, the eigenvalues of $\mathbf{U}$ associated with the principal directions $\mathbf{e}_1$, $\mathbf{e}_2$, respectively.

Assuming that the reference configuration is a natural state, where $\mathbf{F} = \mathbf{I}$, and that there is no residual stress, the conditions (3.92) and (3.93) evaluated at the reference configuration take the form, (Aguiar, 2019),

$$\begin{aligned}
&Q_{11} = c_{11} > 0\,, \qquad Q_{22} = c_{22} > 0\,, \qquad Q_{12} = Q_{21} = c_{66} > 0\,,\\
&Q_* = \sqrt{c_{11}\,c_{22}} + c_{66} - |c_{66} + c_{12}| > 0\,.
\end{aligned} \tag{3.94}$$

The strong ellipticity condition (3.90) implies that, given arbitrary vectors $\mathbf{a}$ and $\mathbf{b}$, the function $\mathbf{a}\cdot\mathbf{F}\,\mathbf{b}\mapsto\mathbf{a}\cdot\hat{\mathbf{P}}(\mathbf{x},\mathbf{F})\,\mathbf{b}$ is strictly increasing. This is a mathematical way to represent the idea that a body should elongate in the direction of the applied force (Antman, 2005). However, there are cases in which this monotonic behavior is not desirable. For instance, as mentioned in Chapter 2, non-monotonic responses have been proposed to model materials that can undergo multiple solid phases or strain localization. This type of non-monotonic response may yield a deformation field that has a jump in its gradient and is in good agreement with experimental results. In fact, this type of non-smooth deformation field is only possible if the strong ellipticity condition is violated at some deformation field (Knowles; Sternberg, 1978; Gurtin, 1986).

3.6 The constrained minimization theory

We have seen in Chapter 2 that, in the context of the classical linear elasticity theory, there are problems whose solutions predict self-intersection even though the applied load is small. One way to prevent this unphysical behavior is to impose the local injectivity constraint, $\det\mathbf{F}>0$, as it was done by Fosdick and Royer-Carfagni (2001). One of our objectives is to study this constrained minimization theory in the context of the nonlinear elasticity theory since the violation of the constraint $\det\mathbf{F}>0$ is associated with large deformations.

We consider the constrained minimization problem

$$\min_{\mathbf{f}\in\mathcal{A}_\varepsilon}\mathcal{E}(\mathbf{f})\,, \tag{3.95}$$

where

$$\mathcal{A}_\varepsilon\triangleq\{\mathbf{f}:\mathcal{B}\to\mathbb{R}^3\,|\,c(\mathbf{F})\triangleq\det\mathbf{F}-\varepsilon\geq 0\} \tag{3.96}$$

for smooth enough deformations $\mathbf{f}$, ε is a small positive parameter, and, assuming that the body is homogeneous, $\mathcal{E}$ is given by

$$\mathcal{E}(\mathbf{f})=\int_{\mathcal{B}}W(\mathbf{F})\,\mathrm{d}\mathbf{x}-B(\mathbf{f})-T(\mathbf{f})\,, \tag{3.97}$$

where $B(\mathbf{f})$ and $T(\mathbf{f})$ are the potentials associated with the loads $\mathbf{b}$ and $\mathbf{t}$, respectively. Recall from Section 3.1 that if both $\mathbf{b}$ and $\mathbf{t}$ are dead loads, $B(\mathbf{f})$ and $T(\mathbf{f})$ are given by (3.10) and, for the pressure load, $T(\mathbf{f})$ is given (3.14).

We now introduce the sets

$$\mathcal{B}_{=}\triangleq\operatorname{int}\left[\{\mathbf{x}\in\mathcal{B}\,|\,c(\mathbf{F}(\mathbf{x}))=0\}\right],\qquad\mathcal{B}_{>}\triangleq\operatorname{int}\left[\{\mathbf{x}\in\mathcal{B}\,|\,c(\mathbf{F}(\mathbf{x}))>0\}\right], \tag{3.98}$$

where $\operatorname{int}[\cdot]$ denotes the interior of a set, such that $\mathcal{B}=\mathcal{B}_{>}\cup\mathcal{B}_{=}\cup\Sigma$, where $\mathcal{B}_{>}\cap\mathcal{B}_{=}=\emptyset$ and $\Sigma\triangleq\bar{\mathcal{B}}_{>}\cap\bar{\mathcal{B}}_{=}$ denotes the interface between $\mathcal{B}_{>}$ and $\mathcal{B}_{=}$ with unit normal $\mathbf{N}$ pointing towards $\mathcal{B}_{>}$. In addition, let $\partial_2\mathcal{B}_{>}\triangleq\bar{\mathcal{B}}_{>}\cap\partial_2\mathcal{B}$ and $\partial_2\mathcal{B}_{=}\triangleq\bar{\mathcal{B}}_{=}\cap\partial_2\mathcal{B}$ denote, respectively, the parts of the boundaries of $\mathcal{B}_{>}$ and $\mathcal{B}_{=}$ belonging to $\partial_2\mathcal{B}$.

We then assume that there exists a Lagrange multiplier field $\lambda : \mathcal{B} \to \mathbb{R}$ associated with the local injectivity constraint $c(\mathbf{F}) \geq 0$, such that $\lambda = 0$ in $\mathcal{B}_> \cup \partial_2\mathcal{B}_>$. In this case, a minimizer of (3.97) is also a minimizer of the functional

$$\mathcal{E}_a(\mathbf{f}, \lambda) = \mathcal{E}_a^W(\mathbf{f}, \lambda) - B(\mathbf{f}) - T(\mathbf{f}) \,, \tag{3.99}$$

where

$$\mathcal{E}_a^W(\mathbf{f}, \lambda) \triangleq \int_{\mathcal{B}} W_a(\mathbf{F}, \lambda) \, \mathrm{d}\mathbf{x} \,, \qquad W_a(\mathbf{F}, \lambda) \triangleq W(\mathbf{F}) - \lambda \, c(\mathbf{F}) \,. \tag{3.100}$$

Next, we calculate the variation of $\mathcal{E}_a$, which we denote by $\delta\mathcal{E}_a$, with respect to admissible deformations $\mathbf{f}^* \in \mathcal{A}_\varepsilon$ and Lagrange multiplier fields λ^* having the form

$$\mathbf{f}^*(\mathbf{x}^*) = \mathbf{f}(\mathbf{x}) + \delta\mathbf{f}(\mathbf{x}) \,, \quad \lambda^*(\mathbf{x}^*) = \lambda(\mathbf{x}) + \delta\lambda(\mathbf{x}) \,, \quad \mathbf{x}^*(\mathbf{x}) = \mathbf{x} + \delta\mathbf{x}(\mathbf{x}) \,, \tag{3.101}$$

where the perturbations $\delta\mathbf{f}$, $\delta\lambda$, $\delta\mathbf{x}$ are smooth and satisfy $\delta\mathbf{f} = \mathbf{0}$ on $\partial_1\mathcal{B}$, $\delta\lambda = 0$ in $\mathcal{B}_> \cup \partial_2\mathcal{B}_>$, and $\delta\mathbf{x} = \mathbf{0}$ on $\partial\mathcal{B}$.

Abeyaratne (1983) used perturbations of the domain to study conditions that must hold on an internal surface $\mathcal{S} \subset \mathcal{B}$, across which the deformation gradient $\mathbf{F}$ may suffer a finite jump. His study does not involve the imposition of the local injectivity constraint. Here, we assume that $\mathbf{F}$ may be discontinuous not only across $\mathcal{S}$, but also across Σ, where $\mathcal{S} \cap \Sigma = \emptyset$. This assumption is used below when we apply the divergence theorem.

For B and T having the forms (3.10) and (3.14), the first variation of $\mathcal{E}_a$ is given by

$$\delta\mathcal{E}_a = \delta\mathcal{E}_a^W - \delta B - \delta T \,, \tag{3.102}$$

where (see Appendix B)

$$\delta\mathcal{E}_a^W = \int_{\mathcal{B}} \left[\mathrm{Div}\left(\frac{\partial W_a}{\partial \mathbf{F}}^T \overline{\delta\mathbf{f}} + W_a \, \delta\mathbf{x} \right) - \overline{\delta\mathbf{f}} \cdot \mathrm{Div}\left(\frac{\partial W_a}{\partial \mathbf{F}} \right) + \frac{\partial W_a}{\partial \lambda} \, \overline{\delta\lambda} \right] \mathrm{d}\mathbf{x} \,, \tag{3.103}$$

$$\delta T = \begin{cases} \int_{\partial_2\mathcal{B}} \mathbf{t} \cdot \delta\mathbf{f} \, \mathrm{d}\mathbf{x} \,, & \text{(dead load)} \,, \\ -p \int_{\mathcal{B}} \left[\mathrm{Div}\left(\dfrac{\partial J}{\partial \mathbf{F}}^T \overline{\delta\mathbf{f}} + J \, \delta\mathbf{x} \right) - \overline{\delta\mathbf{f}} \cdot \mathrm{Div}\left(\dfrac{\partial J}{\partial \mathbf{F}} \right) \right] \mathrm{d}\mathbf{x} \,, & \text{(pressure load)} \,, \end{cases} \tag{3.104}$$

$$\delta B = \int_{\mathcal{B}} \left\{ \mathrm{Div}\left[(\mathbf{b} \cdot \mathbf{f}) \, \delta\mathbf{x} \right] + \mathbf{b} \cdot \overline{\delta\mathbf{f}} \right\} \mathrm{d}\mathbf{x} \,, \tag{3.105}$$

$$\overline{\delta\mathbf{f}} = \delta\mathbf{f} - \mathbf{F} \, \delta\mathbf{x} \,, \qquad \overline{\delta\lambda} = \delta\lambda - \nabla\lambda \cdot \delta\mathbf{x} \,, \tag{3.106}$$

and $J \triangleq \det \mathbf{F}$.

We then use (3.100.b), the divergence theorem, $\delta\mathbf{f} = \mathbf{0}$ on $\partial_1\mathcal{B}$, $\delta\mathbf{x} = \mathbf{0}$ on $\partial\mathcal{B}$, $\partial J/\partial\mathbf{F} = \mathrm{cof}\,\mathbf{F}$, the Piola's identity $\mathrm{Div}\,(\mathrm{cof}\,\mathbf{F}) = \mathbf{0}$, $c(\mathbf{F}) = 0$ in $\mathcal{B}_=$, and $\lambda = 0$ in $\mathcal{B}_> \cup \partial_2\mathcal{B}_>$ to find that

$$\begin{aligned} \delta\mathcal{E}_a^W = & \int_{\Sigma\cup\mathcal{S}} \left\{ \delta\mathbf{f} \cdot [\mathbf{P}_a]_+^- \, \mathbf{N} + \delta\mathbf{x} \cdot \left[W \, \mathbf{N} + \mathbf{F}^T \, \mathbf{P}_a \, \mathbf{N} \right]_+^- \right\} \mathrm{d}A \\ & + \int_{\partial_2\mathcal{B}} \delta\mathbf{f} \cdot \mathbf{P}_a \, \mathbf{N} \, \mathrm{d}A - \int_{\mathcal{B}} \left(\delta\mathbf{f} \cdot \mathrm{Div}\, \mathbf{P}_a - \delta\mathbf{x} \cdot \mathbf{F}^T \, \mathrm{Div}\, \mathbf{P}_a \right) \mathrm{d}\mathbf{x} \,, \end{aligned} \tag{3.107}$$

$$\delta T = \begin{cases} \int_{\partial_2\mathcal{B}} \mathbf{t}\cdot\delta\mathbf{f}\,\mathrm{d}\mathbf{x}\,, & \text{(dead load)}\,, \\ -p\int_{\Sigma\cup\mathcal{S}} \delta\mathbf{f}\cdot[\operatorname{cof}\mathbf{F}]_+^-\,\mathbf{N}\,\mathrm{d}A - p\int_{\partial_2\mathcal{B}}\delta\mathbf{f}\cdot\operatorname{cof}\mathbf{F}\,\mathbf{N}\,\mathrm{d}A\,, & \text{(pressure load)}\,, \end{cases} \tag{3.108}$$

$$\delta B = \int_{\mathcal{B}} \Big(\delta\mathbf{f}\cdot\mathbf{b} - \delta\mathbf{x}\cdot\mathbf{F}^T\,\mathbf{b}\Big)\,\mathrm{d}\mathbf{x}\,, \tag{3.109}$$

where

$$\mathbf{P}_a \triangleq \frac{\partial W_a}{\partial\mathbf{F}} = \mathbf{P} - \lambda\operatorname{cof}\mathbf{F} \tag{3.110}$$

and $[\,\cdot\,]_+^- \triangleq (\cdot)^- - (\cdot)^+$ with $(\cdot)^+$ and $(\cdot)^-$ indicating that the evaluations of $(\cdot)$ are understood as limit values as we approach the surfaces Σ and $\mathcal{S}$ from their corresponding positive and negative sides, respectively. The positive side of these surfaces is that towards their normal $\mathbf{N}$ points and the negative side is the opposite side. Recall from above that $\lambda = 0$ in $\mathcal{B}_> \cup \partial_2\mathcal{B}_>$, thus, $\mathbf{P}_a = \mathbf{P}$ in $\mathcal{B}_> \cup \partial_2\mathcal{B}_>$. See Appendix B for further details about the derivation of (3.103)-(3.109).

The variation $\delta\mathcal{E}_a$, which is given by (3.102) together with (3.107)-(3.110), vanishes at a minimizer $\mathbf{f}$ of the functional $\mathcal{E}$. Since the perturbation $\delta\mathbf{f}$ is arbitrary in $\mathcal{B}_> \cup \partial_2\mathcal{B}_>$, it follows from the fundamental lemma of calculus of variations that the coefficients of $\delta\mathbf{f}$ are null in $\mathcal{B}_> \cup \partial_2\mathcal{B}_>$. The same is true in $\mathcal{B}_=$, but with a different reasoning. Following the arguments in Section 4.5 of Kirk (2004), we have that, in $\mathcal{B}_= \cup \partial_2\mathcal{B}_=$, two of the components of $\delta\mathbf{f}$, say the first two, are arbitrary, whereas the remaining component, say the last one, is chosen so that the scalar constraint $c(\mathbf{F}) = 0$ is satisfied. Since in the above equations $\lambda(\mathbf{x})$ is arbitrary in $\mathcal{B}_= \cup \partial_2\mathcal{B}_=$, we select $\lambda(\mathbf{x})$ so that the last component of the coefficients of $\delta\mathbf{f}$ is zero. Here, such a value of $\lambda(\mathbf{x})$ is assumed to exist; later, in Chapter 5, we verify this assumption by determining $\lambda(\mathbf{x})$ numerically. Then, it follows from the arbitrariness of the first two components of $\delta\mathbf{f}$ that the first two components of the coefficients of $\delta\mathbf{f}$ are also null.

Recalling that $\mathbf{F}$ is not defined on $\Sigma\cup\mathcal{S}$ and $\mathbf{t}$ is given by (3.13) for a pressure load, the above considerations on $\delta\mathbf{f}$ lead to the Euler-Lagrange equation

$$\operatorname{Div}\mathbf{P}_a + \mathbf{b} = \mathbf{0} \quad \text{in } \mathcal{B}\setminus(\Sigma\cup\mathcal{S})\,, \tag{3.111}$$

the traction condition

$$\mathbf{P}_a\,\mathbf{N} = \mathbf{t} \quad \text{on } \partial_2\mathcal{B}\,, \tag{3.112}$$

where, here, $\mathbf{N}$ is the unit normal to $\partial_2\mathcal{B}$, and the jump condition

$$\begin{cases} [\mathbf{P}_a\,\mathbf{N}]_-^+ = \mathbf{0}\,, & \text{if } \mathbf{t} \text{ is a dead load}\,, \\ [\mathbf{P}_a\,\mathbf{N}]_-^+ + p\,[\operatorname{cof}\mathbf{F}]_-^+\,\mathbf{N} = \mathbf{0}\,, & \text{if } \mathbf{t} \text{ is a pressure load}\,, \end{cases} \tag{3.113}$$

on $\Sigma\cup\mathcal{S}$, where $\mathbf{N}$ is the unit normal to $\Sigma\cup\mathcal{S}$. In addition, $\delta\mathbf{x}$ is arbitrary in the interior of $\mathcal{B}$, yielding

$$[W\,\mathbf{N} + \mathbf{F}^T\,\mathbf{P}_a\,\mathbf{N}]_-^+ = \mathbf{0} \qquad \text{on } \Sigma\cup\mathcal{S}\,. \tag{3.114}$$

Then, the same arguments used in Section 3.4 to obtain (3.87) and (3.88) from (3.84) and (3.85), respectively, can be used to show that (3.113) and (3.114) are respectively equivalent to

$$[\mathbf{P}_a\,\mathbf{N}]^+_- = \mathbf{0} \qquad \text{on } \Sigma \cup \mathcal{S}\,, \tag{3.115}$$

$$[W + \mathbf{F}\,\mathbf{N}\cdot\mathbf{P}_a\,\mathbf{N}]^+_- = 0 \qquad \text{on } \Sigma \cup \mathcal{S}\,. \tag{3.116}$$

Thus, the necessary conditions for a deformation field to be a minimizer of the minimization problem (3.95) consist of the Euler-Lagrange equation (3.111), the traction condition (3.112), the continuity of traction (3.115), and the scalar equation (3.116).

Remark 1 (Constrained linear theory). If $\mathbf{F}$ is continuous across $\Sigma \cup \mathcal{S}$, which means that $\mathbf{F}^+ = \mathbf{F}^-$, using (3.115), we find that (3.116) is trivially satisfied. It follows from (3.110), $\det\mathbf{F} = \varepsilon$ in $\mathcal{B}_=$, and $\operatorname{cof}\mathbf{F} = (\det\mathbf{F})\,\mathbf{F}^{-T}$ that $\mathbf{P}_a = \mathbf{P} - \lambda\,\varepsilon\,\mathbf{F}^{-T}$ in $\mathcal{B}_=$. Therefore, (3.111), (3.112), and (3.115) have the same form of the equations of the constrained minimization theory proposed by Fosdick and Royer-Carfagni (2001) if we replace $\mathbf{P}$ with the stress tensor of the classical linear elasticity theory.

4 THE UNCONSTRAINED DISK PROBLEM

In this chapter, we consider the problem of a radially reinforced annular disk that is fixed on its inner surface and compressed by a uniform pressure on its outer surface. No body force acts on the disk. We investigate the solutions predicted by the orthotropic St Venant-Kirchhoff and Mooney-Rivlin models without imposing the local injectivity constraint. For comparison purposes, we also consider the analogous problem in the context of the classical linear elasticity theory.

4.1 Formulation of the problem

Let $\{\mathbf{e}_R, \mathbf{e}_\Theta, \mathbf{e}_Z\}$ denote the usual orthonormal cylindrical basis at $\mathbf{x}$ associated with the cylindrical coordinates (R, Θ, Z), such that $\mathbf{x} = R\,\mathbf{e}_R(\Theta) + Z\,\mathbf{e}_Z$. Similarly, let $\{\mathbf{e}_r, \mathbf{e}_\theta, \mathbf{e}_z\}$ and (r, θ, z) be the corresponding orthonormal cylindrical basis and coordinates, respectively, at $\mathbf{y}$, such that $\mathbf{y} = r\,\mathbf{e}_r(\theta) + z\,\mathbf{e}_z$. Unless stated otherwise, we omit the dependence of $\mathbf{e}_R$ and $\mathbf{e}_r$ on the azimuth.

We consider the problem of equilibrium of an elastic annular disk with uniform unitary thickness in the absence of body force, so that $\mathbf{b} = \mathbf{b}_\mathbf{f} = \mathbf{0}$. The disk is fixed on its inner surface of radius $R_i \geq 0$ and compressed by a uniform pressure $p > 0$ on its outer surface of radius $R_e > R_i$. The disk is homogeneous and made of a *cylindrically orthotropic* material, that is, it is orthotropic with respect to the planes that are normal to $\mathbf{e}_R$, $\mathbf{e}_\Theta$, $\mathbf{e}_Z$. In Figure 3, we show an illustration of the disk problem.

Figure 3 – Illustration of the disk problem.

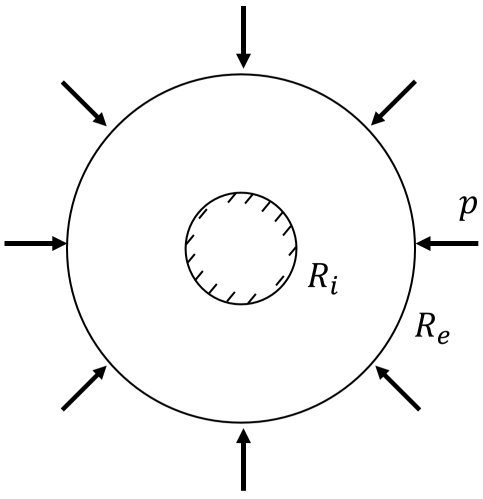

Source: The author.

We want to find a *radially symmetric* deformation field $\mathbf{f}$, such that points $\mathbf{x} \in \mathcal{B}$ move along radial lines according to

$$\mathbf{f}(R, \Theta, Z) = r(R)\, \mathbf{e}_r(\Theta) + Z\, \mathbf{e}_z\,, \tag{4.1}$$

or, equivalently,

$$\mathbf{u}(R, \Theta, Z) = u_r(R)\, \mathbf{e}_R\,, \qquad u_r(R) = r(R) - R\,. \tag{4.2}$$

Since $\mathbf{F} \triangleq \nabla \mathbf{f}$, we have that

$$\begin{gathered} \mathbf{F} = \nu(R)\, \mathbf{e}_r \otimes \mathbf{e}_R + \tau(R)\, \mathbf{e}_\theta \otimes \mathbf{e}_\Theta + \mathbf{e}_z \otimes \mathbf{e}_Z\,, \\ \nu(R) \triangleq r'(R)\,, \quad \tau(R) \triangleq \frac{r(R)}{R}\,, \end{gathered} \tag{4.3}$$

where the explicit dependence on $\mathbf{x} = (R, \Theta, Z)$ is omitted and $(\cdot)'$ denotes the derivative with respect to R. In addition, it follows from (4.3) that

$$\det \mathbf{F} = \nu(R)\, \tau(R)\,. \tag{4.4}$$

For comparison purposes, we consider two material models. The first model concerns an orthotropic St Venant-Kirchhoff material, whose strain energy density function is given by (3.46), where the nonzero components of $\mathbb{C}$ with respect to $\{\mathbf{e}_R, \mathbf{e}_\Theta, \mathbf{e}_Z\}$ are given by (3.48) with the subscripts 1, 2, 3 denoting the directions $\mathbf{e}_R$, $\mathbf{e}_\Theta$, $\mathbf{e}_Z$, respectively. The second model concerns an orthotropic and compressible Mooney-Rivlin material, whose strain energy function is given by (3.67), (3.68), (3.56.c), and (3.65), which means that $\mathbf{m}_1 = \mathbf{e}_R$ and $\mathbf{m}_2 = \mathbf{e}_\Theta$.

It follows from (3.21) and (4.3.a) that

$$\mathbf{P} = P_{rr}(R)\, \mathbf{e}_r \otimes \mathbf{e}_R + P_{\theta\theta}(R)\, \mathbf{e}_\theta \otimes \mathbf{e}_\Theta + P_{zz}(R)\, \mathbf{e}_z \otimes \mathbf{e}_Z\,, \tag{4.5}$$

where the components of $\mathbf{P}$ are given by

$$P_{rr}(R) = \hat{P}^{\mathrm{vk}}_{rr}(\nu, \tau) \triangleq \frac{\nu}{2}\left[c_{11}\,(\nu^2 - 1) + c_{12}\,(\tau^2 - 1)\right], \tag{4.6}$$

$$P_{\theta\theta}(R) = \hat{P}^{\mathrm{vk}}_{\theta\theta}(\nu, \tau) \triangleq \frac{\tau}{2}\left[c_{12}\,(\nu^2 - 1) + c_{22}\,(\tau^2 - 1)\right], \tag{4.7}$$

for the St Venant-Kirchhoff material and by

$$P_{rr}(R) = \hat{P}^{\mathrm{mr}}_{rr}(\nu, \tau) \triangleq \hat{P}^{\mathrm{vk}}_{rr}(\nu, \tau) - \frac{c_{33}}{2\,\nu}\,(\nu^4 - 2\,\nu^2 + 1)\,, \tag{4.8}$$

$$P_{\theta\theta}(R) = \hat{P}^{\mathrm{mr}}_{\theta\theta}(\nu, \tau) \triangleq \hat{P}^{\mathrm{vk}}_{\theta\theta}(\nu, \tau) - \frac{c_{33}}{2\,\tau}\,(\tau^4 - 2\,\tau^2 + 1)\,, \tag{4.9}$$

for the Mooney-Rivlin material. The expressions of P_{zz} were omitted because they do not contribute to the governing equations of equilibrium. In this work, we will use $\hat{P}_{rr}$ and $\hat{P}_{\theta\theta}$ to represent the response functions of P_{rr} and $P_{\theta\theta}$, respectively, without distinguishing between the St Venant-Kirchhoff and Mooney-Rivlin materials.

Observe from (4.6)-(4.9) that the stress responses of the Mooney-Rivlin material are equal to the corresponding responses of the St Venant-Kirchhoff material plus a term that depends on c_{33}. We will see in Section 4.3.3 that this additional term plays a fundamental role to prevent self-intersection of the Mooney-Rivlin material. For a large enough traction, where $\nu, \tau > 1$, the sign of $\hat{P}_{rr}^{\mathrm{mr}}$ is given by the sign of $(c_{11} - c_{33})\,\nu^3 + c_{12}\,\nu\,\tau^2$, which is negative if c_{33} is sufficiently larger than c_{11}. This is not realistic, so we limit our studies to the case $c_{33} \leq c_{11}$. The same argument applied to $\hat{P}_{\theta\theta}^{\mathrm{mr}}$ yields $c_{33} \leq c_{22}$. In addition, recall from the beginning of this section that the disk is radially reinforced, which yields $c_{11} > c_{22}$. Therefore, we focus our study in the case $c_{11} > c_{22} \geq c_{33}$.

Recall from above that, to obtain (4.6)-(4.9), we have considered $\mathbf{m}_1 = \mathbf{e}_R$ and $\mathbf{m}_2 = \mathbf{e}_\Theta$. The directions $\mathbf{m}_1$ and $\mathbf{m}_2$ are usually associated with the directions of fiber reinforcements, thus, c_{33} is indeed expected to be lower than c_{11} and c_{22}. In addition, if we were to consider $\mathbf{m}_1 = \mathbf{e}_R$ and $\mathbf{m}_2 = \mathbf{e}_Z$, we would obtain (4.6)-(4.9) with c_{33} replaced with c_{22}. Thus, c_{33} would not influence P_{rr} and $P_{\theta\theta}$. Also, the analysis of the sign of $\hat{P}_{rr}^{\mathrm{mr}}$ would yield $c_{11} > c_{22}$, which, again, is in agreement with the idea of $\mathbf{m}_1$ and $\mathbf{m}_2$ being directions of reinforcements. Therefore, these results indicate that the considered orthotropic and compressible Mooney-Rivlin material is adequate to model fiber-reinforced composites subjected to compression or traction; however, it is not adequate to represent materials with aligned flaws, such as voids or flexible fibers, under traction.

Substituting (4.5) into the vector equilibrium equation (3.69.a), we find that this equation reduces to the scalar ordinary differential equation given by

$$\frac{\mathrm{d}}{\mathrm{d}R}\left[R\,P_{rr}(R)\right] - P_{\theta\theta}(R) = 0\,. \tag{4.10}$$

Also, from (4.3) and (3.13), the boundary conditions in (3.69.b,c) for the disk problem reduce to, respectively,

$$r(R_i) = R_i\,, \qquad P_{rr}(R_e) = -p\,\frac{r(R_e)}{R_e}\,, \tag{4.11}$$

where the pressure $p > 0$ is constant.

Thus, the *disk boundary value problem (disk BVP)* consists of finding $r : [R_i, R_e] \to \mathbb{R}$ that satisfies the ordinary differential equation (4.10), the boundary conditions (4.11), and either (4.6)-(4.7) for the St Venant-Kirchhoff material or (4.8)-(4.9) for the Mooney-Rivlin material, where ν and τ are given by (4.3). A detailed investigation of the disk BVP is presented in Section 4.3.

In addition, we define the *disk minimization problem (disk MP)* as the problem of finding a radial displacement field $u_r : [R_i, R_e] \to \mathbb{R}$ that satisfies $u_r(R_i) = 0$ and minimizes the functional

$$\check{\mathcal{E}}(u_r) \triangleq \mathcal{E}(\mathbf{f})\,, \tag{4.12}$$

where $\mathbf{f} = \mathbf{x} + \mathbf{u}$ and $\mathcal{E}(\mathbf{f})$ is given by (3.97) together with (4.2), (3.14), $B(\mathbf{f}) = 0$, and either (3.46) for the St Venant-Kirchhoff material or (3.67) for the Mooney-Rivlin material. A detailed investigation of the disk MP is presented in Section 4.4.

Remark 2 (Linearly elastic disk BVP). We can follow a similar procedure to define a problem in the context of the classical linear elasticity theory which is analogous to the disk BVP introduced above. We refer to this analogous problem as the *linearly elastic disk BVP*. It consists of finding $r : [R_i, R_e] \to \mathbb{R}$ that satisfies the ordinary differential equation

$$\frac{\mathrm{d}}{\mathrm{d}R}\left[R\,\sigma_{rr}(R)\right] - \sigma_{\theta\theta}(R) = 0\,, \tag{4.13}$$

where σ_{rr} and $\sigma_{\theta\theta}$ are the corresponding components of the stress tensor of the linear theory. To obtain these components, observe from (4.3) that both ν and τ are close to unity near the reference configuration. It then follow from (4.6) and (4.7) that

$$\sigma_{rr}(R) = \hat{\sigma}_{rr}(\nu,\tau) = c_{11}\,(\nu-1) + c_{12}\,(\tau-1)\,, \tag{4.14}$$

$$\sigma_{\theta\theta}(R) = \hat{\sigma}_{\theta\theta}(\nu,\tau) = c_{12}\,(\nu-1) + c_{22}\,(\tau-1)\,. \tag{4.15}$$

In addition, r must also satisfy the boundaries conditions (4.11.a) and

$$\sigma_{rr}(R_e) = -p \tag{4.16}$$

since, in the linear theory, the pressure load is a dead load. The solution of the linearly elastic disk BVP is known and given by, (Aguiar; Fosdick; Sanchez, 2008),

$$\begin{gathered} r(R) = R - \frac{R_i}{2\,\kappa}\left[\left(\frac{R}{R_i}\right)^{\kappa} - \left(\frac{R}{R_i}\right)^{-\kappa}\right]\frac{p}{c_{11}\,p_1}\,, \\ p_1 \triangleq \frac{R_i}{2\,\kappa\,R_e}\left[\left(\kappa - \frac{c_{12}}{c_{11}}\right)\left(\frac{R_i}{R_e}\right)^{\kappa} + \left(\kappa + \frac{c_{12}}{c_{11}}\right)\left(\frac{R_i}{R_e}\right)^{-\kappa}\right], \qquad \kappa \triangleq \sqrt{\frac{c_{22}}{c_{11}}}\,, \end{gathered} \tag{4.17}$$

which, in the case $R_i = 0$, simplifies to

$$r(R) = R - \frac{p\,R_e}{\sqrt{c_{11}\,c_{22}} + c_{12}}\left(\frac{R}{R_e}\right)^{\kappa}. \tag{4.18}$$

4.2 Analysis of the constitutive response of the disk

We apply some concepts presented in Chapter 3 to the considered disk problem. We analyze the response function $\hat{P}_{rr}(\nu,\tau)$, obtain reduced expressions for the continuity conditions (3.87) and (3.88), and obtain reduced expressions for the inequalities (3.92), which are necessary and sufficient conditions for the strong ellipticity condition (3.90).

4.2.1 Behavior of the radial normal stress P_{rr}

Recalling from (4.6)-(4.9) that both $P_{rr}(R) = \hat{P}_{rr}(\nu,\tau)$ and $P_{\theta\theta}(R) = \hat{P}_{\theta\theta}(\nu,\tau)$ and from (4.3) that $\nu = r'$ and $\tau = r/R$, we can use the relations

$$\frac{\mathrm{d}P_{rr}}{\mathrm{d}R} = \frac{\partial \hat{P}_{rr}}{\partial \nu}\,\frac{\partial \nu}{\partial R} + \frac{\partial \hat{P}_{rr}}{\partial \tau}\,\frac{\partial \tau}{\partial R}\,, \qquad \frac{\partial \nu}{\partial R} = r''\,, \tag{4.19}$$

to rewrite (4.10) as a differential equation of the form

$$R\,\frac{\partial \hat{P}_{rr}(r', r/R)}{\partial \nu}\,r'' + f(r', r, R) = 0\,, \tag{4.20}$$

for some function f. Since $R\,\partial \hat{P}_{rr}/\partial \nu$ is the leading term in (4.20), we investigate below the behavior of $\hat{P}_{rr}$.

First we focus on the response of the orthotropic St Venant-Kirchhoff material and, later, on the orthotropic and compressible Mooney-Rivlin material. Observe from (4.6) that $\hat{P}_{rr}$ is a cubic polynomial in ν parameterized by τ and passing through the origin. It may have two or no extrema, depending on the roots of the equation

$$\frac{\partial \hat{P}^{\rm vk}_{rr}}{\partial \nu}(\nu, \tau) = \frac{1}{2}\left[c_{11}\,(3\,\nu^2 - 1) + c_{12}\,(\tau^2 - 1)\right] = 0\,. \tag{4.21}$$

which occur at $\nu = \nu_{e1}$ and $\nu = \nu_{e2}$, where

$$\nu_{e1} = -\nu_{e2} = \frac{\sqrt{3}}{3}\sqrt{(-\tau^2 + \bar{\tau}^2)\,\frac{c_{12}}{c_{11}}}\,, \qquad \bar{\tau} \triangleq \sqrt{\frac{c_{11} + c_{12}}{c_{12}}}\,. \tag{4.22}$$

Clearly, if $|\tau| < \bar{\tau}$, the roots are real numbers and $\hat{P}_{rr}(\nu, \tau)$ has two local extrema given by $P^{\rm min}_{rr} = \hat{P}_{rr}(\nu_e, \tau)$ and $P^{\rm max}_{rr} = \hat{P}_{rr}(-\nu_e, \tau)$, where

$$P^{\rm max}_{rr} = -P^{\rm min}_{rr} = \frac{\sqrt{3}}{9}\sqrt{(-\tau^2 + \bar{\tau}^2)\,\frac{c_{12}}{c_{11}}}\,\left(-\tau^2 + \bar{\tau}^2\right)c_{12}\,. \tag{4.23}$$

On the other hand, if $|\tau| > \bar{\tau}$, the roots are imaginary numbers and $\hat{P}_{rr}(\nu, \tau)$ is a monotonic function of ν for a given τ. In the special case of $|\tau| = \bar{\tau}$, both roots are null. In all the cases, there is an inflection point at the origin, where the graph is concave for $\nu < 0$ and convex, otherwise.

We see from (4.22) that in the case $\tau = 1$, the extrema occur at $\nu = \pm\sqrt{3}/3$ for any value of the elastic constants. Recall from Chapter 2, that this value of stretch was also found by Batra (2001) in the study of homogeneous deformations of a body made of the classical isotropic St Venant-Kirchhoff material. In his work, this value of stretch corresponds to an extremum point in the load-stretch relation of the experiments of simple extension, biaxial loading of a membrane, and triaxial loading of a cube.

In the case of the orthotropic and compressible Mooney-Rivlin material, there may also be extrema, which are determined by finding the roots of the equation

$$2\,\nu^2\,\frac{\partial \hat{P}^{\rm mr}_{rr}}{\partial \nu}(\nu, \tau) = 3\,(c_{11} - c_{33})\,\nu^4 + (\tau^2\,c_{12} - c_{11} - c_{12} + 2\,c_{33})\,\nu^2 + c_{33} = 0\,. \tag{4.24}$$

For $\nu > 0$, the extrema occur at $\nu = \nu_{e1}$ and $\nu = \nu_{e2}$, where

$$\nu_{e1} = \sqrt{\frac{-\bar{b} + \sqrt{\bar{b}^2 - 4\,\bar{a}\,\bar{c}}}{2\,\bar{a}}}\,, \qquad \nu_{e2} = \sqrt{\frac{-\bar{b} - \sqrt{\bar{b}^2 - 4\,\bar{a}\,\bar{c}}}{2\,\bar{a}}}\,, \tag{4.25}$$

$$\bar{a} \triangleq 3\,(c_{11} - c_{33})\,, \qquad \bar{b} \triangleq (\tau^2\,c_{12} - c_{11} - c_{12} + 2\,c_{33})\,, \qquad \bar{c} \triangleq c_{33}\,,$$

if $\nu_{e1}, \nu_{e2} \in \mathbb{R}$. Recall from Section 4.1 that we consider $c_{11} > c_{33}$, thus $\bar{a} > 0$ and, for $\nu > 0$, there are two extrema or there is none; it cannot exist only one extremum.

In Figure 4, we plot $\hat{P}_{rr}^{\mathrm{vk}}(\nu, \tau)$, given by (4.6), versus ν in the range $(-1.5, 1.5)$ using different values of τ and the elastic constants

$$c_{11} = \frac{900}{59} \approx 15.2542\,, \quad c_{22} = \frac{239}{177} \approx 1.35028\,, \quad c_{12} = \frac{30}{59} \approx 0.508475\,, \tag{4.26}$$

which, by using (3.49), are obtained from the engineering constants

$$E_1 = 15\,, \qquad E_2 = E_3 = 1\,, \qquad \mathrm{v}_{12} = \mathrm{v}_{13} = 0.25\,, \qquad \mathrm{v}_{23} = 0.5\,. \tag{4.27}$$

These engineering constants can be used to approximately represent the properties of a unidirectional carbon/epoxy composite (Daniel; Ishai, 2006). Of course, negative values of ν have no physical meaning, and are included here because of the constitutive structure of the hyperelastic model. In Chapter 5 we impose the constraint $\det \mathbf{F} \geq \varepsilon > 0$ and eliminate these negative values from occurring.

We see from Figure 4 that the curve corresponding to $\tau = 6$ is monotonic and the other curves are not monotonic with respect to ν. The non-monotonic curves have two local extrema, which are determined from (4.22) and (4.23), where $\bar{\tau} = 5.568$. All the curves have an inflection point at $\nu = 0$. These results are expected from the previous analysis. We also see from Figure 4 that the curves corresponding to $\tau = 0$ and $\tau = 1$ are very close to each other, which is relevant in the analysis of the disk problem since, in this case, we expect that $0 < \tau \leq 1$.

In Figure 5, we plot $\hat{P}_{rr}^{\mathrm{mr}}(\nu, \tau)$, given by (4.6), versus ν using $c_{33} = c_{22}/d$, $d = 1, 2, 5, 20$, and the elastic constants given by (4.26). We have verified that the curves do not change significantly for $\tau \in (0, 1)$, so we consider $\tau = 1$. We see from this figure that only in the case $c_{33} = c_{22}$ the curve is monotonic. In the other cases, the curves are non-monotonic with extrema at ν_{e1} and ν_{e2} given by (4.25). In addition, in all cases, $P_{rr} \to -\infty$ as $\nu \to 0^+$, which is a physically expected response. Only the interval $\nu > 0$ is physically meaningful and it yields the whole range of $\hat{P}_{rr}^{\mathrm{mr}}$. Nevertheless, we show $\hat{P}_{rr}^{\mathrm{mr}}$ for $\nu < 0$ because, later in Sections 4.3 and 4.4, the numerical procedures we use to solve the disk BVP and MP, respectively, need to prevent $\nu < 0$, even though it is mathematically possible.

We have seen from above that the response functions $\hat{P}_{rr}^{\mathrm{vk}}(\nu, \tau)$ and $\hat{P}_{rr}^{\mathrm{mr}}(\nu, \tau)$, given by (4.6) and (4.8), respectively, may be monotonic or not. In the latter case, they are similar to the non-monotonic response functions used by Ericksen (1975), Abeyaratne (1981), and Fosdick and Macsithigh (1986) in the sense that, as ν increases, $\hat{P}_{rr}(\nu, \tau)$ increases, then it decreases, and then it increases again. In their work, this type of response function yields a deformation field with a jump in its gradient on an internal surface of the body if the applied load is greater than a certain value. We will see in Section 4.3 that the

Figure 4 – Radial normal stress $\hat{P}_{rr}^{\mathrm{vk}}$ versus ν for different values of τ.

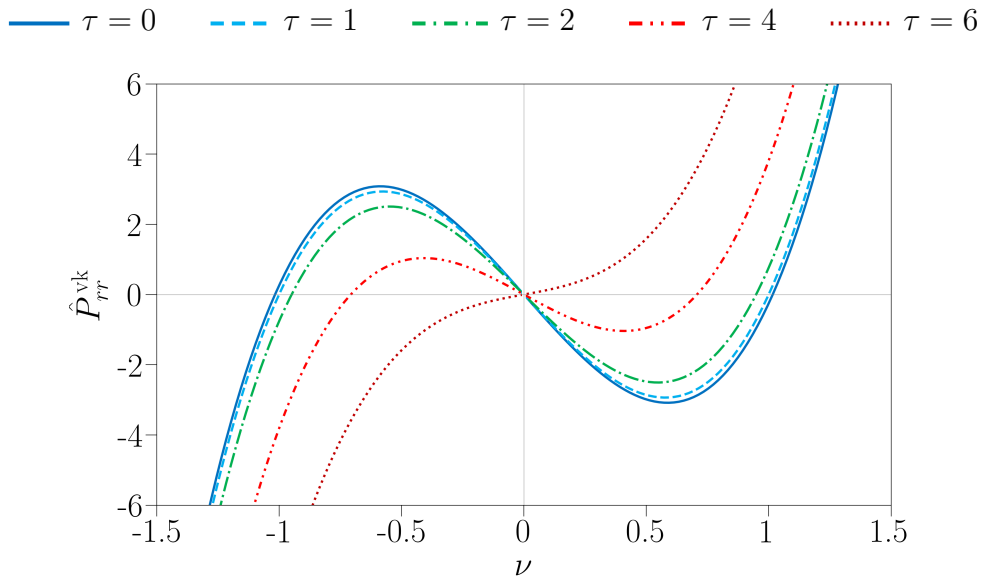

Source: The author.

Figure 5 – Radial normal stress $\hat{P}_{rr}^{\mathrm{mr}}$ versus ν for $\tau = 1$ and different values of c_{33}.

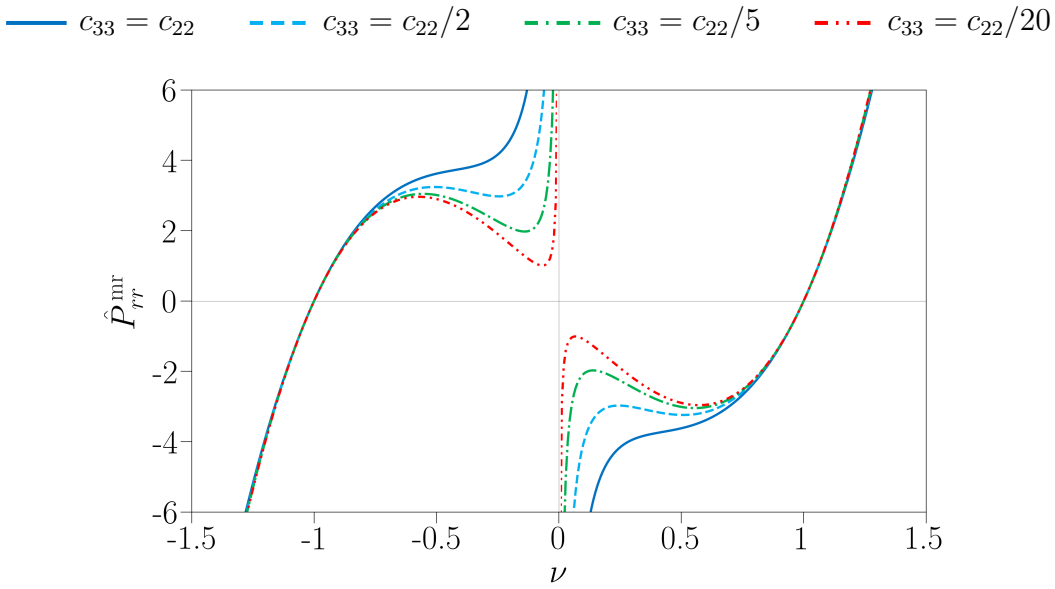

Source: The author.

deformation field of our disk problem has this same behavior. For this reason, we study next some aspects of this non-smooth behavior by applying the continuity conditions (3.87) and (3.88) to the disk problem.

4.2.2 Continuity conditions

We have seen in Section 3.4 that necessary conditions for a non-smooth deformation field $\mathbf{f}$ to minimize the total potential energy (3.71.b) are given by (3.83), (3.87), and (3.88). In this section, we particularize the traction continuity condition (3.87) and the dissipation-free condition (3.88) to the case of the disk BVP.

Since $\mathbf{f}$ is continuous and given by (4.1), both r and $\tau = r/R$ are also continuous and $\mathcal{S}$ is a cylindrical surface with outer unit normal $\mathbf{N} = \mathbf{e}_R$. This together with (4.3) implies that the jump condition on $\mathbf{F}$ is given by

$$[\mathbf{F}]_-^+ = (\nu^+ - \nu^-)\, \mathbf{e}_r \otimes \mathbf{e}_R\,, \tag{4.28}$$

which is in agreement with (3.74). Then, it follows from (4.5) and (3.87) with $\mathbf{N} = \mathbf{e}_R$, that $[P_{rr}\, \mathbf{e}_r]_-^+ = \mathbf{0}$, that is, P_{rr} must be continuous across $\mathcal{S}$. Thus, we find that ν^+ and ν^- must satisfy

$$\hat{P}_{rr}(\nu^+, \tau) = \hat{P}_{rr}(\nu^-, \tau) \triangleq \bar{P}_{rr} \qquad \text{on } \mathcal{S}\,, \tag{4.29}$$

where $\hat{P}_{rr}$ is used to represent both $\hat{P}_{rr}^{\mathrm{vk}}$ and $\hat{P}_{rr}^{\mathrm{mr}}$. This is trivially satisfied if $\nu^+ = \nu^-$, which, as can be seen from (4.28), corresponds to the case of $\mathbf{F}$ being continuous on $\mathcal{S}$. In this case, the dissipation-free condition (3.88) is also trivially satisfied. In the remainder of this section, we assume that $\nu^+ \neq \nu^-$.

Next, we consider the dissipation-free condition (3.88). Since $\mathbf{F}$ has the form (4.3), we write $W(\mathbf{F}) = \hat{W}(\nu, \tau)$. It follows from (4.3.a), (4.5), and (4.29), that the dissipation-free condition (3.88) can be written as

$$\hat{W}(\nu^+, \tau) - \hat{W}(\nu^-, \tau) - (\nu^+ - \nu^-)\, \bar{P}_{rr} = 0 \qquad \text{on } \mathcal{S}\,. \tag{4.30}$$

For a given τ, the equation (4.30) is analogous to equation (3.3) of Ericksen (1975). In view of (3.28), (4.3), and (4.5), we can write $\hat{P}_{rr} = \partial \hat{W}/\partial \nu$. Thus,

$$\hat{W}(\nu^+, \tau) - \hat{W}(\nu^-, \tau) = \int_{\nu_-}^{\nu^+} \hat{P}_{rr}(\nu, \tau)\, \mathrm{d}\nu\,, \tag{4.31}$$

and (4.30) can be rewritten as

$$\int_{\nu_-}^{\nu^+} \hat{P}_{rr}(\nu, \tau)\, \mathrm{d}\nu - (\nu^+ - \nu^-)\, \bar{P}_{rr} = \int_{\nu_-}^{\nu^+} \left[\hat{P}_{rr}(\nu, \tau) - \bar{P}_{rr}\right] \mathrm{d}\nu = 0 \qquad \text{on } \mathcal{S}\,, \tag{4.32}$$

which means that the signed area enclosed by the curve $\hat{P}_{rr}(\nu, \tau) - \bar{P}_{rr}$ and the axis ν must be null. Thus, the horizontal line $\hat{P}_{rr}(\cdot, \tau) = \bar{P}_{rr}$ intersects the graph of $\hat{P}_{rr}(\cdot, \tau)$ at

Figure 6 – Graphical interpretation of equation (4.30).

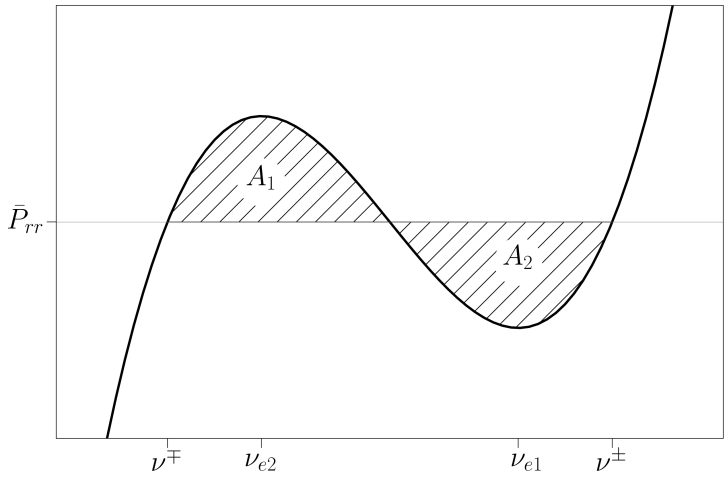

Source: The author.

three points, such that the two enclosed regions between this graph and the horizontal line have equal areas. This situation is depicted in Figure 6, where $\bar{P}_{rr}$ must be chosen so that $A_1 = A_2$.

For the orthotropic St Venant-Kirchhoff material, $\hat{P}_{rr} = \hat{P}_{rr}^{\mathrm{vk}}$, which is given by (4.6), is a cubic polynomial and an odd function in ν; thus, we have that

$$\bar{P}_{rr} = 0\,, \qquad \nu^{+} = -\nu^{-}\,, \qquad |\nu^{+}| = |\nu^{-}| = \sqrt{(-\tau^2 + \bar{\tau}^2)\,\frac{c_{12}}{c_{11}}} \tag{4.33}$$

for $|\tau| < \bar{\tau}$, where $\bar{\tau}$ is given by (4.22.c). In addition, since $\det \mathbf{F}$ is given by (4.4) and τ is continuous on $\mathcal{S}$, $\nu^{+} = -\nu^{-}$ implies that $\det \mathbf{F} \leq 0$ on one of the sides of $\mathcal{S}$. This corresponds to self-intersection, which is a physically unacceptable behavior. For the orthotropic and compressible Mooney-Rivlin material, we could not find a simple expression analogue to (4.33); however, the continuity conditions (4.29) and (4.30) will be verified numerically in Sections 4.3.3 and 4.4.2.

In summary, it follows from the above discussion that (4.29) and (4.30) are necessary conditions for a non-smooth field r with a jump in its first derivative $r' = \nu$ to be a stable solution of the disk BVP, in the sense that it corresponds to a minimum of the total potential energy functional. In the case of the orthotropic St Venant-Kirchhoff material, these conditions can be written as (4.33) and the corresponding stable non-smooth solution predicts self-intersection in a region within the disk, which is not physically admissible.

4.2.3 Strong ellipticity conditions

Let us now study the strong ellipticity conditions (3.92)-(3.93), where $u_1 = \nu(R)$ and $u_2 = \tau(R)$ because of (4.3). In the case of the orthotropic St Venant-Kirchhoff material,

where $\bar{W}$ is given by (3.56), the conditions (3.92)-(3.93) become

$$
\begin{aligned}
Q_{11}^{\mathrm{vk}} &= \frac{1}{2\,\nu^2}\left[c_{11}\,(3\,\nu^2-1)+c_{12}\,(\tau^2-1)\right] = \frac{1}{\nu^2}\,\frac{\partial \hat{P}_{rr}^{\mathrm{vk}}}{\partial \nu} > 0\,,\\
Q_{22}^{\mathrm{vk}} &= \frac{1}{2\,\tau^2}\left[c_{12}\,(\nu^2-1)+c_{22}\,(3\,\tau^2-1)\right] = \frac{1}{\tau^2}\,\frac{\partial \hat{P}_{\theta\theta}^{\mathrm{vk}}}{\partial \tau} > 0\,,\\
Q_{12}^{\mathrm{vk}} &= \frac{1}{2\,\nu^2}\left[c_{12}\,(\nu^2-1)+c_{22}\,(\tau^2-1)\right] + c_{66} > 0\,,\\
Q_{21}^{\mathrm{vk}} &= \frac{1}{2\,\tau^2}\left[c_{11}\,(\nu^2-1)+c_{12}\,(\tau^2-1)\right] + c_{66} > 0\,,\\
Q_{*}^{\mathrm{vk}} &= \sqrt{Q_{11}^{\mathrm{vk}}\,Q_{22}^{\mathrm{vk}}} + \sqrt{Q_{12}^{\mathrm{vk}}\,Q_{21}^{\mathrm{vk}}} - |c_{12}+c_{66}| > 0\,.
\end{aligned}
\tag{4.34}
$$

In the case of the orthotropic and compressible Mooney-Rivlin material, $\bar{W}$ is given by (3.67) and the conditions (3.92)-(3.93) become

$$
\begin{aligned}
Q_{11}^{\mathrm{mr}} &= Q_{11}^{\mathrm{vk}} + \frac{c_{33}}{2\,\nu^4}\,(-3\,\nu^4+2\,\nu^2+1) = \frac{1}{\nu^2}\,\frac{\partial \hat{P}_{rr}^{\mathrm{mr}}}{\partial \nu} > 0\,,\\
Q_{22}^{\mathrm{mr}} &= Q_{22}^{\mathrm{vk}} + \frac{c_{33}}{2\,\tau^4}\,(-3\,\tau^4+2\,\tau^2+1) = \frac{1}{\tau^2}\,\frac{\partial \hat{P}_{\theta\theta}^{\mathrm{mr}}}{\partial \tau} > 0\,,\\
Q_{12}^{\mathrm{mr}} &= Q_{12}^{\mathrm{vk}} + \frac{c_{33}}{2\,\nu^2}\,(2-\nu^2-\tau^2) > 0\,,\\
Q_{21}^{\mathrm{mr}} &= Q_{21}^{\mathrm{vk}} + \frac{c_{33}}{2\,\nu^2}\,(2-\nu^2-\tau^2) > 0\,,\\
Q_{*}^{\mathrm{mr}} &= \sqrt{Q_{11}^{\mathrm{mr}}\,Q_{22}^{\mathrm{mr}}} + \sqrt{Q_{12}^{\mathrm{mr}}\,Q_{21}^{\mathrm{mr}}} - \left|c_{12}+c_{66}+\frac{c_{33}}{2}\left(\frac{1}{\nu^2\,\tau^2}-1\right)\right| > 0\,.
\end{aligned}
\tag{4.35}
$$

The loss of ellipticity occurs when at least one of the above expressions in (4.34)-(4.35) is null. Note from (4.34.a-d) that, if all elastic constants are positive[1], Q_{11}^{vk}, Q_{22}^{vk}, Q_{12}^{vk}, and Q_{21}^{vk} are positive for any $\nu,\tau > 1$; they may be negative only if $\nu,\tau \in (0,1)$. We see from (4.35) that the expressions of Q_{ij}^{mr}, $ij = 11, 22, 12, 22$, are those of the St Venant-Kirchhoff material plus extra terms that multiply c_{33}; similarly to what we have discussed for the stress below (4.8)-(4.9). These extra terms are positive for $\nu,\tau \in (0,1)$ and go to infinity as $\nu,\tau \to 0$; therefore, they contribute to the ellipticity of the governing equations. If $\nu,\tau > 1$, these extra terms are negative, but bounded; on the other hand, Q_{11}^{vk}, Q_{22}^{vk}, Q_{12}^{vk}, and Q_{21}^{vk} are positive and unbounded.

4.3 The disk boundary value problem

In this section, we study the solutions of the disk BVP using a phase-plane technique; see, for instance, Pontryagin (1962). We begin by rewriting the differential equation (3.69)

[1] Recall from (3.94) that this is a requirement for c_{11}, c_{22}, c_{66}, so that the strong ellipticity condition holds at the reference configuration. This ellipticity condition allows $c_{12} < 0$; however, c_{12} is positive for most materials.

as a system of autonomous differential equations[2]. We then use the constitutive relations to construct trajectories of this system.

4.3.1 The autonomous system of differential equations

For a given τ, we solve $P_{rr} = \hat{P}_{rr}(\nu, \tau)$ for ν, yielding $\nu = \check{\nu}(\tau, P_{rr})$. The possible multivaluedness of ν is addressed in Sections 4.3.2 and 4.3.3. We then define $\check{P}_{\theta\theta}(\tau, P_{rr}) \triangleq \hat{P}_{\theta\theta}(\check{\nu}(\tau, P_{rr}), \tau)$ and rewrite the differential equation (3.69) as the system of equations

$$\begin{aligned} \frac{\mathrm{d}}{\mathrm{d}R}[R\,\tau] &= \check{\nu}(\tau, P_{rr})\,, \\ \frac{\mathrm{d}}{\mathrm{d}R}[R\,P_{rr}(R)] &= \check{P}_{\theta\theta}(\tau, P_{rr})\,. \end{aligned} \tag{4.36}$$

Next, we change variables by introducing $\xi = \log R$, $\xi \in [\log R_i, \log R_e]$, and rewrite $\tau(R)$ as $\tau(\xi)$ and $P_{rr}(R)$ as $P_{rr}(\xi)$. The system of equations (4.36) can then be rewritten as the system of autonomous differential equations given by

$$\begin{aligned} \frac{\mathrm{d}\tau}{\mathrm{d}\xi} &= \check{\nu}(\tau, P_{rr}) - \tau\,, \\ \frac{\mathrm{d}P_{rr}}{\mathrm{d}\xi} &= \check{P}_{\theta\theta}(\tau, P_{rr}) - P_{rr}\,, \end{aligned} \tag{4.37}$$

where we have omitted the dependence of both τ and P_{rr} on ξ. Singular points of the system (4.37) are points where both the vertical isocline $\mathcal{V} \triangleq \{(\tau, P_{rr}) \in \mathcal{U} \mid d\tau/d\xi = 0 \overset{(4.37.a)}{\iff} \check{\nu}(\tau, P_{rr}) = \tau\}$ and the horizontal isocline $\mathcal{H} \triangleq \{(\tau, P_{rr}) \in \mathcal{U} \mid dP_{rr}/d\xi = 0 \overset{(4.37.b)}{\iff} \check{P}_{\theta\theta}(\tau, P_{rr}) = P_{rr}\}$ intersect. Therefore, at singular points the relation $\hat{P}_{\theta\theta}(\tau, \tau) = \hat{P}_{rr}(\tau, \tau)$ holds.

Next, we rewrite the boundary conditions (4.11) in terms of τ and P_{rr} as

$$\begin{cases} \tau(\xi) = 1\,, \quad \xi = \log R_i\,, & \text{if } R_i > 0\,, \\ \lim\limits_{\xi \to -\infty} e^{\xi}\,\tau(\xi) = 0\,, & \text{if } R_i = 0\,, \end{cases} \tag{4.38}$$

$$P_{rr}(\xi) = -p\,\tau(\xi)\,, \qquad \xi = \log R_e\,. \tag{4.39}$$

We then use (4.38.a) and (4.39) to define the *initial curve* $\mathcal{C}_i$ and the *terminal curve* $\mathcal{C}_e \equiv \mathcal{C}_e(p)$ as, respectively,

$$\mathcal{C}_i = \{(\tau, P_{rr}) \in \mathcal{U} \mid \tau = 1\}, \qquad \mathcal{C}_e(p) = \{(\tau, P_{rr}) \in \mathcal{U} \mid P_{rr} = -p\,\tau\}\,. \tag{4.40}$$

A *trajectory* of the system (4.37) is a curve in the plane $\mathcal{U} \triangleq \{(\tau, P_{rr}) \mid \tau,\, P_{rr} \in \mathbb{R}\}$ parameterized by ξ that satisfies (4.37) and is oriented according to increasing values of

[2] A system of autonomous differential equation is a system of differential equations that does not explicitly depend on the independent variable.

ξ. The *trajectory of solution* of the disk BVP is a segment of a trajectory of the system (4.37) whose starting and ending points satisfy (4.38) and (4.39), respectively. Therefore, it begins at the initial curve $\mathcal{C}_i$ with $\xi = \log R_i$ for $R_i > 0$ and it ends at the terminal curve $\mathcal{C}_e$ with $\xi = \log R_e$. For $R_i = 0$, the initial point of the trajectory of solution, which corresponds to $\xi = -\infty$, must be a point such that (4.38.b) holds, which can be either a point at infinity or a singular point; for the former, $\tau(\xi)$ may become unbounded as $\xi \to -\infty$ as long as e^{ξ} tends to zero at a faster enough rate, for the latter, $\tau(\xi)$ remains finite so (4.38.b) is trivially verified.

To construct the *phase portrait* of the autonomous system (4.37), which is a collection of trajectories of this system, we must determine expressions for $\check{\nu}(\tau, P_{rr})$ and $\check{P}_{\theta\theta}(\tau, P_{rr})$, which depends on the constitutive relation.

4.3.2 Orthotropic St Venant-Kirchhoff material

In the case of the orthotropic St Venant-Kirchhoff material, it follows from (4.6) that $\nu = \check{\nu}(\tau, P_{rr})$ satisfies the cubic equation

$$\nu^3 - \left[1 + \frac{c_{12}}{c_{11}}\,(1 - \tau^2)\right]\nu - 2\,\frac{P_{rr}}{c_{11}} = 0. \tag{4.41}$$

The discriminant of this equation is given by

$$D = D(\tau, P_{rr}) \triangleq -4\,a^3 - 27\,b^2\,, \tag{4.42}$$

where $a \triangleq -[1 + (1 - \tau^2)\,c_{12}/c_{11}]$ and $b \triangleq -2\,P_{rr}\,/c_{11}$, where we recall from (3.94.a) that $c_{11} > 0$. We then have the following three cases of interest, which will be used in the discussion of numerical results presented below.

- If $D = 0$, the equation (4.41) has either a triple root $\nu_3^0 = 0$ if $a = b = 0$ or both a simple root $\nu_1^0 = 3\,b/a$ and a double root $\nu_2^0 = -\nu_1^0/2$ if $a \neq 0$ and $b \neq 0$. In the latter case, $D = 0$ and $-27\,b^2 < 0$ yields $a < 0$; thus, for $c_{11} > 0$, ν_1^0 has the same sign of P_{rr} and ν_2^0 the opposite sign.

- If $D > 0$, the equation (4.41) has three distinct real roots, given by $\nu_i = \nu_i(\tau, P_{rr})$, $i = 1, 2, 3$, where $\nu_1 < \nu_2 < \nu_3$. By Vieta's formulas, $\nu_1 + \nu_2 + \nu_3 = 0$ and $\nu_1\,\nu_2\,\nu_3 = 2\,P_{rr}/c_{11}$. Therefore, $\nu_1 < 0$, $\nu_3 > 0$, and, since $c_{11} > 0$, ν_2 has the opposite sign of P_{rr}. In addition, for $D \to 0^+$, we have: (i) $\nu_1, \nu_2 \to \nu_2^0$ and $\nu_3 \to \nu_1^0$ if $P_{rr} > 0$; (ii) $\nu_2, \nu_3 \to \nu_2^0$ and $\nu_1 \to \nu_1^0$ if $P_{rr} < 0$; (iii) $\nu_1, \nu_2, \nu_3 \to 0$ if $P_{rr} = 0$.

- If $D < 0$, the equation (4.41) has only one real root $\nu_* = \nu_*(\tau, P_{rr})$ and two complex conjugate roots. Again, by Vieta's formulas, the product of these three roots is equal to $2\,P_{rr}/c_{11}$. Therefore, ν_* has the same sign of P_{rr} since the product between two complex conjugates is positive. In addition, $\nu_* \to \nu_1^0$ for $D \to 0^-$.

We use the discriminant D to define the regions

$$\mathcal{D}_{>} \triangleq \{(\tau, P_{rr}) \in \mathcal{U} \mid D > 0\}, \qquad \mathcal{D}_{<} \triangleq \{(\tau, P_{rr}) \in \mathcal{U} \mid D < 0\}. \tag{4.43}$$

The interface between $\mathcal{D}_{>}$ and $\mathcal{D}_{<}$ corresponds to points where $D = 0$. Once $\nu = \check{\nu}(\tau, P_{rr})$ is determined, $\check{P}_{\theta\theta}(\tau, P_{rr})$ is obtained from (4.7) by recalling from above that $\check{P}_{\theta\theta}(\tau, P_{rr}) \triangleq \hat{P}_{\theta\theta}(\check{\nu}(\tau, P_{rr}), \tau)$.

Given p, $R_i \neq 0$, and the elastic constants c_{11}, c_{12}, c_{22}, we can determine trajectories of solutions of the disk BVP by generating a set of points $\{(\tau^j, P_{rr}^j)\}$, $j = 1, 2, ..., N$, where $(\tau^1, P_{rr}^1) \in \mathcal{C}_i$,

$$(\tau^{j+1}, P_{rr}^{j+1}) = (\tau^j, P_{rr}^j) + \delta\xi_j \left(\frac{d\tau}{d\xi}, \frac{dP_{rr}}{d\xi}\right)\Big|_{(\tau^j, P_{rr}^j)}, \tag{4.44}$$

and N is such that $\sum_{j=1}^{N} \delta\xi_j = \Delta\xi \triangleq \log R_e - \log R_i$. Thus, N is the total number of steps that are necessary to go from the initial curve $\mathcal{C}_i$ to the terminal curve $\mathcal{C}_e$. In addition, we use a simple iterative procedure to choose the initial point $(\tau^1, P_{rr}^1) \in \mathcal{C}_i$ in such a way that the last point (τ^N, P_{rr}^N) is close to $\mathcal{C}_e(p)$ within a small error. More precisely, $(\tau^N, P_{rr}^N) \in \mathcal{C}_e(p_*)$, where $|p - p_*| < 0.001\,|p|$. For $R_i = 0$, we consider a sequence of disk BVPs parameterized by the internal radius $R_i > 0$ and obtain the trajectory of solution in the limit, as $R_i \to 0$.

Remark 3 (Trajectories of the linearly elastic case). As mentioned in Section 4.1, in the context of the linear elasticity theory, $P_{rr} = \sigma_{rr}$ is given by (4.14), from which we obtain $\check{\nu}(\tau, \sigma_{rr}) = 1 + [\sigma_{rr} - c_{12}\,(\tau - 1)]/c_{11}$. Also, $\check{P}_{\theta\theta}(\tau, \sigma_{rr}) = \check{\sigma}_{\theta\theta}(\tau, \sigma_{rr}) \triangleq \hat{\sigma}_{\theta\theta}(\check{\nu}(\tau, \sigma_{rr}), \tau)$ is obtained from (4.15). In the linear theory, the above comments regarding the starting point of the trajectory of solution remain valid. For the ending point, however, (4.39.a) is replaced by $\sigma_{rr}(R_e) = -p$, yielding the terminal curve $\mathcal{C}_e(p) = \{(\tau, \sigma_{rr}) \in \mathcal{U} \,|\, \sigma_{rr} = -p\}$, instead of (4.40.b). The trajectory of solution in the linear case is then obtained from the exact solution of the linearly elastic disk BVP given by (4.17) together with (4.14) and (4.3.b,c).

In the remainder of this section, we use $R_e = 1$, so that all lengths are normalized with respect to R_e, and the elastic constants c_{11}, c_{22}, c_{12} given by (4.26). In Figure 7, we plot phase portraits associated with the system (4.37) together with some auxiliary lines. The gray oriented lines are the trajectories, the black vertical dashed line is the initial curve $\mathcal{C}_i$, and the blue dashed line is the terminal curve $\mathcal{C}_e(p)$ for $p = 0.01$. In addition, the green dashed line segments correspond to $D = 0$, where D is the discriminant defined in (4.42), and separate the regions $\mathcal{D}_{<}$ and $\mathcal{D}_{>}$, which are defined in (4.43). Figures 7.a-c are the phase portraits for the orthotropic St Venant-Kirchhoff material and Figure 7.d is the phase portrait for the linear elastic material. Inside the region $\mathcal{D}_{>}$, recall from below (4.42) that $\check{\nu}(\tau, P_{rr})$ may assume three possible values, denoted by $\nu_i(\tau, P_{rr})$, $i = 1, 2, 3$. Figures 7.a-c are phase portraits corresponding to ν_1, ν_2, and ν_3, respectively. Outside the region

$\mathcal{D}_>$, $\check{\nu}(\tau, P_{rr})$ assumes only one value and, therefore, in Figures 7.a-c, the trajectories differ only inside $\mathcal{D}_>$.

The red line segments shown in Figures 7.a-c are trajectories of solutions of the disk BVP for $R_i = 0.001$ and $p = 0.01$. To obtain these trajectories, we use (4.44) with the steps $\delta\xi_j = \delta\xi = 0.001$ for $j = 1, 2, ..., N-1$, and the last step $\delta\xi_N = -\log R_i - (N-1)\,\delta\xi$. Similarly, the red line segment shown in Figure 7.d is the trajectory of solution of the linearly elastic disk BVP for the same values of R_i and p. As mentioned in Remark 3, we use the exact solution (4.17) to determine this trajectory. In Figure 8, we show enlargements of the phase portraits of Figure 7 near the trajectories of solutions.

Recall from Section 4.3.1 that $\hat{P}_{\theta\theta}(\tau, \tau) = \hat{P}_{rr}(\tau, \tau)$ at singular points. Thus, it follows from (4.6) and (4.7) that $(\tau, P_{rr}) \in \{(-1, 0), (0, 0), (1, 0)\}$ are singular points as can be seen from Figures 8.a-c. Observe from Figures 8.a-b that the red line segments end on $\mathcal{C}_e$ for τ not close to 1, which means that the outer surface of the disk undergoes a large deformation for an applied pressure that is small. This behavior is not physically realistic. On the other hand, the red line segment shown in Figure 8.c ends near $\tau = 1$ and is similar to the trajectory of solution of the linearly elastic disk BVP represented by the red line segment of Figure 8.d. This is consistent with the result that the St Venant Kirchhoff model reduces to the linear elastic model in the limit of infinitesimal deformations.

In view of the exposition above, we restrict our analysis to the case $\check{\nu} = \nu_3$ in $\mathcal{D}_>$. Recall from (4.42) and the ensuing discussion that, along the upper green dashed line, where $D = 0$ and $P_{rr} > 0$, we have $\nu_* = \nu_3 = \nu_1^0$. Along the lower green dashed line, where $D = 0$ and $P_{rr} < 0$, we have $\nu_* = \nu_1 = \nu_1^0$ and $\nu_3 = \nu_2^0$. Therefore, $\check{\nu}$ is continuous along the upper green dashed line and has a finite jump from $\nu_* = \nu_1^0$ to $\nu_3 = \nu_2^0$ along the lower green dashed line. It follows from both (4.37) and (4.7) that a jump in $\check{\nu}$ causes a jump in both $\mathrm{d}\tau/\mathrm{d}\xi$ and $\mathrm{d}P_{rr}/\mathrm{d}\xi$, which results in the abrupt change of direction of the trajectories observed along the lower green dashed line in Figure 7.c.

In Figure 9, we show trajectories of solutions for $R_i = 0.001$ and three different values of pressure, $p = 0.005, 0.013773, 0.02$. The solid lines correspond to trajectories of solutions of the disk BVP by choosing $\check{\nu}(\tau, P_{rr}) = \nu_3(\tau, P_{rr})$ in $\mathcal{D}_>$. The dotted lines correspond to trajectories of solutions of the linearly elastic disk BVP. The black dashed line is the interface between $\mathcal{D}_>$ and $\mathcal{D}_<$. As mentioned below (4.44), the trajectories begin at the initial curve $\mathcal{C}_i$, defined by (4.40.a), and end at the terminal curve $\mathcal{C}_e$, defined by (4.40.b) in the case of the disk BVP and inside Remark 3 in the case of the linearly elastic disk BVP. In view of this, observe from the inset of the figure that the curves end before $(1, 0)$.

We see from this Figure 9 that, for $p = 0.005$, the trajectories of the nonlinear and linear cases are very similar to each other and that, as p increases, the solid and the dotted lines become very different. In particular, for $p = 0.02$, the trajectory of the nonlinear

Figure 7 – Phase portraits of the system (4.37): (a), (b), (c) Orthotropic St Venant-Kirchhoff material. (d) Linear elastic material.

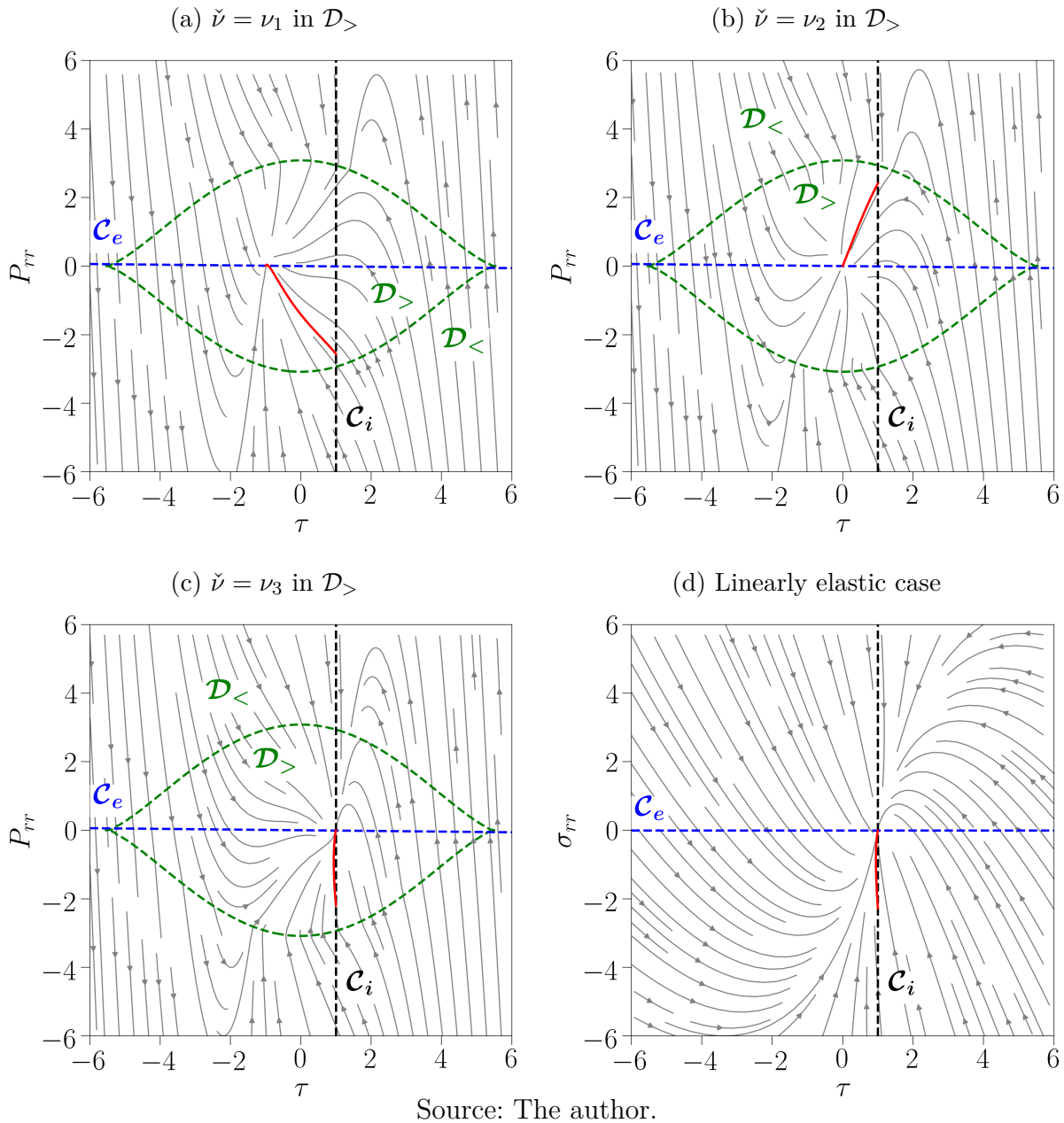

Source: The author.

Figure 8 – Enlargements of the phase portraits of Figure 7. (a), (b), (c) Orthotropic St Venant-Kirchhoff material. (d) Linear elastic material.

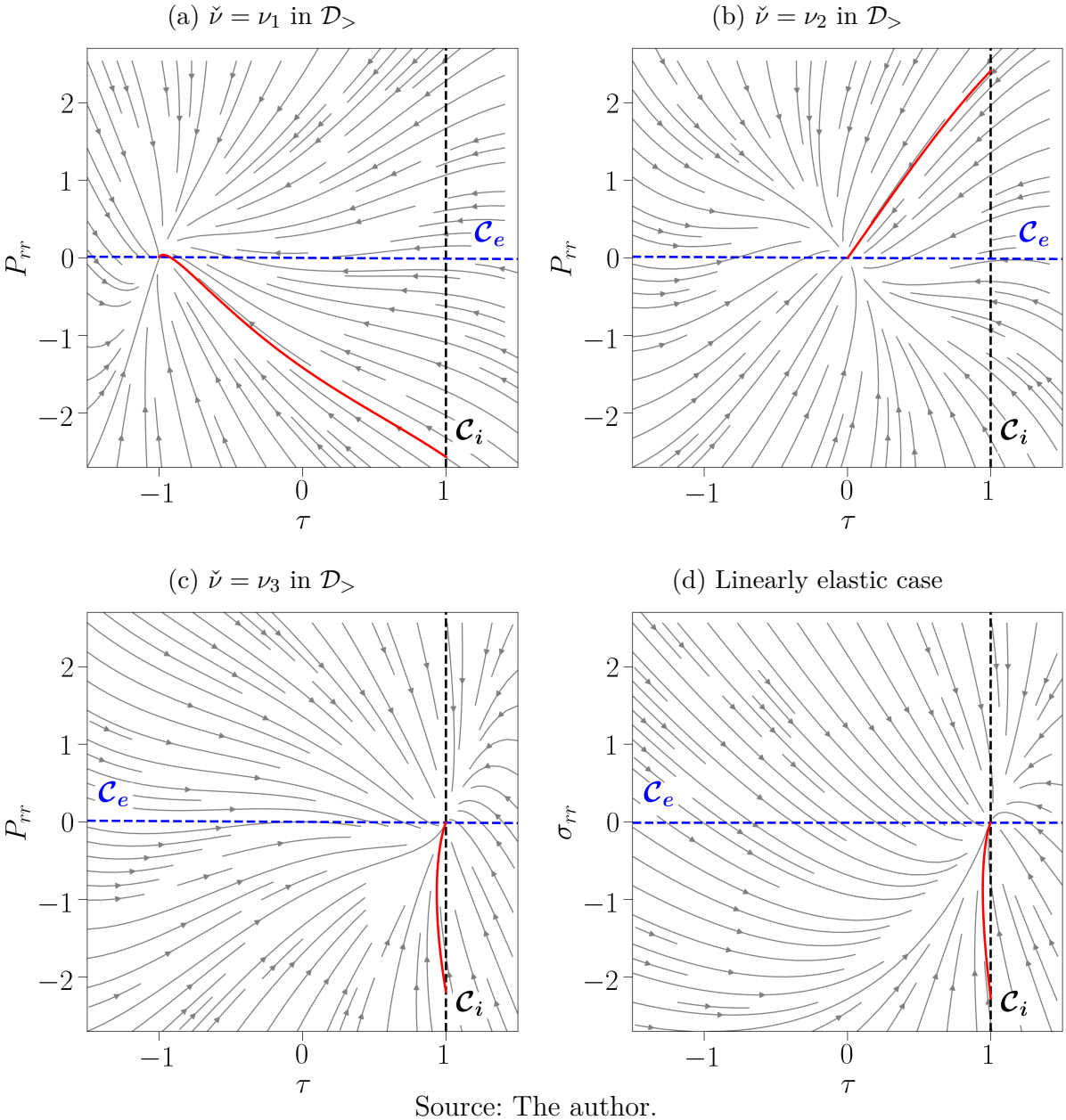

Source: The author.

Figure 9 – Trajectories of solutions of the disk BVP for the St Venant-Kirchhoff material (solid lines) and their linearly elastic counterparts (dotted lines) for $R_i = 0.001$ and different values of p.

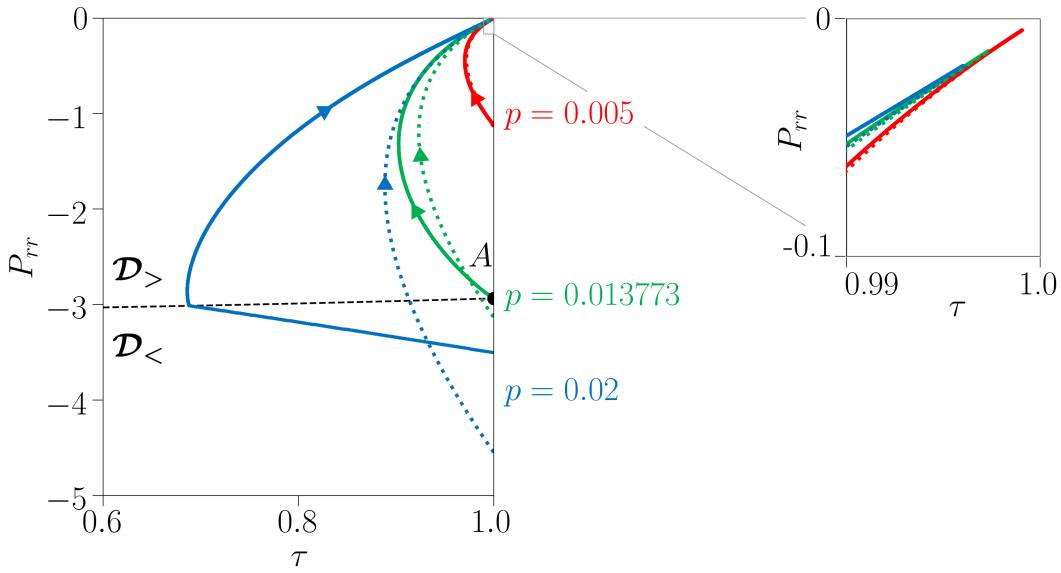

Source: The author.

case is not smooth at the interface between $\mathcal{D}_>$ and $\mathcal{D}_<$. As mentioned above, this is because the corresponding field $\check{\nu}$ has a jump discontinuity at this interface. Therefore, this non-smooth trajectory corresponds to a field r that has a finite jump in its derivative r', where we recall from above that $r'(R) = \nu(R) = \check{\nu}(\tau, P_{rr})$, at an interior point of the disk. It also provides an example of solution of the disk BVP that does not correspond to a minimum of the energy functional, even though it is part of a sequence of solutions that approach their linear counterpart as p decreases. To see this, observe from Figure 9 that, for $p = 0.02$, the trajectory of solution is not smooth at a point where $P_{rr} \approx -3$, which does not satisfy the relations (4.29) and (4.33.a). In addition, this non-smooth trajectory corresponds to a solution that predicts self-intersection, which is not physically admissible. To see this, recall from the discussion below (4.42) that, in $\mathcal{D}_<$, $\check{\nu}(\tau, P_{rr}) = \nu^*(\tau, P_{rr})$ is negative if $P_{rr} < 0$. Therefore, from (4.4), we have that $\det \mathbf{F} = \nu\,\tau < 0$ in the segment of trajectory that belongs to $\mathcal{D}_<$.

In Section 4.4.2, we show a deformation field that is not smooth and, yet, corresponds to a minimizer of the energy functional. The phase-plane technique used here can be adapted to obtain a trajectory of solution that is also an energy minimizer. This is done in Section 4.3.3 for the case of the Mooney-Rivlin material.

It follows from the above discussion that the orthotropic St Venant-Kirchhoff material model matches well the response of the corresponding linear elastic material for small values of p and that it is not appropriate to model the behavior of the disk for large

values of p. We infer from the above that there is an intermediate value of p, denoted by $\bar{p}$, above which the solution of the disk BVP has a finite jump discontinuity in its derivative. This value corresponds to the point A in Figure 9, which is at the intersection of the initial curve $\mathcal{C}_i$ with the line defined by $D = 0$ represented by the black dashed line, where D is defined in (4.42). We then have that $D(1, P_{rr}) = 4\,[1 - 27\,(P_{rr}/c_{11})^2] = 0$, yielding the initial point $(\tau^1, P^1_{rr}) = (1, -c_{11}\,\sqrt{3}/9) = (1, -2.93568)$ for the recursive formula (4.44), where c_{11} is given by (4.26.a). The last point (τ^N, P^N_{rr}) of the trajectory yields $\bar{p} = -P^N_{rr}/\tau^N = 0.013773$, which is a value of p shown in Figure 9.

Substituting the pair (τ^1, P^1_{rr}) into (4.6) yields $\nu = \sqrt{3}/3$. Thus, $\bar{p}$ can also be obtained from the solution of the differential equation (4.10), (4.6), and (4.7), with the initial conditions $r(R_i) = R_i$ and $r'(R_i) = \sqrt{3}/3$. Since the solution corresponding to $p = \bar{p}$ is smooth, this initial value problem can be solved numerically using a standard numerical solver of differential equations[3]. Using (4.11), we obtain $\bar{p} = -P_{rr}(R_e)/\tau(R_e)$, where $P_{rr}(R_e)$ is evaluated from (4.6) employing the numerical solution. This numerical approach yields the values of $\bar{p}$ presented in Table 1.

Next, recall from the discussion of Figure 9 that the solution of the disk BVP predicts self-intersection for $p > \bar{p}$. In the context of the linearly elastic BVP, Aguiar, Fosdick and Sanchez (2008) determined an analogous upper bound $\bar{p}_{\text{lin}}$, that is, the solution of the linearly elastic BVP predicts self-intersection for $p > \bar{p}_{\text{lin}}$. This critical value is given by $\bar{p}_{\text{lin}} = c_{11}\,p_1$, where p_1 is given by (4.17.b,c).

In Table 1, we show $\bar{p}$, $\bar{p}_{\text{lin}}$, and the ratio $\bar{p}_{\text{lin}}/\bar{p}$ for different values of R_i. The numbers inside parenthesis are the ratios between two consecutive values of either $\bar{p}$ or $\bar{p}_{\text{lin}}$ evaluated at $10\,R_i$ and R_i. We see from this table that, as $R_i \to 0$, both $\bar{p}$ and $\bar{p}_{\text{lin}}$ tend to zero at the same ratio, which is, approximately, equal to 5.04. Therefore, if the disk is solid, in which case $R_i = 0$, the deformation field has a finite jump in its spatial derivative and predicts self-intersection for any value of $p > 0$. We do not treat the case $R_i = 0$ directly because, in this case, $\Delta\xi = \infty$ and we cannot use (4.44) to obtain trajectories of solutions. For all the considered values of R_i, we have that $\bar{p} < \bar{p}_{\text{lin}}$ and, for $R_i < 10^{-3}$, the ratio $\bar{p}_{\text{lin}}/\bar{p}$ is approximately constant and equal to 4.85, yielding $\bar{p} \approx 0.206\,\bar{p}_{\text{lin}}$.

Although not shown here, we also calculated the ratio $\bar{p}_{\text{lin}}/\bar{p}$ for $R_e = 1$, $c_{22} = 1$, and different combinations of $R_i \in [10^{-8}, 0.9]$, $c_{11} \in (1, 10^4]$, and $c_{12} \in [0, 1]$. In all the cases, we have obtained $\bar{p}_{\text{lin}}/\bar{p} \in [3.6, 5.2]$, which means that the critical pressure, $\bar{p}$, above which self-intersection occurs by using the St Venant-Kirchhoff material is lower than the corresponding critical pressure, $\bar{p}_{\text{lin}}$, predicted by the classical linear theory. Therefore, $\bar{p}$ yields an upper bound of p below which the classical linear elasticity theory is valid.

[3] We use the routine *solve_ivp* of the the Python library SciPy, version 1.4.1, with the parameters $atol = rtol = 10^{-10}$. To avoid numerical singularity, we use the initial condition $r'(R_i) = \sqrt{3}/3 + 10^{-8}$.

Table 1 – Comparison between $\bar{p}$ and $\bar{p}_{\text{lin}}$ for different values of R_i.

R_i	10^{-1}	10^{-2}	10^{-3}	10^{-4}	10^{-5}	10^{-6}	10^{-7}	10^{-8}
$\bar{p}$	4.25e-01	7.19e-02	1.38e-02	2.71e-03	5.38e-04	1.07e-04	2.11e-05	4.20e-06
		(5.91)	(5.22)	(5.08)	(5.05)	(5.04)	(5.04)	(5.04)
$\bar{p}_{\text{lin}}$	2.02	3.51e-01	6.71e-02	1.32e-02	2.61e-03	5.17e-04	1.03e-04	2.04e-05
		(5.77)	(5.23)	(5.09)	(5.05)	(5.04)	(5.04)	(5.04)
$\bar{p}_{\text{lin}}/\bar{p}$	4.767	4.882	4.871	4.857	4.852	4.850	4.850	4.850

4.3.3 Orthotropic and compressible Mooney-Rivlin material

We have seen in Section 4.3.1 that to determine the trajectories associated with the autonomous system of differential equations (4.37), we need to determine $\check{\nu}(\tau, P_{rr})$ and $\check{P}_{\theta\theta}(\tau, P_{rr})$, which depend on the constitutive relation. In the case of the orthotropic and compressible Mooney-Rivlin material, $\check{\nu}(\tau, P_{rr})$ is obtained numerically from the relation $P_{rr} = \hat{P}_{rr}^{\text{mr}}(\check{\nu}, \tau)$, where $\hat{P}_{rr}^{\text{mr}}$ is given by (4.8), and $\check{P}_{\theta\theta}(\tau, P_{rr})$ is obtained from its definition below (4.36) as $\check{P}_{\theta\theta}(\tau, P_{rr}) = \hat{P}_{\theta\theta}^{\text{mr}}(\check{\nu}(\tau, P_{rr}), \tau)$, where $\hat{P}_{\theta\theta}^{\text{mr}}$ is given by (4.9).

In addition, we use (4.30) to define the curve

$$\mathcal{C}_{\mathcal{S}} = \{(\tau, P_{rr}) \in \mathcal{U} \mid [\hat{W}(\check{\nu}, \tau) + \check{\nu}\, P_{rr}]_{-}^{+} = 0\,,\ \check{\nu} = \check{\nu}(\tau, P_{rr})\}\,. \tag{4.45}$$

This curve represents the points that satisfy (4.30) and, thus, any jump in ν must occur at a point of this curve for the trajectory of solution be a minimizer of the energy. As we have seen in Section 4.2.1, $\hat{P}_{rr}^{\text{mr}}$ may be non-monotonic with respect to ν depending on the elastic constants, so we expect a jump discontinuity in ν.

Differently from Section 4.3.2, here, it is more convenient to construct trajectories of solutions from the outer radius to the inner radius of the disk. This is because near the inner radius, P_{rr} may have a large absolute value and, as we have seen in Figure 5, the relation between (τ, P_{rr}) and $\nu > 0$ may be not one-to-one, so it is not immediately clear which value of ν to choose. On the other hand, at the outer radius, P_{rr} has a low absolute value for plausible values of p. In this case, $(\tau, P_{rr}) \mapsto \nu$ is one-to-one and $\nu \approx 1$, so ν is determined unequivocally. As we construct the trajectory, ν remains well defined even if $(\tau, P_{rr}) \mapsto \nu$ is not one-to-one because ν is continuous except at a point of the curve $\mathcal{C}_{\mathcal{S}}$, where ν jumps to it lowest positive value. More specifically, recall from Section 4.2.1 that $\hat{P}_{rr}^{\text{mr}}$ may have two extrema, so the map $(\tau, P_{rr}) \mapsto \nu$ may yield $\nu = \nu_i$, $i = 1, 2, 3$, where $0 < \nu_1 < \nu_2 < \nu_3$; in this case, a jump between ν_1 and ν_3 occurs across the curve $\mathcal{C}_{\mathcal{S}}$.

Therefore, we generate the set of points $\{(\tau^j, P_{rr}^{a\,j})\}$, $j = 1, 2, ..., N$, using the recursive formula

$$(\tau^{j+1}, P_{rr}^{j+1}) = (\tau^j, P_{rr}^j) - \delta\xi_j \left(\frac{d\tau}{d\xi}, \frac{dP_{rr}}{d\xi}\right)\Big|_{(\tau^j, P_{rr}^j)}\,, \tag{4.46}$$

Figure 10 – Trajectories of solutions of the disk BVP for the Mooney-Rivlin material (solid lines) and their linearly elastic counterparts (dotted lines) for $R_i = 0.001$ and different values of p.

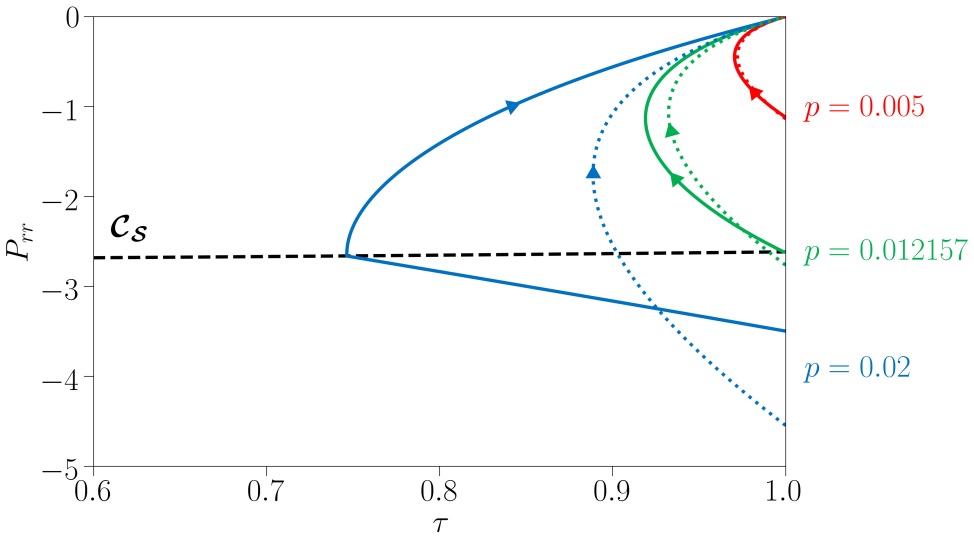

Source: The author.

where $(\tau^1, P_{rr}^1) \in \mathcal{C}_e$ and N is such that $\sum_{j=1}^{N} \delta\xi_j = \Delta\xi \triangleq \log R_e - \log R_i$. Thus, N is the number of steps to go from the terminal curve $\mathcal{C}_e$ to the initial curve $\mathcal{C}_i$ and is a consequence of the choice for the size steps $\delta\xi_j$. We use a simple iterative procedure to find the initial point $(\tau^1, P_{rr}^1) \in \mathcal{C}_e$ such that $0.999 < \tau^N < 1.001$, that is, the last point (τ^N, P_{rr}^N) is close enough to $\mathcal{C}_i$.

In Figure 10, we show trajectories of solutions for $R_i = 0.001$ and three different values of pressure, $p = 0.005, 0.012157, 0.02$. We use the same elastic constants of Section 4.3.2, which are given by (4.26), in addition to $c_{33} = c_{22}/5$. The solid lines correspond to trajectories of solutions of the disk BVP and the dotted lines correspond to trajectories of solutions of the linearly elastic disk BVP. The black dashed line represents the curve $\mathcal{C}_{\mathcal{S}}$ given by (4.45). Similarly to the St Venant-Kirchhoff case presented in Figure 9, the trajectories of the nonlinear and linear cases are very similar to each other for $p = 0.005$ and they become very different from each other as p increases. In addition, note that the critical pressure above which the solution becomes non-smooth is $p = 0.012157$, which is a lower value than that of the St Venant-Kirchhoff material shown in Figure 9. For $p = 0.02$, the trajectory of the nonlinear case is non-smooth at the $\mathcal{C}_{\mathcal{S}}$, which means that the dissipation-free condition (4.30) holds. Recall from Section 4.2.2 that this condition together with the traction continuity condition (4.29) are necessary conditions that a minimizer of the energy functional must satisfy. The traction continuity condition (4.29) is also verified since the trajectory is continuous. Therefore, both necessary conditions are satisfied.

4.4 The disk minimization problem

We now turn our attention to the disk minimization problem (*disk MP*) defined in (4.12) and present a numerical method to find approximate solutions of this problem. The numerical method is implemented in a C++ code using the open-source finite element library deal.ii (Arndt *et al.*, 2019).

4.4.1 Numerical procedure

The numerical procedure is based in a finite element formulation of the disk MP. For this, let $\mathcal{V}_h$ be a finite dimensional space spanned by a set of scalar basis functions $\{w_i\}$, where h stands for the characteristic length of the finite element. Then, an approximate minimizer $\mathbf{u}_h$ of the disk MP can be written as

$$\mathbf{u}_h = u_h\,\mathbf{e}_R\,, \qquad u_h = \sum_{i=1}^{m} s_i\,w_i\,, \tag{4.47}$$

where $u_h \in \mathcal{V}_h$ is the approximate radial displacement, $s_i \in \mathbb{R}$, $i = 1, 2, 3, ..., m$, is a degree of freedom and m is the number of degrees of freedom associated with the discretization. In this work, we use Lagrange finite elements with degree $d = 1, 2, 3, ...$ and a Gauss-Legendre quadrature rule with $2\,d$ points.

For the orthotropic St Venant-Kirchhoff material, we use (4.12), (3.97), (3.46), (3.14), (4.2), $B(\mathbf{f}) = 0$, and $u_r(R_i) = 0$ to obtain $\check{\mathcal{E}}(u_r) = \check{\mathcal{E}}^{\,\mathrm{vk}}(u_r)$, where

$$\begin{aligned}\check{\mathcal{E}}^{\,\mathrm{vk}}(u_r) \triangleq \pi \int_{R_i}^{R_e} \Big(&\frac{c_{11}}{4}\,R\,u_r'^{\,4} + c_{11}\,R\,u_r'^{\,3} + c_{11}\,R\,u_r'^{\,2} + c_{12}\,u_r\,u_r'^{\,2} + 2\,c_{12}\,u_r\,u_r' \\ &+ \frac{c_{12}}{2\,R}\,u_r^2\,u_r'^{\,2} + \frac{c_{12}}{R}\,u_r^2\,u_r' + \frac{c_{22}}{R}\,u_r^2 + \frac{c_{22}}{R^2}\,u_r^3 + \frac{c_{22}}{4\,R^3}\,u_r^4\Big)\,\mathrm{d}R \\ &+ \pi\,p\,\Big[(R_e + u_r(R_e))^2 - R_i^2\Big]\,.\end{aligned} \tag{4.48}$$

Similarly, for the orthotropic and compressible Mooney-Rivlin material, we use (3.67) in the place of (3.46) to obtain $\check{\mathcal{E}}(u_r) = \check{\mathcal{E}}^{\,\mathrm{mr}}(u_r)$, where

$$\begin{aligned}\check{\mathcal{E}}^{\,\mathrm{mr}}(u_r) \triangleq \check{\mathcal{E}}^{\,\mathrm{vk}}(u_r) + \pi\,c_{33} \int_{R_i}^{R_e} \Bigg\{ &-\frac{R}{4}\Big(u_r'^{\,4} + 4\,u_r'^{\,3} + 2\,u_r'^{\,2} - 4\,u_r'\Big) \\ &- \frac{R}{2}\,\log\left[\frac{(R^2 + 2\,R\,u_r + u_r^2)\,(u_r'^{\,2} + 2\,u_r' + 1)}{R^2}\right] \\ &+ u_r - \frac{u_r^2}{2\,R} - \frac{u_r^3}{R^2} - \frac{u_r^4}{4\,R^3}\Bigg\}\,\mathrm{d}R\,.\end{aligned} \tag{4.49}$$

We have seen in Section 4.3 that the radial stretch ν may be discontinuous. This creates numerical difficulties for standard numerical procedures. In view of this, we propose a numerical procedure that uses a penalty formulation to restrict the jump in ν to occur at a position $R = R_{\mathcal{S}}$ and then search for the value of $R_{\mathcal{S}}$ that minimizes the total potential energy functional. For that, we introduce the penalty functional

$$\mathcal{Q}(u_r, R_{\mathcal{S}}) \triangleq \delta_e \left[\int_{\mathcal{B}_-} \max\left(0, \nu - \nu_{e2}\right)^2 \mathrm{d}\mathbf{x} + \int_{\mathcal{B}_+} \max\left(0, \nu_{e1} - \nu\right)^2 \mathrm{d}\mathbf{x} \right] \geq 0\,, \tag{4.50}$$

where both ν_{e1} and ν_{e2} are given by either (4.22) for the St Venant-Kirchhoff material or (4.25) for the Mooney-Rivlin material, $\delta_e > 0$ is a penalty parameter, and, here, $\mathcal{B}_- \triangleq \{\mathbf{x} \in \mathcal{B} \,|\, R_i < R < R_{\mathcal{S}}\}$ and $\mathcal{B}_+ \triangleq \{\mathbf{x} \in \mathcal{B} \,|\, R_{\mathcal{S}} < R < R_e\}$. We see from (4.50) that $\mathcal{Q}$ is null if and only if $\nu \geq \nu_{e1}$ in $\mathcal{B}_+$ and $\nu \leq \nu_{e2}$ in $\mathcal{B}_-$. In addition, $R_{\mathcal{S}}$ is not limited to be in the interval $[R_i, R_e]$; for instance, $R_{\mathcal{S}} < R_i$ means that $\mathcal{B}_- = \emptyset$, $\mathcal{B}_+ = \mathcal{B}$, and ν is continuous.

We consider the bi-level minimization problem[4]

$$\min_{R_{\mathcal{S}} \in \mathbb{R}} \quad \min_{\mathbf{s} \in \mathbb{R}^m} \mathcal{F}(\mathbf{s}, R_{\mathcal{S}})\,, \qquad \mathcal{F}(\mathbf{s}, R_{\mathcal{S}}) = \mathcal{E}_h(\mathbf{s}) + \mathcal{Q}_h(\mathbf{s}, R_{\mathcal{S}})\,, \tag{4.51}$$

where we used (4.47) to define the vector $\mathbf{s} \triangleq (s_1, s_2, ..., s_m)$ and the functions $\mathcal{E}_h(\mathbf{s}) \triangleq \check{\mathcal{E}}(u_h)$ and $\mathcal{Q}_h(\mathbf{s}, R_{\mathcal{S}}) \triangleq \mathcal{Q}(u_h, R_{\mathcal{S}})$. The inner problem is a minimization problem in the vector variable $\mathbf{s}$ parameterized by $R_{\mathcal{S}}$. The outer problem is a minimization problem in the scalar variable $R_{\mathcal{S}}$, which we solve by using the golden-section search. See, for instance, Luenberger and Ye (2008).

We set the initial search interval of the golden section search to be $[R^a_{\mathcal{S}}, R^b_{\mathcal{S}}]$, where $R^a_{\mathcal{S}}$ and $R^b_{\mathcal{S}}$ are numerical parameters that must be chosen so that the initial search interval is large enough to contain $R_{\mathcal{S}}$ of the minimizer. At each iteration of the golden section search, we solve the inner minimization problem for intermediate values $R^c_{\mathcal{S}}, R^d_{\mathcal{S}} \in [R^a_{\mathcal{S}}, R^b_{\mathcal{S}}]$, which are given by[5] $R^c_{\mathcal{S}} = R^b_{\mathcal{S}} - (R^b_{\mathcal{S}} - R^a_{\mathcal{S}})/\psi$ and $R^d_{\mathcal{S}} = R^a_{\mathcal{S}} + (R^b_{\mathcal{S}} - R^a_{\mathcal{S}})/\psi$, where $\psi \triangleq (1 + \sqrt{5})/2$, using a standard Newton-Raphson method with a unidirectional search, as explained below. For large enough values of the penalty parameter δ_e, the solution of this inner minimization problem is expected to converge to a deformation field satisfying $\mathcal{Q}_h(\mathbf{s}) = 0$. Let $\mathbf{s}^c$ and $\mathbf{s}^d$ denote the solutions found using $R^c_{\mathcal{S}}$ and $R^d_{\mathcal{S}}$, respectively. Then, if $\mathcal{F}(\mathbf{s}^c, R^c_{\mathcal{S}}) < \mathcal{F}(\mathbf{s}^d, R^d_{\mathcal{S}})$, we set $R^b_{\mathcal{S}} = R^d_{\mathcal{S}}$; otherwise, we set $R^a_{\mathcal{S}} = R^c_{\mathcal{S}}$. Finally, if the new search interval $[R^a_{\mathcal{S}}, R^b_{\mathcal{S}}]$ is greater than 10^{-6}, we repeat the iteration; otherwise, we set $(\mathbf{s}, R_{\mathcal{S}}) = \text{argmin}\,\{\mathcal{F}(\mathbf{s}^c, R^c_{\mathcal{S}}), \mathcal{F}(\mathbf{s}^d, R^d_{\mathcal{S}})\}$ as the solution of the minimization problem (4.51).

To solve the inner problem in (4.51), we use a standard Newton-Raphson method with a unidirectional search; see, for instance, Luenberger and Ye (2008). Thus, starting

[4] In Appendix C, we present numerical results concerning a standard numerical formulation, which does not include $R_{\mathcal{S}}$ as a variable of the problem. These results are convergent only if the pressure is small enough so that the minimizer is smooth, that is, if $p < \bar{p}$ as we have seen in Section 4.3.2. For $p > \bar{p}$, the procedure fails to obtain convergent results. These results, however, motivated us to formulate the discrete problem as in (4.51).

[5] By definition, the golden section search is a Fibonacci search whose interval of uncertainty tends to zero. This definition yields the expressions of $R^c_{\mathcal{S}}$ and $R^d_{\mathcal{S}}$ (Luenberger; Ye, 2008).

from an initial guess $\mathbf{s}_0$, we generate a sequence of vectors $\mathbf{s}_k$, $k = 1, 2, 3, ...$, using the recursive formula

$$\mathbf{s}_{k+1} = \mathbf{s}_k + \alpha_k \, \mathbf{d}_k \,, \tag{4.52}$$

where $\mathbf{d}_k \in \mathbb{R}^m$ is a search direction and $\alpha_k \in \mathbb{R}$ is a step length. Below, we shall omit the dependence of $\mathcal{F}$ on the parameter $R_{\mathcal{S}}$.

The search direction $\mathbf{d}_k$ is given by

$$\mathbf{d}_k = - \left[\nabla^2_{\mathbf{s}} \mathcal{F}(\mathbf{s}_k) \right]^{-1} \nabla_{\mathbf{s}} \mathcal{F}(\mathbf{s}_k) \,, \tag{4.53}$$

where $\nabla_{\mathbf{s}} \mathcal{F} \triangleq (\partial \mathcal{F}/\partial s_1, \partial \mathcal{F}/\partial s_2, ..., \partial \mathcal{F}/\partial s_m)$ is the gradient of $\mathcal{F}$ with respect to $\mathbf{s}$ and $\nabla^2_{\mathbf{s}} \mathcal{F}$ is the Hessian of $\mathcal{F}$. The step length α_k is the minimizer of the unidirectional minimization problem

$$\min_{\alpha \in \mathbb{R}} \mathcal{H}(\alpha) \,, \qquad \mathcal{H}(\alpha) \triangleq \mathcal{F}(\mathbf{s}_k + \alpha \, \mathbf{d}_k) \,. \tag{4.54}$$

Starting from $\alpha^{(0)} = 0$, we use the recursive formula

$$\alpha^{(i+1)} = \alpha^{(i)} - \left(\frac{\mathrm{d}\mathcal{H}/\mathrm{d}\alpha}{\mathrm{d}^2\mathcal{H}/\mathrm{d}\alpha^2} \right) \Big|_{\alpha = \alpha^{(i)}} \tag{4.55}$$

to generate a sequence of values $\alpha^{(i)}$, which is expected to converge to α_k as $i \to \infty$. This sequence is truncated and we set $\alpha_k = \alpha^{(i+1)}$ when the following stop criterium is satisfied.

$$\frac{\left| \mathbf{d}_k \cdot \nabla_{\mathbf{s}} \mathcal{F}(\mathbf{s}_k + \alpha^{(i+1)} \, \mathbf{d}_k) \right|}{|\mathbf{d}_k| \, |\nabla_{\mathbf{s}} \mathcal{F}(\mathbf{s}_k + \alpha^{(i+1)} \, \mathbf{d}_k)|} < \varepsilon_\alpha \qquad \text{or} \qquad i + 1 = N_\alpha \,, \tag{4.56}$$

where $\varepsilon_\alpha > 0$ is an adopted tolerance and N_α is the maximum number of iterations allowed. The inequality (4.56.a) states that the search direction $\mathbf{d}_k$ and the gradient of the objective function $\mathcal{F}$ must be orthogonal to each other to within an error ε_α. For the Mooney-Rivlin material, we check if α_k yields $\det \mathbf{F} = \nu \, \tau > 0$ at all quadrature points; otherwise, we halve α_k until this condition is verified. Recall from the discussion of Figure 5 that, despite $\nu > 0$ yielding the whole range of $\hat{P}^{\mathrm{mr}}_{rr}$, $\nu < 0$ is mathematically possible. This verification makes the step length small enough so $\nu < 0$ is not reached. For the St Venant-Kirchhoff material, this verification is not done since, recalling from the discussion of (4.33), a non-smooth minimizer necessarily has $\det \mathbf{F} \leq 0$ on one of the sides of $\mathcal{S}$; additionally, $\nu > 0$ does not yield the whole range of $\hat{P}^{\mathrm{vk}}_{rr}$ like in the Mooney-Rivlin case.

Let $\mathbf{u}^k_h = u^k_h \, \mathbf{e}_R$ denote the approximate displacement field associated with $\mathbf{s}_k$ through (4.47). The stop criterium used to truncate the sequence of vectors $\mathbf{s}_k$, $k = 1, 2, 3, ...$, is

$$\left\| \mathbf{u}^{k+1}_h - \mathbf{u}^k_h \right\|_{H_1} < \varepsilon_{\mathbf{s}} \,, \tag{4.57}$$

where $\varepsilon_{\mathbf{s}} > 0$ is an adopted tolerance and $||\mathbf{u}_h^{k+1} - \mathbf{u}_h^k||_{H_1}$ is the H_1-norm of $\mathbf{u}_h^{k+1} - \mathbf{u}_h^k$, which is given by

$$\begin{aligned}\left|\left|\mathbf{u}_h^{k+1} - \mathbf{u}_h^k\right|\right|_{H_1} &= \left[\int_{\mathcal{B}} \left(\left|\mathbf{u}_h^{k+1} - \mathbf{u}_h^k\right|^2 + \left|\nabla\mathbf{u}_h^{k+1} - \nabla\mathbf{u}_h^k\right|^2\right) \mathrm{d}\mathbf{x}\right]^{1/2} \\ &= \left\{2\,\pi \int_{R_i}^{R_e} \left[R\left(\frac{\mathrm{d}u_h^{k+1}}{\mathrm{d}R} - \frac{\mathrm{d}u_h^k}{\mathrm{d}R}\right)^2 + \left(R + \frac{1}{R}\right)\left(u_h^{k+1} - u_h^k\right)^2\right] \mathrm{d}R\right\}^{1/2}.\end{aligned} \tag{4.58}$$

4.4.2 Numerical results

We use the numerical procedure presented in the previous section to determine approximate solutions of the disk MP. We use $R_i = 0.001$, $R_e = 1$, and the elastic constants c_{11}, c_{12}, c_{22} given by (4.26), which were used in Section 4.3. Also from this section, we find that $\bar{p} = 0.013773$; since here we are interested in non-smooth solutions, we choose $p = 0.05 > \bar{p}$. In addition, we use $[0.9\,R_i, 0.01\,R_e]$ as the initial search interval of the golden-section search presented below (4.51), $\delta_e = 1000$ in (5.35), $\varepsilon_{\mathbf{s}} = 10^{-6}$ in (4.57), $\varepsilon_\alpha = 10^{-6}$ and $N_\alpha = 50$ in (4.56), and non-uniform meshes parameterized by $q \in \mathbb{N}$ and composed of $N = 24 \times 2^q$ linear finite elements distributed in three intervals: 15×2^q elements in $R_i < R < 0.1\,R_e$, 5×2^q elements in $0.1\,R_e < R < 0.5\,R_e$, and 4×2^q elements in $0.5\,R_e < R < R_e$. These meshes are similar to the meshes used by Aguiar and Rocha (2021) and Aguiar, Fosdick and Sanchez (2008). The initial guess used in the numerical procedure is given by $\mathbf{s}_0 = \mathbf{0}$, which corresponds to the undistorted reference configuration.

First, we consider the St Venant-Kirchhoff material. In Figure 11, we show ν (left) and P_{rr} (right) versus the radius in a neighborhood of the inner surface of the disk. The colored lines refer to approximate solutions of the nonlinear disk problem obtained with a sequence of increasing mesh refinements. The black solid lines refer to the corresponding fields, either ν or P_{rr}, obtained with the linear solution, which is given by (4.17). We see from this figure that the numerical approximations of both ν and P_{rr} tend to limit functions that satisfy both (4.29) and (4.33) and are considerably different from their linear counterparts near the inner surface of the disk. We have verified that, for our most refined mesh, which corresponds to $q = 10$, the jump discontinuity of ν occurs at the position $R_{\mathcal{S}} = 0.00554$ where $\nu^- \approx -1.0093$, $\nu^+ \approx 1.0094$, and $\bar{P}_{rr} \approx -0.0016$, which is in good agreement with (4.29) and (4.33). Recall from Section 4.2.2, that (4.29) and (4.33) correspond to the traction continuity and dissipation-free conditions, given by (3.87) and (3.88), respectively, which are necessary conditions for a deformation field to be a minimizer of total potential energy. Since τ is continuous and positive at $R_{\mathcal{S}}$, we have that $\det \mathbf{F} = \nu^-\,\tau < 0$, which is not acceptable.

Figure 12 is the analogue of Figure 11 for the Mooney-Rivlin material with the elastic constant $c_{33} = c_{22}/5$. Again, the curves are significantly different from their linear counterpart near the inner radius because of the discontinuity of ν. We have verified

that, at this discontinuity, both the traction continuity and dissipation-free conditions, given by (4.8) and (4.9), are satisfied. Recall from Section 4.2.1 that the responses of P_{rr} and $P_{\theta\theta}$ depend on c_{33}; in fact, this elastic constant is critical for the emergence of the discontinuity in ν, which, recalling from Chapter 2, is of interest in the modeling of solids which undergoes stress-induced phase transformations. In Section 5.3, we present solutions for different values of c_{33} and compare them with the solutions obtained with the constrained minimization theory.

Figure 11 – Radial stretch ν and radial normal stress P_{rr} versus R using the St Venant-Kirchhoff material.

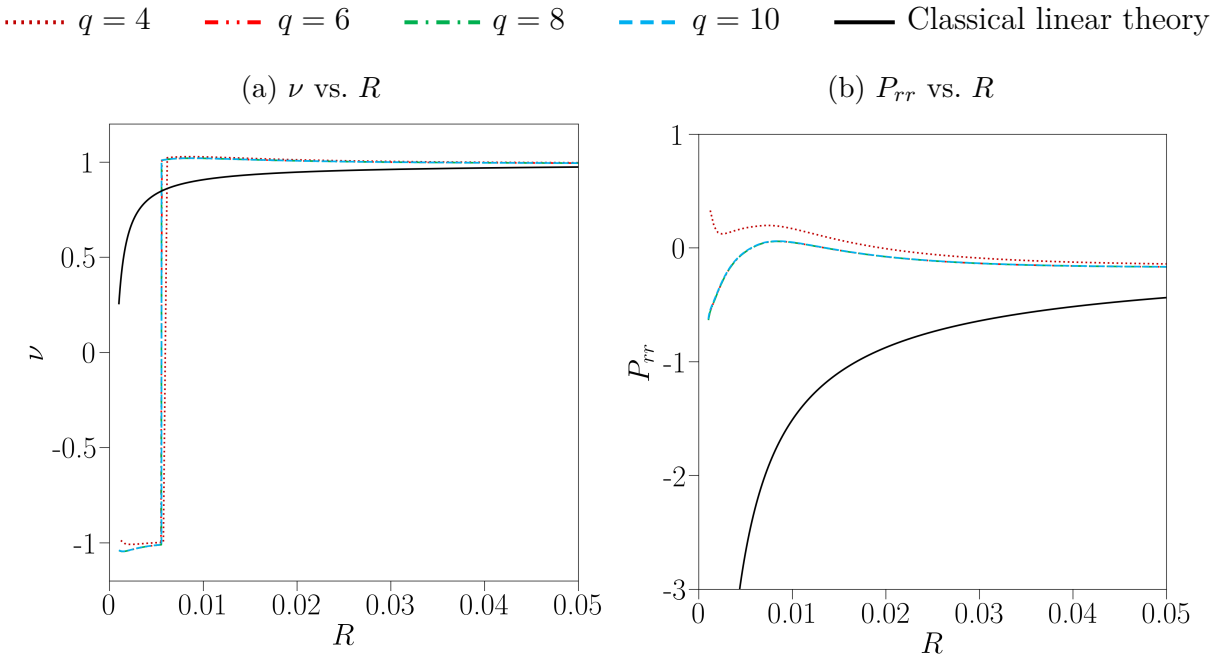

Source: The author.

Figure 12 – Radial stretch ν and radial normal stress P_{rr} versus R using the Mooney-Rivlin material.

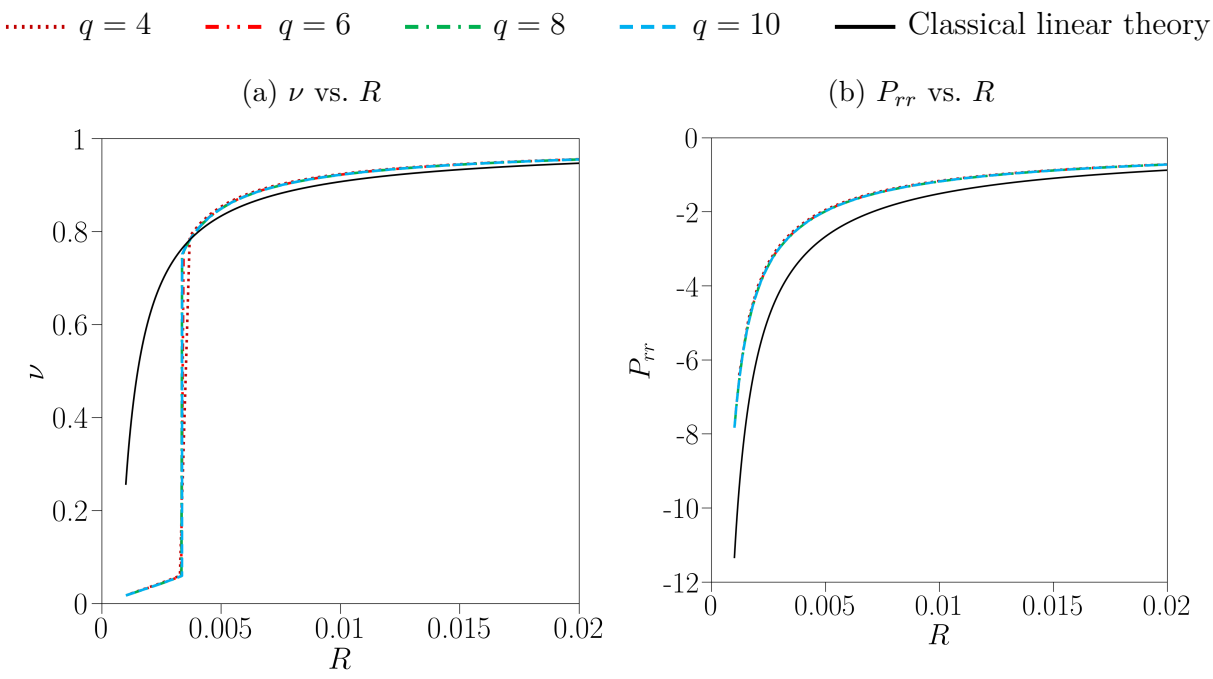

Source: The author.

5 THE CONSTRAINED DISK PROBLEM

In this chapter, we impose the local injectivity constraint, $\det \mathbf{F} \geq \varepsilon > 0$, in the disk problem studied in the previous chapter. Again, we find approximate solutions using both a phase-plane technique and a finite element formulation. The former is used to solve a boundary value problem obtained from the Euler-Lagrange equations derived in Section 3.6. The latter is used to solve a constrained minimization problem. In addition, we compare the solutions obtained with both the constrained minimization theory and the classical nonlinear elasticity using the orthotropic and compressible Mooney-Rivlin material.

5.1 Formulation of the constrained problem

As we have seen in the discussion of (4.33), in the unconstrained disk problem, a jump in ν corresponds to a jump in $\det \mathbf{F}$ from a positive to a negative value; thus, violating the local injectivity constraint. In addition, ν is continuous in $\mathcal{B}_=$ since, in this region, $\det \mathbf{F} = \nu\,\tau = \varepsilon$, τ is continuous, and ε is a constant. Therefore, in the constrained disk problem, a jump in ν must occur on Σ, which is the interface between $\mathcal{B}_=$ and $\mathcal{B}_>$. This allows us to rewrite the the Euler-Lagrange equations (3.111) as

$$\operatorname{Div} \mathbf{P}_a + \mathbf{b} = \mathbf{0} \qquad \text{in } \mathcal{B}_= \cup \mathcal{B}_> \,, \tag{5.1}$$

where we use (3.110), (4.5), (4.3) to write $\mathbf{P}_a$ as

$$\mathbf{P}_a = P^a_{rr}(R)\,\mathbf{e}_r \otimes \mathbf{e}_R + P^a_{\theta\theta}(R)\,\mathbf{e}_\theta \otimes \mathbf{e}_\Theta + P^a_{zz}(R)\,\mathbf{e}_z \otimes \mathbf{e}_Z \,, \tag{5.2}$$

$$P^a_{rr}(R) = \hat{P}^a_{rr}(\nu,\tau,\lambda) \triangleq \hat{P}_{rr}(\nu,\tau) - \lambda\,\tau \,, \tag{5.3}$$

$$P^a_{\theta\theta}(R) = \hat{P}^a_{\theta\theta}(\nu,\tau,\lambda) \triangleq \hat{P}_{\theta\theta}(\nu,\tau) - \lambda\,\nu \,. \tag{5.4}$$

The expression of P^a_{zz} is omitted because it does not contribute to the governing equations of equilibrium. In addition, we use $\hat{P}_{rr} = \hat{P}^{\mathrm{vk}}_{rr}$ and $\hat{P}_{\theta\theta} = \hat{P}^{\mathrm{vk}}_{\theta\theta}$, which are given by (4.6) and (4.7), respectively, because we impose the local injectivity constraint only for the St Venant-Kirchhoff model.

Recall from Sections 4.3.2 and 4.4.2 that, in the unconstrained case, $\det \mathbf{F} < 0$ in a neighborhood of the inner surface of the disk. Here, we assume that there exists a radius R_Σ, corresponding to the position of the interface Σ, such that the expressions in (3.98) become

$$\mathcal{B}_= = \{\mathbf{x} \in \mathcal{B} \,|\, R_i < R < R_\Sigma\} \,, \qquad \mathcal{B}_> = \{\mathbf{x} \in \mathcal{B} \,|\, R_\Sigma < R < R_e\} \,. \tag{5.5}$$

The radius R_Σ is not known *a priori* and is determined from the solution of the constrained problem presented below.

Using both (5.2) and $\mathbf{b} = \mathbf{0}$, we reduce the vector equilibrium equation (5.1) to the scalar differential equation

$$\frac{\mathrm{d}}{\mathrm{d}R}\left[R\, P^a_{rr}(R)\right] - P^a_{\theta\theta}(R) = 0 \qquad \text{in } (R_i, R_\Sigma) \cup (R_\Sigma, R_e)\,. \tag{5.6}$$

At $R = R_\Sigma$, the conditions (3.115) and (3.116) become

$$P^a_{rr}(R_\Sigma^-) = P^a_{rr}(R_\Sigma^+) \triangleq \bar{P}^a_{rr}\,, \qquad \hat{W}(\nu^>, \tau) - \hat{W}(\nu^=, \tau) - (\nu^> - \nu^=)\,\bar{P}^a_{rr} = 0\,, \tag{5.7}$$

respectively, where $\nu^> = \nu(R_\Sigma^+)$ and $\nu^= = \nu(R_\Sigma^-)$. In view of the expressions in (5.5) and the definition of λ introduced in Section 3.6, we obtain

$$\det \mathbf{F} = \nu\,\tau = \varepsilon \quad \text{in } (R_i, R_\Sigma)\,, \qquad \lambda = 0 \quad \text{in } (R_\Sigma, R_e)\,, \tag{5.8}$$

where λ may be discontinuous at $R = R_\Sigma$ in order for (5.7) to be satisfied. In addition, boundary conditions analogous to (4.11) are given by

$$r(R_i) = R_i\,, \qquad P^a_{rr}(R_e) = -p\,\frac{r(R_e)}{R_e}\,, \tag{5.9}$$

where P^a_{rr} is given by (5.3).

Thus, the *constrained disk BVP* consists of determining the radial deformation $r : [R_i, R_e] \to \mathbb{R}$ and Lagrange multiplier $\lambda : [R_i, R_e] \to \mathbb{R}$ that satisfy the differential equation (5.6) together with (5.3), (5.4), (5.8), (5.7), (5.9), and (4.3.b,c).

Similarly to the disk MP introduced in Section 4.1, the *constrained disk MP* consists of finding $u_r : [R_i, R_e] \to \mathbb{R}$ that minimizes the functional $\check{\mathcal{E}}(u_r)$, given by (4.12), and satisfies both $u_r(R_i) = 0$ and $\det \mathbf{F} = (1 + u_r')\,(1 + u_r/R) \geq \varepsilon$. In Sections 5.2 and 5.3, we conduct a detailed investigation of the constrained disk BVP and the constrained disk MP, respectively.

Remark 4 (The constrained linearly elastic disk BVP). The analogous version of the constrained disk BVP in the context of the classical linear elasticity is referred to as the *constrained linearly elastic disk BVP* and was studied by Fosdick and Royer-Carfagni (2001) and by Aguiar, Fosdick and Sanchez (2008) in the cases $R_i = 0$ and $R_i \geq 0$, respectively. These authors determined analytical solutions for both r and λ in the whole disk. In $\mathcal{B}_=$, they are given by

$$r(R) = \sqrt{(R^2 - R_i^2)\,\varepsilon + R_i^2}\,, \tag{5.10}$$

$$\begin{aligned}\lambda(R) = c_{11}\Bigg\{ &-\frac{(1-\varepsilon)\,R_i^2}{2}\left(\frac{1}{r(R)^2} - \frac{1}{r_\Sigma^2}\right) + \log\left(\frac{r(R)}{r_\Sigma}\right) \\ &- \kappa^2\,\log\left(\frac{R}{R_\Sigma}\right) - \frac{1-\kappa^2}{\sqrt{\varepsilon}}\log\left(\frac{\sqrt{\varepsilon}\,R + r(R)}{\sqrt{\varepsilon}\,R_\Sigma + r_\Sigma}\right)\Bigg\}\,,\end{aligned} \tag{5.11}$$

$$\kappa \triangleq \sqrt{\frac{c_{22}}{c_{11}}}\,, \qquad r_\Sigma \triangleq r(R_\Sigma)\,, \tag{5.12}$$

for $R_i > 0$, and by

$$r(R) = R\sqrt{\varepsilon}\,, \tag{5.13}$$

$$\lambda(R) = -\frac{1-\sqrt{\varepsilon}}{\sqrt{\varepsilon}}\,(c_{11}-c_{22})\,\log\left(\frac{R}{R_\Sigma}\right) \tag{5.14}$$

for $R_i = 0$. The expression for r in $\mathcal{B}_>$, where $\lambda = 0$, is given by

$$r(R) = R + \beta_1\,R^{\kappa} + \beta_2\,R^{-\kappa}\,, \tag{5.15}$$

where

$$\begin{cases} \beta_1 \triangleq \dfrac{R_\Sigma^{-\kappa+1}}{2\,\kappa}\left[-1-\kappa+\kappa\,\dfrac{r_\Sigma}{R_\Sigma}+\varepsilon\,\dfrac{R_\Sigma}{r_\Sigma}\right], \\ \beta_2 \triangleq \dfrac{R_\Sigma^{\kappa+1}}{2\,\kappa}\left[1-\kappa+\kappa\,\dfrac{r_\Sigma}{R_\Sigma}-\varepsilon\,\dfrac{R_\Sigma}{r_\Sigma}\right], \end{cases} \tag{5.16}$$

for $R_i \geq 0$. In addition, R_Σ is determined by solving the algebraic equation

$$\Gamma(\zeta,\kappa)+\Gamma(\zeta,-\kappa)+\frac{p}{c_{11}} = 0\,, \qquad \zeta \triangleq \frac{R_\Sigma}{R_e}\,, \tag{5.17}$$

where

$$\Gamma(\zeta,\kappa) \triangleq \frac{\kappa + c_{12}/c_{11}}{2\,\kappa}\,\zeta^{1-\kappa}\,\left[-1-\kappa+\kappa\,\frac{\gamma(\zeta)}{\zeta}+\varepsilon\,\frac{\zeta}{\gamma(\zeta)}\right], \tag{5.18}$$

$$\gamma(\zeta) \triangleq \sqrt{\varepsilon\,\zeta^2+(1-\varepsilon)\left(\frac{R_i}{R_e}\right)^2}\,. \tag{5.19}$$

5.2 The constrained disk boundary value problem

We study the constrained disk BVP by, first, finding its solution in $\mathcal{B}_=$ analytically and, then, applying the phase-plane technique to search for a solution in the whole domain.

5.2.1 Analytical solution in the active region $\mathcal{B}_=$

In $\mathcal{B}_=$, the field r must satisfy the ordinary differential equation $\det\mathbf{F} = \nu\,\tau = r'\,r/R = \varepsilon$ and the boundary condition $r(R_i) = R_i$. This yields the expression (5.10) for $R_i > 0$ and the expression (5.13) for $R_i = 0$. Thus, in $\mathcal{B}_=$, the field r coincides in the constrained disk BVP and its constrained linear counterpart, which is given by (5.10) and (5.13). Despite that, λ does not coincide, as we will see below.

We use (5.3), (5.4), and (4.3.b,c) to rewrite the differential equation (5.6) as

$$\begin{aligned} &\left[c_{11}\,\left(3\,(r')^2-1\right)+c_{12}\,\left(\frac{r^2}{R^2}-1\right)\right]r'' - \left[c_{11}+c_{12}\left(\frac{r^2}{R^2}+1\right)\right]\frac{r'}{R} \\ &+ c_{11}\,\frac{(r')^3}{R}+c_{12}\,\frac{(r')^2\,r}{R^2}+(c_{12}+c_{22})\,\frac{r}{R^2}-c_{22}\,\frac{r^3}{R^4}-2\,\lambda'\,\frac{r}{R} = 0\,. \end{aligned} \tag{5.20}$$

We then substitute (5.10) into (5.20) and integrate λ' to obtain

$$\begin{aligned}\lambda(R) = K &+ \frac{3\,R_i^2\,c_{11}\,\varepsilon^2\,(\varepsilon-1)}{8}\,\frac{R^2}{r^4} + \frac{R_i^2\,(\varepsilon-1)[\varepsilon\,c_{11}-2\,c_{11}-2\,c_{12}]}{8\,r^2} \\ &+ \frac{(\varepsilon-1)\,c_{11}-c_{12}}{2}\,\log(r) - \frac{(\varepsilon-1)\,c_{22}-c_{12}}{2}\,\log(R) \\ &- \frac{R_i^2\,c_{22}\,(\varepsilon-1)}{4\,R^2} \qquad \text{in } \mathcal{B}_{=}\,,\end{aligned} \tag{5.21}$$

where K is a constant of integration and r is given by (5.10). In the case $R_i = 0$, (5.21) becomes

$$\lambda(R) = K_0 + \frac{(\varepsilon-1)\,(c_{11}-c_{22})}{2}\,\log R \qquad \text{in } \mathcal{B}_{=}\,, \tag{5.22}$$

$$K_0 \triangleq K + \frac{(\varepsilon-1)\,c_{11}-c_{12}}{4}\,\log\varepsilon\,. \tag{5.23}$$

Also, the continuity conditions (5.7) can be written as

$$\hat{P}^a_{rr}(\nu^{>},\tau_\Sigma,0) - \hat{P}^a_{rr}(\nu^{=},\tau_\Sigma,\lambda^{=}) = 0\,, \tag{5.24}$$

$$\hat{W}(\nu^{>},\tau_\Sigma) - \hat{W}(\nu^{=},\tau_\Sigma) + \nu^{>}\,\hat{P}^a_{rr}(\nu^{>},\tau_\Sigma,0) - \nu^{=}\,\hat{P}^a_{rr}(\nu^{=},\tau_\Sigma,\lambda^{=}) = 0\,, \tag{5.25}$$

where $\lambda^{=} = \lambda(R_\Sigma^{-})$, P^a_{rr} is given by (5.3), and

$$\hat{W}(\nu,\tau) = \frac{1}{4}\Big\{(\nu^2-1)\,[c_{11}\,(\nu^2-1)+c_{12}\,(\tau^2-1)]+(\tau^2-1)\,[c_{12}\,(\nu^2-1)+c_{22}\,(\tau^2-1)]\Big\}\,. \tag{5.26}$$

In both (5.24) and (5.25), $\nu^{=} = r'(R_\Sigma^{-})$ and $\tau_\Sigma = r(R_\Sigma)/R_\Sigma$, where r is given by (5.10). Both (5.24) and (5.25) can be used to determine $\lambda^{=}$ and $\nu^{>}$ in terms of R_Σ. To determine R_Σ, we should first find r in $\mathcal{B}_{>}$ as the general solution of the differential equation (5.20) with $\lambda \equiv 0$. Then, R_Σ and the constants of integration of this general solution are obtained from $r'(R_\Sigma^{+}) = \nu^{>}$, the continuity of r at R_Σ, and the boundary condition (5.9.b). In this work, we do not find r in $\mathcal{B}_{>}$ analytically. Instead, we find numerical approximations of r using both the phase-plane technique in Section 5.2.2 and the finite element method in Section 5.3.2.

Next, we investigate the behavior of λ in the cases of $R_i = 0$ and $\varepsilon \to 0$. For $R_i = 0$, we see from (5.22) that λ is singular at the center of the disk. In fact, it has the same log-singularity of its constrained linear counterpart given by (5.14). For $\varepsilon \to 0$, we see from both (5.21) and (5.22) that bounded values of λ depend on whether K and K_0 are also bounded.

Now, we show that K remains bounded and K_0 becomes unbounded for $\varepsilon \to 0$. For this, we solve (5.24) for $\lambda^{=}$ and substitute the resulting expression into (5.25). We then obtain a fourth-order polynomial in $\nu^{>}$, which, in the case of $\varepsilon \to 0$, is given by

$$(\nu^{>})^2\left[(\nu^{>})^2 + \frac{2}{3}\left(-\tilde{c} - 1 + \tilde{c}\,\frac{R_i^2}{R_\Sigma^2}\right)\right] = 0\,, \qquad \tilde{c} \triangleq \frac{c_{12}}{c_{11}}\,. \tag{5.27}$$

Its positive root is given by

$$\nu^{>} = \frac{\sqrt{6}}{3} \frac{\sqrt{R_\Sigma^2 + \tilde{c}\,(R_\Sigma^2 - R_i^2)}}{R_\Sigma}\,. \tag{5.28}$$

Substituting $\nu^{>}$, given by (5.28), into the expression of $\lambda^{=}$ mentioned above, we find that

$$\lambda^{=} = c_{11}\,\frac{\sqrt{6}}{18}\,\frac{[R_\Sigma^2 + \tilde{c}\,(R_\Sigma^2 - R_i^2)]^{3/2}}{R_i\,R_\Sigma^2}\,, \tag{5.29}$$

which is finite for $R_i > 0$. Thus, K is also finite and, consequently, λ for $R_i > 0$. This behavior is qualitatively similar to the behavior of its constrained linear counterpart given by (5.11), which is also bounded for $\varepsilon \to 0$. In Section 5.3.2, we show numerical results obtained with the finite element method that confirm these findings. Next, by taking $R_i \to 0$ in (5.29), we see that $\lambda^{=}$ becomes unbounded; thus, both K_0 and λ also become unbounded, yielding the same type of behavior of its constrained linear counterpart given by (5.14).

5.2.2 Numerical solution in the whole disk

In the previous section, we studied the solution of the constrained disk BVP in $\mathcal{B}_{=}$, which corresponds to the region where the local injectivity constraint is active. Let us now study its solution in the whole disk. For that, we construct trajectories of solutions on the plane $\mathcal{U}^a \triangleq \{(\tau, P_{rr}^a)\,|\,\tau, P_{rr}^a \in \mathbb{R}\}$. Similarly to Section 4.3, we change variables by introducing $\xi = \log R$ and write the differential equation (5.6) as the system of autonomous differential equations given by

$$\begin{aligned} \frac{\mathrm{d}\tau}{\mathrm{d}\xi} &= \check{\nu}(\tau, P_{rr}^a) - \tau\,, \\ \frac{\mathrm{d}P_{rr}^a}{\mathrm{d}\xi} &= \check{P}_{\theta\theta}^a(\tau, P_{rr}^a) - P_{rr}^a\,, \end{aligned} \tag{5.30}$$

where, here, $\check{P}_{\theta\theta}^a(\tau, P_{rr}^a) \triangleq \hat{P}_{\theta\theta}^a(\check{\nu}(\tau, P_{rr}^a), \tau)$, with $\hat{P}_{\theta\theta}^a$ given by (5.4).

To determine a trajectory of solution of the constrained disk BVP, we need to calculate $\check{\nu}(\tau, P_{rr}^a)$ and $\check{P}_{\theta\theta}^a(\tau, P_{rr}^a)$. If (τ, P_{rr}^a) corresponds to a deformation field satisfying $\det \mathbf{F} > \varepsilon$, we have $\lambda = 0$ and we recover the unconstrained case, where $\check{\nu}(\tau, P_{rr}^a)$ is given by the solution of the cubic equation (4.41) with $P_{rr} = P_{rr}^a$. Recall from the discussion below the equation (4.42) that this cubic equation has the three distinct real roots $\nu_i(\tau, P_{rr}^a)$, $i = 1, 2, 3$, if $D(\tau, P_{rr}^a) > 0$. In view of the discussion of the Figures 7 and 8, we set $\check{\nu}(\tau, P_{rr}^a) = \nu_3$. If (τ, P_{rr}^a) corresponds to a deformation field for which $\det \mathbf{F} = \varepsilon$, we have that $\check{\nu}(\tau, P_{rr}^a) = \varepsilon/\tau$. In addition, in this case, $\lambda \neq 0$ is obtained from (5.3) as

$$\lambda = \frac{1}{\tau}\,(\hat{P}_{rr} - P_{rr}^a)\,, \qquad \hat{P}_{rr} = \hat{P}_{rr}^{\mathrm{vk}}(\check{\nu}(\tau, P_{rr}^a), \tau)\,. \tag{5.31}$$

After $\check{\nu}(\tau, P_{rr}^a)$ is calculated, $\check{P}_{\theta\theta}^a(\tau, P_{rr}^a)$ is obtained from its definition below (5.30).

Similar to (4.40), we define initial and terminal curves for the constrained disk BVP as, respectively,

$$\mathcal{C}_i \triangleq \{(\tau, P^a_{rr}) \in \mathcal{U}^a \mid \tau = 1\}, \qquad \mathcal{C}_e(p) \triangleq \{(\tau, P^a_{rr}) \in \mathcal{U}^a \mid P^a_{rr} = -p\,\tau\}\,. \tag{5.32}$$

In addition, we use (3.116) with $\mathbf{N} = \mathbf{e}_R$, (4.3.a), and (5.2) to define the curve

$$\mathcal{C}_\Sigma \triangleq \{(\tau, P^a_{rr}) \in \mathcal{U}^a \mid [\hat{W}(\check{\nu}, \tau) + \check{\nu}\, P^a_{rr}]^+_- = 0\,,\ \check{\nu} = \check{\nu}(\tau, P^a_{rr})\}\,, \tag{5.33}$$

which is used below for determining R_Σ. Recall from Section 5.1 that, in the constrained disk problem, a jump in ν must occur at $R = R_\Sigma$, which is the position of the interface Σ.

In Section 4.3.2, we constructed a trajectory of solution for the unconstrained disk problem in its forward direction, that is, we began on the initial curve $\mathcal{C}_i$, at $R = R_i$, and, by using the recursive formula (4.44), we marched towards the terminal curve $\mathcal{C}_e$, where the distance of the last point to this curve was within a small error. In this section, however, we do not know, *a priori*, whether the constraint of injectivity is active or not at $R = R_i$, and, thus, we cannot determine $(\mathrm{d}\tau/d\xi, \mathrm{d}P^a_{rr}/d\xi)$ from (5.30). Since the local injectivity constraint is not active at $R = R_e$ for reasonable values of pressure, we construct a trajectory of solution for the constrained disk problem in the backward direction like in Section 4.3.3, that is, the initial point belongs to the terminal curve $\mathcal{C}_e$ and, for $R_i > 0$, it ends near the initial curve $\mathcal{C}_i$ to within a small error. The trajectory will cross the curve $\mathcal{C}_\Sigma$ for p large enough and ε small enough, in which case the injectivity constraint becomes active. For small p, $\det \mathbf{F} > \varepsilon$ and, therefore, the trajectory will not cross the curve $\mathcal{C}_\Sigma$. For large ε, say $\varepsilon = 0.5$, we have verified that the constraint becomes active without crossing the curve $\mathcal{C}_\Sigma$. In this work, we are interested in small values of ε; so, the case of large ε is not presented.

Here, we generate a set of points $\{(\tau^j, P^{a\,j}_{rr})\}$, $j = 1, 2, ..., N$, using the recursive formula

$$(\tau^{j+1}, P^{a\,j+1}_{rr}) = (\tau^j, P^{a\,j}_{rr}) - \delta\xi_j \left(\frac{d\tau}{d\xi}, \frac{dP^a_{rr}}{d\xi}\right)\Big|_{(\tau^j, P^{a\,j}_{rr})}, \tag{5.34}$$

where $(\tau^1, P^{a\,1}_{rr}) \in \mathcal{C}_e$ and N is such that $\sum_{j=1}^N \delta\xi_j = \Delta\xi \triangleq \log R_e - \log R_i$. Thus, N is the total number of steps that are necessary to go from the terminal curve $\mathcal{C}_e$ to the initial curve $\mathcal{C}_i$ and depends on the choice of the step sizes $\delta\xi_j$. In addition, we use a simple iterative procedure to search for an initial point $(\tau^1, P^1_{rr}) \in \mathcal{C}_e$ such that $0.999 < \tau^N < 1.001$, that is, the last point (τ^N, P^N_{rr}) of the corresponding trajectory of solution is close to $\mathcal{C}_i$ to within a small error.

To show numerical results, we use the same geometrical parameters and elastic constants considered in Sections 4.3 and 4.4, that is, $R_i = 0.001$, $R_e = 1$, and c_{11}, c_{22}, c_{12} given by (4.26). In addition, the constraint parameter that appears in (5.8) is assumed to be $\varepsilon = 0.1$. In Figure 13, we show trajectories of solutions for three different values

Figure 13 – Trajectories of solutions of the constrained disk BVP for $R_i = 0.001$ and different values of p.

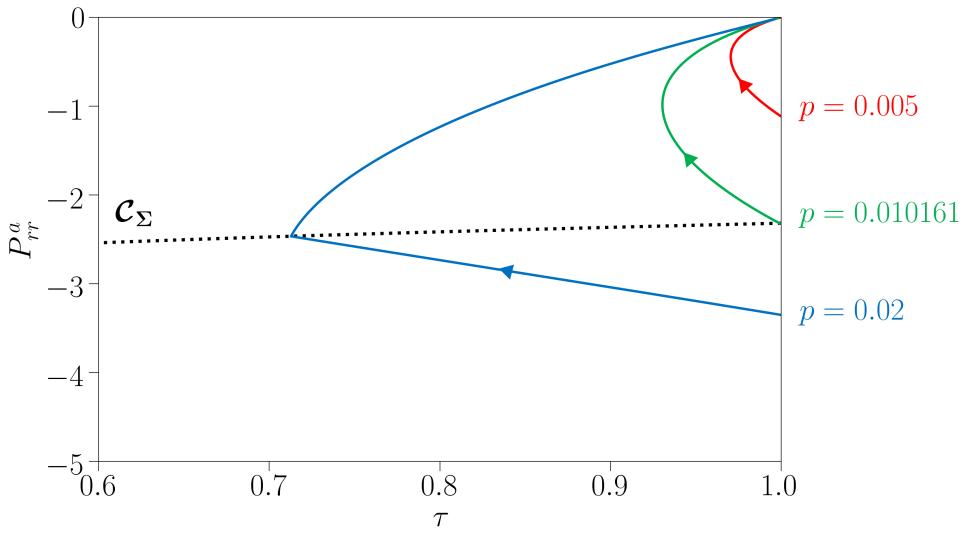

Source: The author.

of pressure, $p = 0.005, 0.010161, 0.02$. The black dotted line corresponds to $\mathcal{C}_\Sigma$, given by (5.33), and, as mentioned above, corresponds to the interface between $\mathcal{B}_>$ and $\mathcal{B}_=$ with the constraint $\det \mathbf{F} \geq \varepsilon$ being active in the segment of trajectory below the dotted line. Therefore, in the trajectories of solutions shown in Figure 13, the constraint is active in a neighborhood of the inner radius only for $p = 0.02$. The case $p = 0.010161$ corresponds to a critical value $\hat{p}$ above which the local injectivity constraint becomes active near the inner radius of the disk. This value is smaller than $\bar{p}$, which appears in Table 1 and corresponds to the solid green line in Figure 9. In any case, $\hat{p} < \bar{p}$ and both tend to zero as $R_i \to 0$. The trajectory of solution for the case $p = 0.005$ is the same one shown in Figure 9 and corresponds to a case for which the constraint is not active in any part of the disk.

5.3 The constrained disk minimization problem

We now turn our attention to the constrained disk MP. To solve this problem numerically, we adapt the numerical procedure used to solve the unconstrained disk MP in Section 4.4, which is also implemented in a C++ code using the open-source finite element library deal.ii (Arndt *et al.*, 2019).

5.3.1 Numerical procedure

We consider a finite element formulation of the constrained disk MP using an approximate minimizer $\mathbf{u}_h$ having the form (4.47). For comparison purposes, we impose the constraint $\det \mathbf{F} \geq \varepsilon$ using penalty and augmented Lagrangian formulations. For that,

we define the penalty functional

$$\mathcal{P}(u_r, R_\Sigma) \triangleq \frac{\delta}{2} \int_{\mathcal{B}_=} c^2 \, \mathrm{d}\mathbf{x} + \delta_e \int_{\mathcal{B}_>} \max\left(0, \nu_{e1} - \nu\right)^2 \mathrm{d}\mathbf{x} \tag{5.35}$$

and the Lagrangian functional

$$\mathcal{L}(u_r, \lambda, R_\Sigma) \triangleq \int_{\mathcal{B}_=} \left(-\lambda \, c + \frac{\delta}{2} \, c^2 \right) \mathrm{d}\mathbf{x} + \delta_e \int_{\mathcal{B}_>} \max\left(0, \nu_{e1} - \nu\right)^2 \mathrm{d}\mathbf{x} \,, \tag{5.36}$$

where $\nu = u_r' + 1$, ν_{e1} is given by (4.22.a), $\lambda = \lambda(R)$ is the Lagrange multiplier field associated with the constraint $c \triangleq \det \mathbf{F} - \varepsilon = 0$ in $\mathcal{B}_=$, $\delta > 0$ and $\delta_e > 0$ are penalty parameters, and both $\mathcal{B}_=$ and $\mathcal{B}_>$ are given by (5.5).

In the penalty formulation, the discrete version of the constrained disk MP can be written as

$$\min_{R_\Sigma \in \mathbb{R}} \quad \min_{\mathbf{s} \in \mathbb{R}^m} \mathcal{F}(\mathbf{s}, R_\Sigma) \,, \qquad \mathcal{F}(\mathbf{s}, R_\Sigma) = \mathcal{E}_h(\mathbf{s}) + \mathcal{P}_h(\mathbf{s}, R_\Sigma) \,, \tag{5.37}$$

where we used (4.47) to introduce the vector $\mathbf{s} \triangleq (s_1, s_2, ..., s_m)$ and to define the functions $\mathcal{E}_h(\mathbf{s}) \triangleq \check{\mathcal{E}}(u_h)$ and $\mathcal{P}_h(\mathbf{s}, R_\Sigma) \triangleq \mathcal{P}(u_h, R_\Sigma)$. In the augmented Lagrangian formulation, we introduce a finite element approximation of λ, which is given by

$$\lambda_h = \sum_{i=1}^{m_\lambda} l_i \, \hat{w}_i \,, \tag{5.38}$$

where $l_i \in \mathbb{R}$, $i = 1, 2, 3, ..., m_\lambda$, is a degree of freedom, m_λ is the number of degrees of freedom associated with the approximation of λ, and $\hat{w}_i$ is a shape function of the finite element approximation. Then, the discrete version of the constrained disk MP can be written as

$$\min_{R_\Sigma \in \mathbb{R}} \quad \left[\max_{\mathbf{l} \in \mathbb{R}^{m_\lambda}} \quad \min_{\mathbf{s} \in \mathbb{R}^m} \mathcal{F}(\mathbf{s}, \mathbf{l}, R_\Sigma) \right] , \qquad \mathcal{F}(\mathbf{s}, \mathbf{l}, R_\Sigma) = \mathcal{E}_h(\mathbf{s}) + \mathcal{L}_h(\mathbf{s}, \mathbf{l}, R_\Sigma) \,, \tag{5.39}$$

where we used both (4.47) and (5.38) to define the vector $\mathbf{l} \triangleq (l_1, l_2, ..., l_{m_\lambda})$ and the function $\mathcal{L}_h(\mathbf{s}, \mathbf{l}, R_\Sigma) \triangleq \mathcal{L}(u_h, \lambda_h, R_\Sigma)$.

In both (5.37) and (5.39), the outer problem is a minimization problem in the scalar variable R_Σ, which we solve by using the golden section search explained in Section 4.4.1. In (5.37), the inner problem is a minimization problem in the vector variable $\mathbf{s}$ parameterized by R_Σ; whereas, in (5.39), the inner problem is a max-min problem in the vector variables $\mathbf{l}$ and $\mathbf{s}$, which is also parameterized by R_Σ.

For both penalty and augmented Lagrangian formulations, we use $\delta_e = 10^3$. For the penalty formulation, we use increasingly larger values of δ. Starting from $\delta = 10^3$ and $\mathbf{s} = \mathbf{s}_0$, we solve the inner problem using a standard Newton-Raphson method with a unidirectional search. Then, we increase δ and solve again the inner problem starting from the solution of the previous problem. We repeat this process until $\delta = \delta_f$, where δ_f is large enough so that the constraint $c(\mathbf{F}) = 0$ is satisfied to within a small error. The dependence

of this error on δ_f is discussed below in the presentation of Figure 16. In this formulation, the numerical approximation of the Lagrange multiplier λ is obtained in a post-processing calculation and is given by $\lambda = -\delta\, c(\mathbf{I} + \nabla \mathbf{u}_h^\delta)$, where $\mathbf{u}_h^\delta$ is the finite element solution $\mathbf{u}_h$ corresponding to δ.

For the augmented Lagrangian formulation, we use a fixed value, $\delta = \delta_f$, where, again, δ_f is large enough so that the constraint $c(\mathbf{F}) = 0$ is satisfied to within a small error. As above, the dependence of this error on δ_f is discussed below in the presentation of Figure 16. In addition, λ_h is constant by parts, which means that m_λ coincides with the number of mesh elements used in the discretization. Starting from $l_1 = l_2 = ... = l_{m_\lambda} = 0$ and $\mathbf{s} = \mathbf{s}_0$, we solve the inner minimization problem using a standard Newton-Raphson method with a unidirectional search as explained in Section 4.4.1. Then, we update l_i, $i = 1, 2, 3, ..., m_\lambda$, as explained below and solve again the inner minimization problem starting from the solution of the previous problem. We repeat this process until the L_2-norm of the update of λ_h is lower than 10^{-3}. We update l_i, $i = 1, 2, 3, ..., m_\lambda$, using the recursive formula

$$l_i^{(k+1)} = l_i^{(k)} - \delta\, c_i^{(k)}\,, \tag{5.40}$$

where the superscript denotes an iteration of the inner maximization problem, $c_i^{(k)} = c(\mathbf{I} + \nabla \mathbf{u}_h)$, and $\nabla \mathbf{u}_h$ is evaluated at the center of the i-th mesh element in the k-th iteration.

5.3.2 Numerical results

We use the numerical procedure presented in Section 5.3.1 to determine approximate solutions of the constrained disk MP. We use the same geometrical, material, and kinematical parameters of Section 5.2. Here, we fix the pressure at the value $p = 0.1$, which is about ten times the critical value $p = 0.010161$ shown in Figure 13. Recall from Section 5.2 that, above this critical value, the local injectivity constraint becomes active near the inner radius of the disk. We compare our results with the corresponding results obtained in the context of the constrained linear theory, which is given by Remark 4. Recall from the discussion of Table 1 that, in the linear case, the pressure above which the local injectivity constraint becomes active near the inner radius of the disk is $\bar{p}_{\text{lin}} = 0.0671$. We choose $p = 0.1 > \bar{p}_{\text{lin}}$ so that in both nonlinear and linear cases the local injectivity constraint is active near the center of the disk. Although it is not shown here, we have also considered $p \in (0.010161, 0.1)$ and verified that the corresponding solution has the same qualitative behavior of the solution corresponding to $p = 0.1$.

We use $[0.9\, R_i, 0.02\, R_e]$ as the initial search interval of the golden section search. We also use non-uniform meshes parameterized by $q \in \mathbb{N}$, which was introduced in Section 4.4. We use Lagrange finite elements of degree $d = 1, 2, 3, ...$ in the approximation of the displacement field $\mathbf{u}_h$. The initial guess used in the numerical procedure is $\mathbf{s}_0 = \mathbf{0}$, which corresponds to the undistorted reference configuration.

In Figure 14, we show u_r (top left), ν (top right), $\det \mathbf{F}$ (bottom left), and λ (bottom right) versus the radius R in a neighborhood of the inner surface of the disk. The colored lines correspond to approximate solutions of the nonlinear disk problem using the augmented Lagrangian formulation with increasing mesh refinements, $\delta = 10^4$, and $d = 1$. These colored lines are almost indistinguishable, which indicates the convergence of the numerical results. Using $d = 2$ and the sequence $\delta = 10^3, 10^4, 10^5$, the numerical results obtained with the penalty formulation are very similar to those shown in Figure 14. Later in this section, we present a comparison of results obtained with both formulations. The black solid lines correspond to the exact solution of the disk problem in the context of the constrained linear theory, which is given by (5.10)-(5.11) in $\mathcal{B}_=$ and (5.15)-(5.16) in $\mathcal{B}_>$. The black dotted line in the graph of λ corresponds to the analytical expression of λ, given by (5.21), where K is calculated using the numerical approximations of R_Σ and $\lambda(R_\Sigma)$ obtained with the most refined mesh. We see from this graph that the numerical approximations of λ converge to its analytical expression.

We see from Figure 14.a that the radial displacement u_r is continuous, but not smooth, and that the colored lines are nearly parallel to the black solid line for $R > R_\Sigma$. In fact, this behavior is observed up to the outer surface of the disk, $R = 1$, where the difference between the displacements is approximately 12%. This seems to indicate that a localized behavior of the solution affects its global behavior.

We see from Figure 14.b that the radial stretch ν has a jump discontinuity at $R = R_\Sigma$. An analogous discontinuity was observed in the case of the unconstrained disk MP, as shown in Figure 11. There, however, the discontinuity is related to $\det \mathbf{F} < 0$, which is not admissible. We see also that the black and the colored lines are indistinguishable near the inner radius of the disk, differ significantly in an interval around the discontinuity, and become indistinguishable again as we move towards the outer surface of the disk.

We see from above that the disk is considerably more deformed in $\mathcal{B}_=$ than it is in $\mathcal{B}_>$. For radially fiber-reinforced materials, this indicates that, near the inner surface of the disk and for $p > \bar{p}$, the fibers fail by kinking, since the surface of discontinuity of the deformation gradient is normal to the fiber direction. See, for instance, Merodio and Ogden (2002) and El Hamdaoui, Merodio and Ogden (2020).

Next, observe from Figures 14.c and 14.d that the local injectivity constraint is active in the intervals $(R_i, R_\Sigma^{\text{lin}})$ and (R_i, R_Σ), where $R_\Sigma^{\text{lin}} \approx 0.002$ in the constrained linear theory and $R_\Sigma \approx 0.010$ in the constrained nonlinear theory. In addition, in $(R_i, R_\Sigma^{\text{lin}})$, u_r and, consequently, ν of both theories coincide, as expected from Section 5.2.1.

Recall from Section 3.6 that (3.115) and (3.116) are necessary conditions that the deformation field must satisfy to be a minimizer of the energy functional. To verify these conditions in our case, we show the trajectory of solution represented by the blue solid line in Figure 15 together with the curve $\mathcal{C}_\Sigma$ represented by the black dotted line. The curve

Figure 14 – Radial displacement u_r, radial stretch ν, determinant of the deformation gradient $\det \mathbf{F}$, and Lagrange multiplier λ versus the radius R.

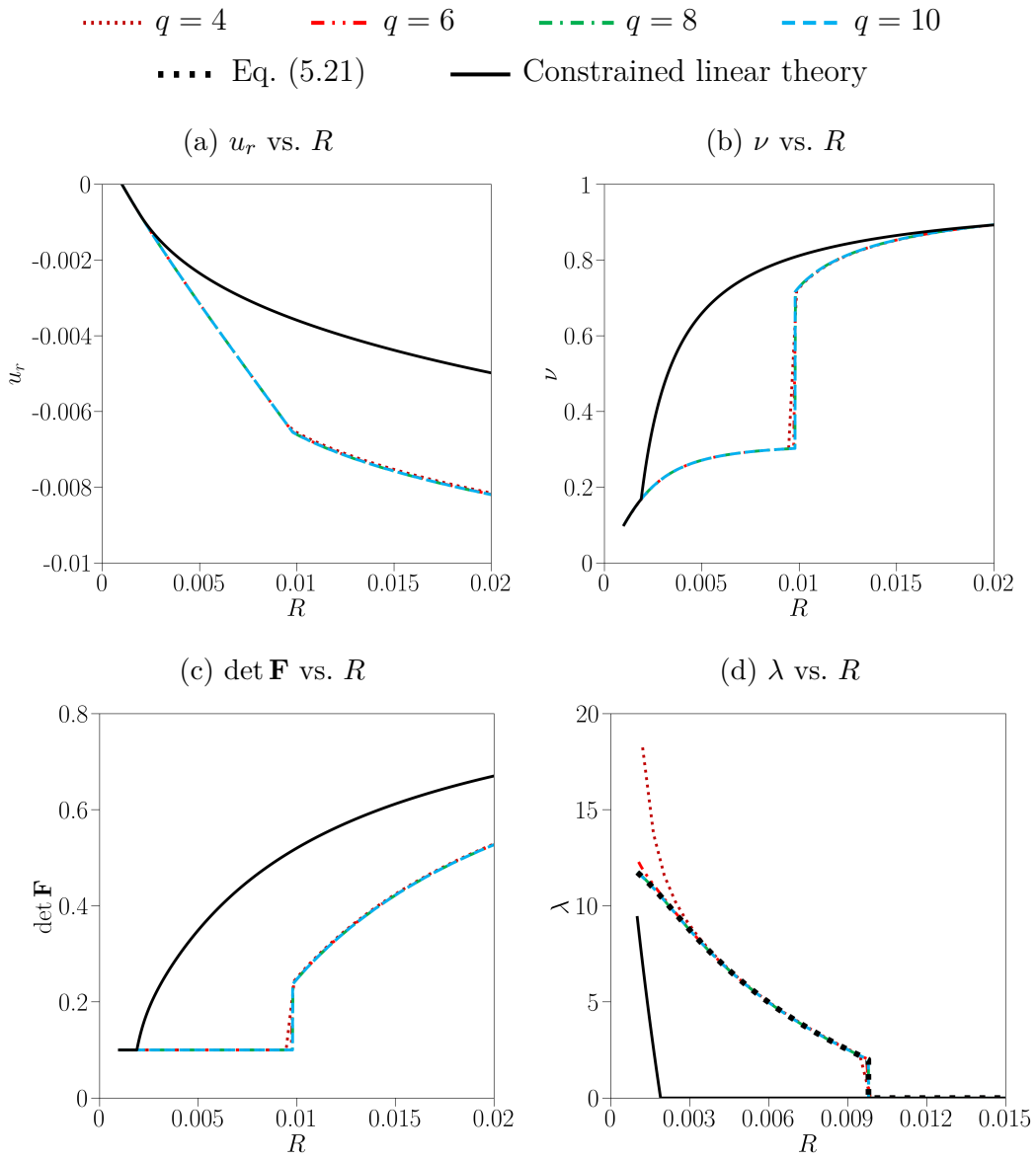

Source: The author.

Figure 15 – Curve $(\tau(R), P^a_{rr}(R))$ for $R \in [R_i, R_e]$ and $p = 0.1$ obtained from the approximate solutions of both the constrained disk MP using $q = 10$ and the constrained disk BVP using $\delta\xi = 10^{-3}$.

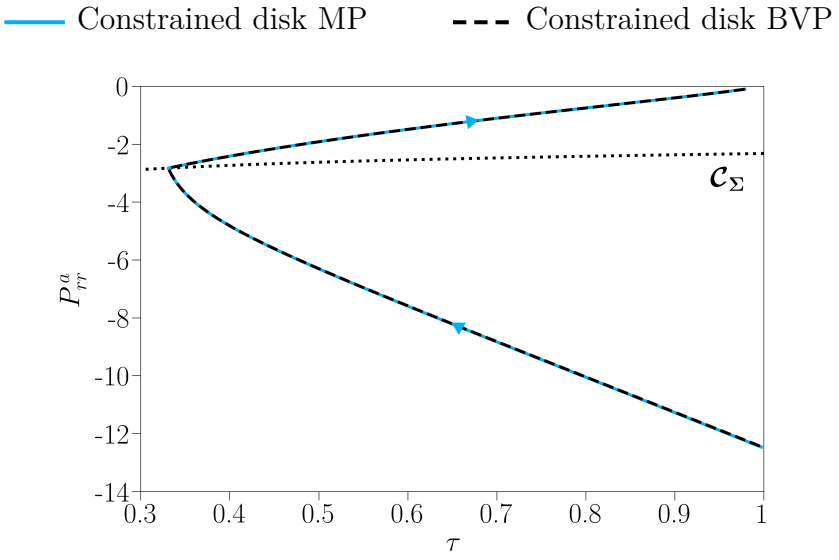

Source: The author.

$\mathcal{C}_\Sigma$ is obtained from (5.33), which defines the set of points $(\tau(R), P^a_{rr}(R))$ satisfying the dissipation-free condition (3.116). Observe from this figure that the trajectory of solution is continuous and changes direction abruptly at the intersection with the curve $\mathcal{C}_\Sigma$. The above conditions are, therefore, satisfied. For comparison purposes, we also plot the the trajectory of solution of the constrained disk BVP as a black dashed line. Both the blue solid and the black dashed lines are almost indistinguishable from each other.

We now focus on the comparison between the penalty and the augmented Lagrangian formulations. For this, we investigate how accurately the constraint $\det \mathbf{F} = \varepsilon$ in $\mathcal{B}_=$ is imposed when we use different meshes, by varying the parameter q, and finite element approximations, by varying the parameter d. We also study the influence of the penalty parameter δ on the penalty and the augmented Lagrangian formulations. The results presented below were obtained using the same pressure, disk geometry, and material parameters used in the previous numerical example.

We define the error $e \triangleq \sqrt{\int_{\mathcal{B}_=} (\det \mathbf{F} - \varepsilon)^2 \, \mathrm{d}\mathbf{x}}$ and, in Figure 16, we plot $\log_{10} e$ versus $\log_{10} \delta_f$, where δ_f is the final value of δ. Recall from Section 5.3.1 that, in the augmented Lagrangian formulation, δ is fixed and equal to δ_f, and that, in the penalty formulation, δ increases from $\delta = 10^3$ to $\delta = \delta_f$. The two graphs on the top part of the figure refer to results obtained with $d = 1$ and increasing values of q. The two graphs on the bottom part refer to results obtained with $q = 6$ and increasing values of d. The graphs on the left and right sides refer to, respectively, the penalty and the augmented

Lagrangian formulations. From the top left graph, we see that e decreases as δ_f increases until it reaches an asymptotic value that decreases as q increases. From the top right graph, we see that e decreases as q increases, independently of the value of δ_f.

Next, we see from the bottom left graph of Figure 16 that, for the penalty formulation, the error e decreases as δ_f increases until it reaches an asymptotic value that decreases as d increases. From the bottom right graph, we see that the augmented Lagrangian formulation yields a similar behavior. The main difference in this case is that the asymptotic value is reached with lower values of δ_f.

For large enough penalty parameters, we see from Figure 16 that, in both formulations, an increase of two units in q, which approximately quadruplicates the number of degrees of freedom, reduces $\log_{10} e$ in approximately 0.6 units. On the other hand, an increase of one unit in d, which less than duplicates the number of degrees of freedom, reduces $\log_{10} e$ in approximately 2 units. Therefore, our results indicate that, to reduce the error e, it is preferable to increase the degree of the finite element approximation than to increase the number of mesh elements.

In Figures 17 and 18 we consider the cases $\varepsilon \to 0$ and $R_i \to 0$, respectively. In Figure 17, we plot λ versus the radius R for $\varepsilon = 10^{-1}, 10^{-2}, 10^{-3}, 10^{-5}, 10^{-7}$, and a fixed inner radius $R_i = 0.001$. We see from this figure that the curves tend to a limit curve as $\varepsilon \to 0$; in fact, the curves corresponding to $\varepsilon = 10^{-5}$ and $\varepsilon = 10^{-7}$ are indistinguishable. In Figure 18, we show $\log_{10} \lambda$ versus the radius R for $R_i = 10^{-5}, 4\times10^{-5}, 16\times10^{-5}, 64\times10^{-5}, 256\times10^{-5}$, and a fixed parameter $\varepsilon = 10^{-7}$. We see that, as R_i decreases, λ increases with no indication of convergence to some limit curve. In addition, for $R_i = 10^{-5}, 4\times10^{-5}, 16\times10^{-5}$, λ sharply increases as we approach $R = R_i$. These results are in good agreement with the results presented in Section 5.2, below equation (5.29), where we have seen that λ remains finite in the case $R_i > 0$ and $\varepsilon \to 0$, but is unbounded in the case $R_i = 0$ and $\varepsilon \to 0$.

Next, we compare numerical results obtained with both the constrained minimization theory and the classical nonlinear elasticity theory. For this, we compare solutions of the disk MP in the case of the orthotropic and compressible Mooney-Rivlin material, defined in Section 4.1, with solutions of the constrained disk MP, which was defined in Section 5.1 and uses the orthotropic St Venant-Kirchhoff material as its material model.

In Figure 19, we show the radial displacement u_r (top left), the radial stretch ν (top right), the determinant of the deformation gradient $\det \mathbf{F} = \nu\,\tau$ (bottom left), and the radial stress (bottom right) versus the radius R in a neighborhood of the inner surface of the disk. Regarding the radial stress, we show P^a_{rr}, given by (5.3), for the St Venant-Kirchhoff model and P_{rr}, given by (4.8), for the Mooney-Rivlin model. The solid lines correspond to results obtained with the Mooney-Rivlin (MR) material for different values of c_{33}. The dashed lines correspond to results obtained with the St Venant-Kirchhoff (StVK) material for different values of ε. Recall from (4.49) that the energy functional

Figure 16 – Base 10 logarithm of the error e versus base 10 logarithm of the final penalty parameters δ_f.

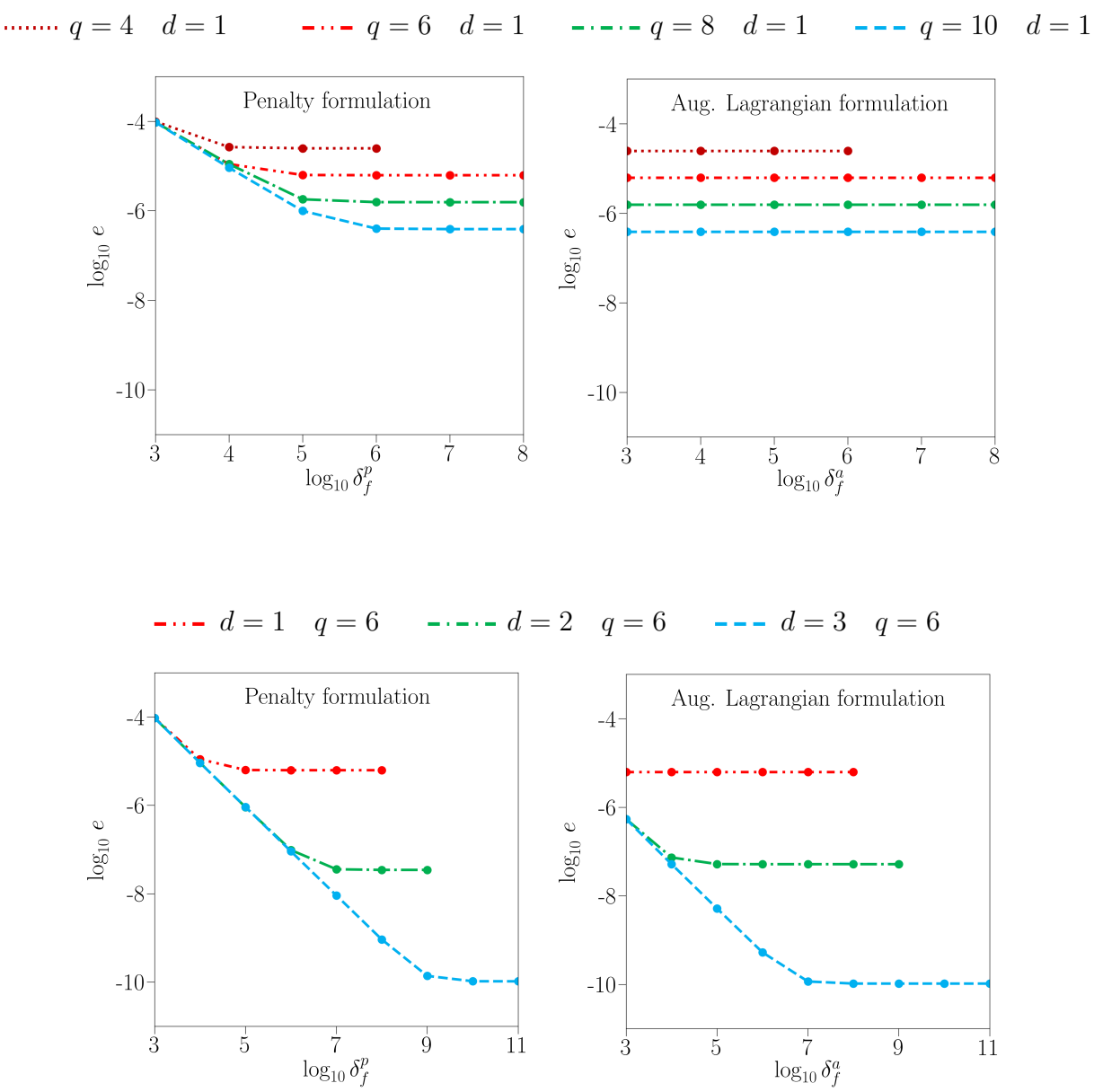

Source: The author.

Figure 17 – Lagrange multiplier field λ versus R for $R_i = 0.001$ and different values of ε.

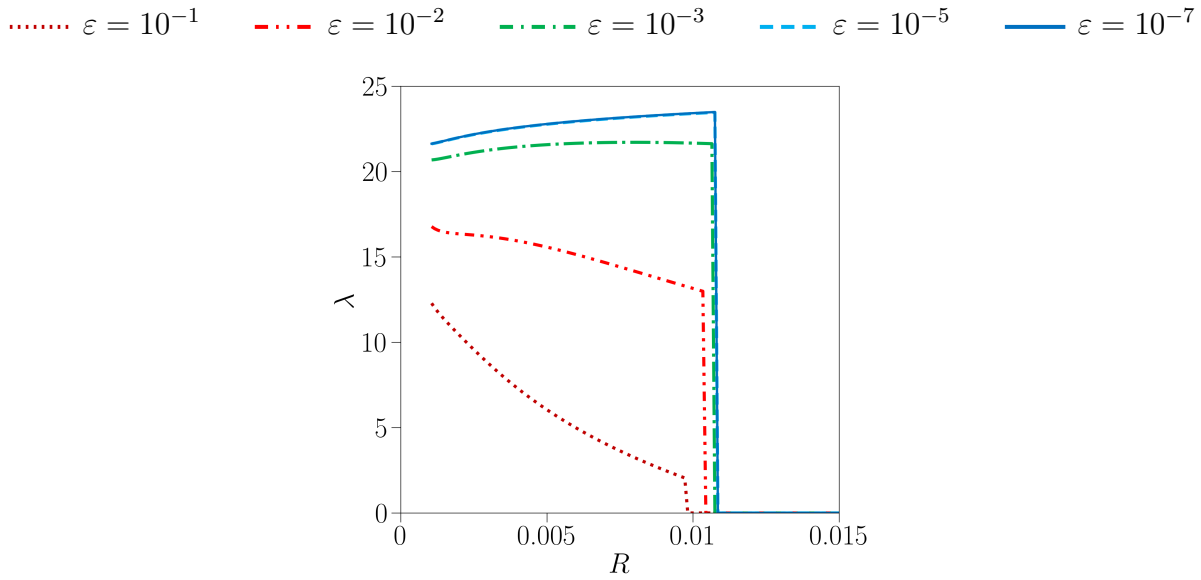

Source: The author.

Figure 18 – Lagrange multiplier field λ versus R for $\varepsilon = 10^{-7}$ and different values of R_i.

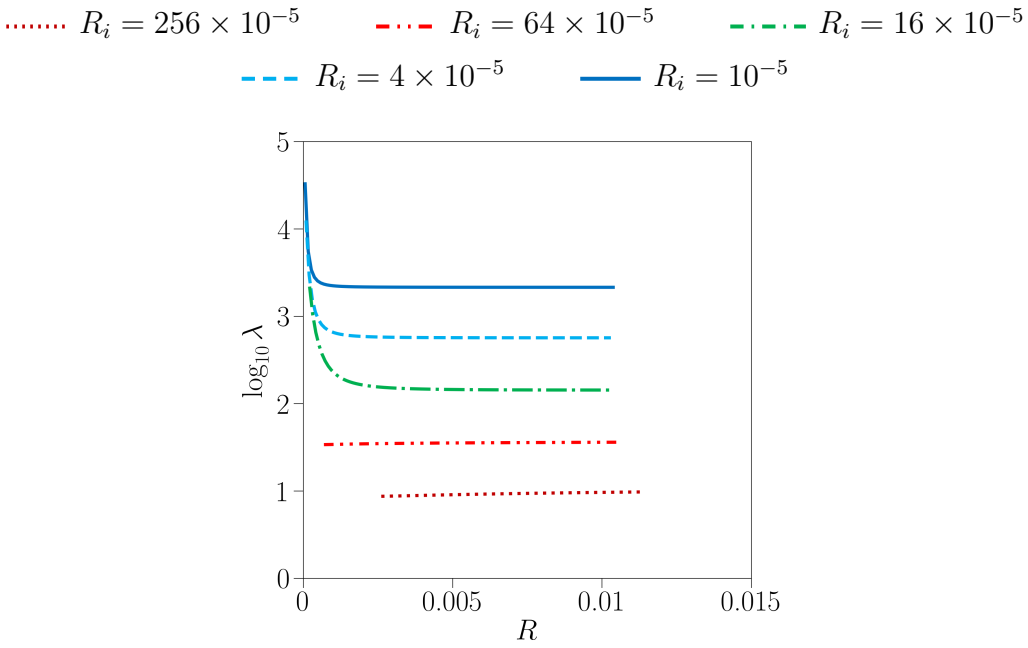

Source: The author.

of the Mooney-Rivlin material depends on the elastic constant c_{33}, whereas the energy of the St Venant-Kirchhoff material, given by (4.48), does not. On the other hand, in the constrained minimization theory, the results depend on the constraint parameter ε. We see from Figure 19 that the results obtained with both materials have similarities. For instance, as we move away from the inner radius, $\det \mathbf{F}$ remains either constant or approximately constant, increases sharply, and then increases moderately. In addition, as c_{33} and ε decrease, the results obtained with both materials become very similar. In particular, the case MR $c_{33} = c_{22}/100$ is almost indistinguishable from the case StVK $\varepsilon = 0.001$. These results indicate that the constrained minimization theory prevents self-intersection from occurring in a way which is consistent with others classical nonlinear elastic models.

Figure 19 – Radial displacement u_r, radial stretch ν, determinant of the deformation gradient $\det \mathbf{F}$, and radial stress versus the radius R for different values of c_{33} and ε.

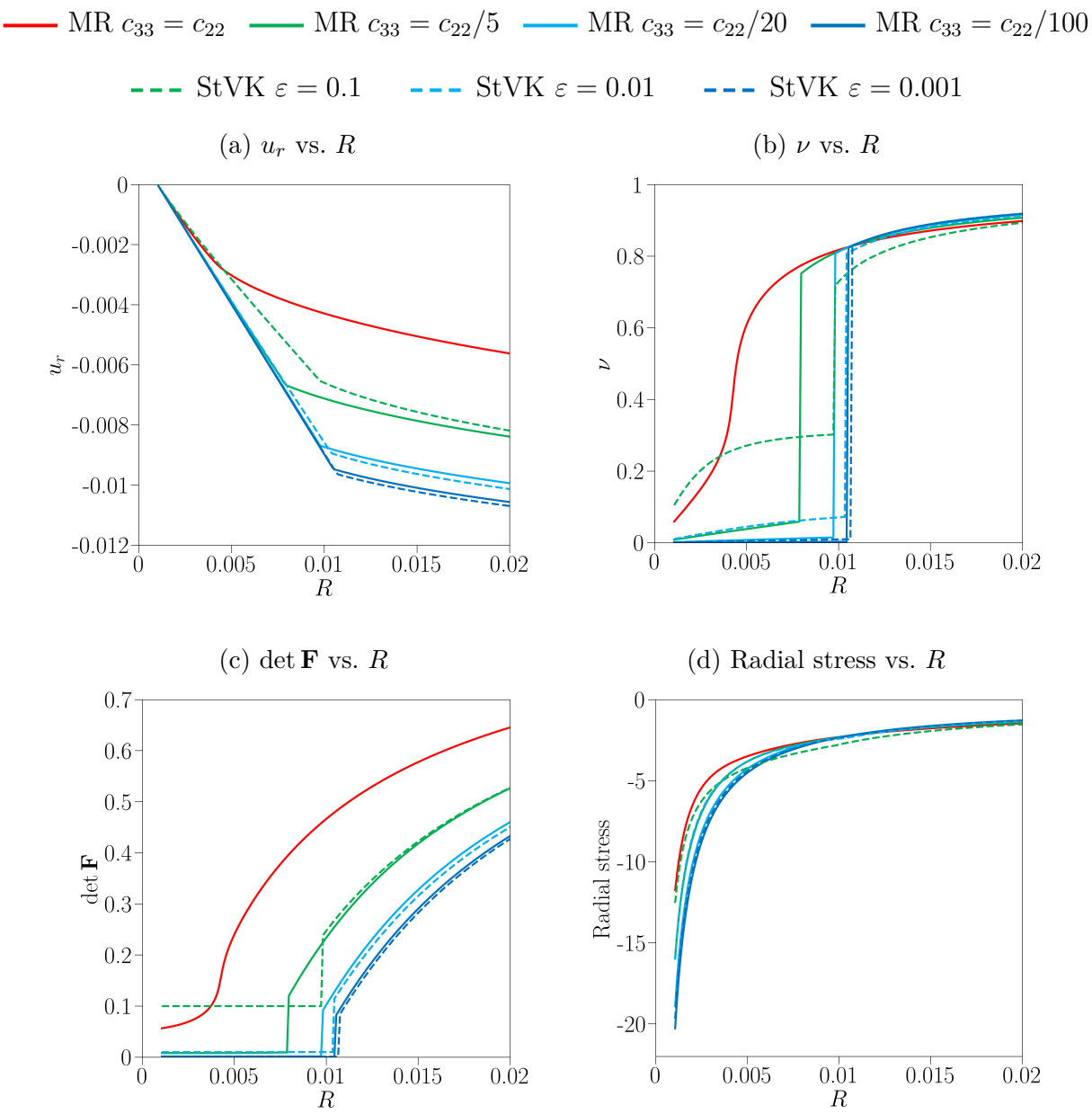

Source: The author.

6 FINAL CONSIDERATIONS

This work proposes a constrained minimization theory in nonlinear elasticity, which represents an extension of the constrained minimization theory of Fosdick and Royer-Carfagni (2001), to impose the local injectivity condition, $\det \mathbf{F} > 0$. This condition is associated to the physical requirement that matter cannot penetrate itself. Our interest is on the investigation of equilibrium problems of hyperelastic solids satisfying the injectivity condition. For this, we considered the problem of minimizing the total potential energy of a hyperelastic solid subject to the injectivity condition. We derived necessary conditions that a minimizer must satisfy, which include traction continuity and dissipation-free conditions on surfaces of discontinuity of the deformation gradient. These conditions, which are given by (3.111), (3.112), (3.115), and (3.116), are the nonlinear counterparts of the conditions obtained by Fosdick and Royer-Carfagni (2001).

We applied this minimization theory in the investigation of the problem of an orthotropic annular disk that is fixed on its inner surface of radius R_i and is compressed by a constant pressure p on the deformed configuration of its outer surface of radius R_e. The disk is made of an orthotropic St Venant-Kirchhoff material. If no injectivity condition is imposed and if the applied pressure is greater than a certain critical value $\bar{p}$, we found an equilibrium solution that predicts both self-intersection in a neighborhood of the inner surface of the disk and a jump in the deformation gradient across an interior surface of the disk. This discontinuity is due to the failure of ellipticity of the equilibrium equations. Thus, $\bar{p}$ is an upper bound below which the classical linear theory is valid. In addition, we verified that $\bar{p} \to 0$ as $R_i \to 0$, which means that the solution predicts self-intersection for any value of pressure in the case of a solid disk, for which $R_i = 0$. This last behavior is also observed in the context of the classical linear elasticity theory.

By imposing the local injectivity constraint, $\det \mathbf{F} \geq \varepsilon > 0$, the solution does not predict self-intersection. The behavior of the Lagrange multiplier is qualitatively similar to its constrained linear counterpart. For $R_i > 0$, the multiplier remains finite. For $R_i = 0$, both λ and its constrained linear counterpart have a log-singularity at the center of the disk for $\varepsilon > 0$ and are unbounded in a neighborhood of this center for $\varepsilon \to 0$. These conclusions were found analytically and confirmed numerically. In addition, we compared the solutions of both the constrained nonlinear theory and the classical nonlinear theory. For the latter, we used an orthotropic and compressible Mooney-Rivlin material and obtained solutions which are in very good agreement with those obtained with the constrained nonlinear theory.

We used two different numerical approaches. The first approach consists in using the Euler-Lagrange equations of the associated minimization problem to formulate a boundary

value problem. The problem was then solved numerically using a phase-plane technique. This technique is very useful in providing both qualitative and quantitative insights of solution candidates; especially, when these candidates are not smooth. In particular, it allowed us to formulate an initial value problem to calculate $\bar{p}$. The second approach consists in using the finite element method to formulate a bi-level minimization problem, in which the independent variables are the degrees of freedom of the displacement field and the position of the surface of discontinuity of the deformation gradient. Standard minimization techniques are then used to search for a minimizer of this minimization problem. This minimizer satisfies the necessary conditions found previously, which include the traction continuity and dissipation-free condition given by (3.115) and (3.116), respectively. In addition, in this second approach, we imposed the local injectivity constraint using both a penalty and an augmented Lagrangian formulation. To obtain similar results, the former requires a more refined discretization by either refining the mesh or by increasing the order of the finite element. On the other hand, the latter requires a discretization of the Lagrange multiplier field, which introduces additional degrees of freedom.

For future investigations, it would be interesting to investigate the existence of a possible secondary solution of the disk problem in the context of the constrained nonlinear theory. Such a solution could correspond to a deformation field with both radial and tangential components depending on both radius and azimuth. One of the challenges is the fact that the discontinuity of the deformation gradient might not be only due to the radial stretch ν, but also due to new components of the deformation gradient associated with the tangential displacement. In addition, for the radially symmetric deformation field considered in this work, the discontinuity occurs only on the interface Σ between the regions where the local injectivity constraint is active and inactive; this could not be true for more general deformations fields.

It would also be interesting to apply the constrained linear and nonlinear theories to more complex problems such as those involving cracks and corners. In the classical linear elasticity theory, the solutions of these problems may predict oscillatory behaviors that are associated with self-intersection. In the context of the classical nonlinear elasticity theory, the solution may require some constraints on the values of the elastic constants to avoid self-intersection; see, for instance, Aguiar and Fosdick (2014) and the references cited therein. These problems may have complex geometries that require new strategies to find the solution. The theory of free boundary problems, which are often formulated as variational inequalities, may be particularly useful since it concerns problems of determining field variables, such as the displacement field, and geometric variables, such as the contour of the active region $\mathcal{B}_{=}$. See, for instance, Kinderlehrer and Stampacchia (1980) for classical aspects of the theory and Chen, Shahgholian and Vazquez (2015) for some recent developments in the area.

REFERENCES

ABEYARATNE, R. C. Discontinuous deformation gradients in the finite twisting of an incompressible elastic tube. **Journal of Elasticity**, v. 11, n. 1, p. 43–80, Jan. 1981. ISSN 0374-3535.

ABEYARATNE, R. C. An admissibility condition for equilibrium shocks in finite elasticity. **Journal of Elasticity**, v. 13, n. 2, p. 175–184, July 1983. ISSN 0374-3535.

ABEYARATNE, R. C.; KNOWLES, J. K. **Evolution of phase transitions**. New York: Cambridge University Press, 2006. ISBN 9780521661478.

AGUIAR, A. R. Local and global injective solution of the rotationally symmetric sphere problem. **Journal of Elasticity**, v. 84, n. 2, p. 99–129, 2006. ISSN 0374-3535.

AGUIAR, A. R. Strong ellipticity conditions for orthotropic bodies in finite plane strain. **Journal of Elasticity**, v. 134, n. 2, p. 219–234, Feb. 2019. ISSN 0374-3535.

AGUIAR, A. R.; FOSDICK, R. L. On the corner behavior of a non-linear elastic wedge under mixed boundary conditions. **International Journal of Non-Linear Mechanics**, v. 66, p. 111–125, Nov. 2014. ISSN 0020-7462.

AGUIAR, A. R.; FOSDICK, R. L.; SANCHEZ, J. A study of penalty formulations used in the numerical approximation of a radially symmetric elasticity problem. **Journal of Mechanics of Materials and Structures**, v. 3, n. 8, 2008. ISSN 1559-3959.

AGUIAR, A. R.; ROCHA, L. A. On the existence of rotationally symmetric solution of a constrained minimization problem of elasticity. **Journal of Elasticity**, v. 147, n. 1-2, p. 1–32, Dec. 2021. ISSN 0374-3535.

ANTMAN, S. S. **Nonlinear problems of elasticity**. New York: Springer-Verlag, 2005. (Applied Mathematical Sciences, v. 107). ISBN 0-387-20880-1.

ANTMAN, S. S.; NEGRÓN-MARRERO, P. V. The remarkable nature of radially symmetric equilibrium states of aeolotropic nonlinearly elastic bodies. **Journal of Elasticity**, v. 18, n. 2, p. 131–164, 1987. ISSN 0374-3535.

ARNDT, D. *et al.* The deal.II library, version 9.1. **Journal of Numerical Mathematics**, v. 27, n. 4, p. 203–213, June 2019. ISSN 1570-2820.

ARNDT, M. *et al.* Martensitic transformation in NiMnGa single crystals: Numerical simulation and experiments. **International Journal of Plasticity**, v. 22, n. 10, p. 1943–1961, Oct. 2006. ISSN 0749-6419.

BAEK, S.; PENCE, T. J. Emergence and disappearance of load induced fiber kinking surfaces in transversely isotropic hyperelastic materials. **Zeitschrift für angewandte Mathematik und Physik**, v. 61, n. 4, p. 745–772, Aug. 2010. ISSN 0044-2275.

BALL, J. M. Convexity conditions and existence theorems in nonlinear elasticity. **Archive for Rational Mechanics and Analysis**, v. 63, n. 4, p. 337–403, Dec. 1976. ISSN 0003-9527.

BATRA, R. C. Comparison of results from four linear constitutive relations in isotropic finite elasticity. **International Journal of Non-Linear Mechanics**, v. 36, n. 3, p. 421–432, May 2001. ISSN 0020-7462.

BONET, J.; BURTON, A. J. A simple orthotropic, transversely isotropic hyperelastic constitutive equation for large strain computations. **Computer Methods in Applied Mechanics and Engineering**, v. 162, n. 1-4, p. 151–164, Aug. 1998. ISSN 0045-7825.

CHEN, G. Q.; SHAHGHOLIAN, H.; VAZQUEZ, J. L. Free boundary problems: the forefront of current and future developments. **Proceedings of the Royal Society A**: Mathematical, Physical and Engineering Sciences, v. 373, p. 20140285, 2015. ISSN 1471-2946.

CHRISTENSEN, R. M. Properties of carbon fibers. **Journal of the Mechanics and Physics of Solids**, v. 42, n. 4, p. 681–695, 1994. ISSN 1873-4782.

CIARLET, P. G. **Mathematical elasticity, volume I**: three-dimensional elasticity. Amsterdam: North-Holand, 1988. ISBN 0444702598.

DANIEL, I. M.; ISHAI, O. **Engineering mechanics of composite materials**. 2nd ed. New York: Oxford University Press, 2006. (Engineering mechanics of composite materials, v. 13). ISBN 9780195150971.

EIK, M.; PUTTONEN, J.; HERRMANN, H. An orthotropic material model for steel fibre reinforced concrete based on the orientation distribution of fibres. **Composite Structures**, v. 121, p. 324–336, Mar. 2015. ISSN 0263-8223.

EL HAMDAOUI, M.; MERODIO, J.; OGDEN, R. W. Loss of ellipticity in the combined helical, axial and radial elastic deformations of a fibre-reinforced circular cylindrical tube. **International Journal of Solids and Structures**, v. 63, p. 99–108, June 2015. ISSN 0020-7683.

EL HAMDAOUI, M.; MERODIO, J.; OGDEN, R. W. Deformation induced loss of ellipticity in an anisotropic circular cylindrical tube. **Journal of Engineering Mathematics**, v. 109, n. 1, p. 31–45, Apr. 2018. ISSN 0022-0833.

EL HAMDAOUI, M.; MERODIO, J.; OGDEN, R. W. Two-phase piecewise homogeneous plane deformations of a fibre-reinforced neo-Hookean material with application to fibre kinking and splitting. **Journal of the Mechanics and Physics of Solids**, v. 143, p. 104091, Oct. 2020. ISSN 0022-5096.

ERICKSEN, J. L. Equilibrium of bars. **Journal of Elasticity**, v. 5, n. 3-4, p. 191–201, Nov. 1975. ISSN 0374-3535.

FOREST PRODUCTS LABORATORY. **Wood handbook**: wood as an engineering material. Madison: U. S. Department of Agriculture, 2010. 508 p.

FOSDICK, R. L.; FREDDI, F.; ROYER-CARFAGNI, G. Bifurcation instability in linear elasticity with the constraint of local injectivity. **Journal of Elasticity**, v. 90, n. 1, p. 99–126, 2008. ISSN 0374-3535.

FOSDICK, R. L.; MACSITHIGH, G. Helical shear of an elastic, circular tube with a non-convex stored energy. *In*: DAFERMOS, C. M.; JOSEPH, D. D.; LESLIE, F. M. **The breadth and depth of continuum mechanics**. Berlin: Springer, 1986. p. 177–199.

FOSDICK, R. L.; ROYER-CARFAGNI, G. The constraint of local injectivity in linear elasticity theory. **Proceedings of the Royal Society A**: Mathematical, Physical and Engineering Sciences, v. 457, n. 2013, p. 2167–2187, 2001.

FROLI, M.; ROYER-CARFAGNI, G. Discontinuous deformation of tensile steel bars: Experimental results. **Journal of Engineering Mechanics**, v. 125, n. 11, p. 1243–1250, Nov. 1999. ISSN 0733-9399.

FROLI, M.; ROYER-CARFAGNI, G. A mechanical model for the elastic–plastic behavior of metallic bars. **International Journal of Solids and Structures**, v. 37, n. 29, p. 3901–3918, July 2000. ISSN 0020-7683.

GELFAND, I. M.; FOMIN, S. V. **Calculus of variations**. New Jersey: Prentice-Hall, 1963. ISBN 9780486414485.

GURTIN, M. E. The linear theory of elasticity. *In*: TRUESDELL, C. (ed.). **Linear theories of elasticity and thermoelasticity**. Berlin: Springer, 1973. p. 1–295.

GURTIN, M. E. **An introduction to continuum mechanics**. New York: Elsevier Science, 1982. (Mathematics in science and engineering, v. 158). ISBN 9780080918495.

GURTIN, M. E. Two-phase deformations of elastic solids. *In*: DAFERMOS, C. M.; JOSEPH, D. D.; LESLIE, F. M. **The breadth and depth of continuum mechanics**. Berlin: Springer, 1986. p. 147–175.

GURTIN, M. E. The dynamics of solid-solid phase transitions 1. Coherent interfaces. **Archive for Rational Mechanics and Analysis**, v. 123, n. 4, p. 305–335, 1993. ISSN 0003-9527.

HUANG, X. Fabrication and properties of carbon fibers. **Materials**, v. 2, n. 4, p. 2369–2403, Dec. 2009. ISSN 1996-1944.

ITSKOV, M.; AKSEL, N. A class of orthotropic and transversely isotropic hyperelastic constitutive models based on a polyconvex strain energy function. **International Journal of Solids and Structures**, v. 41, n. 14, p. 3833–3848, July 2004. ISSN 0020-7683.

KINDERLEHRER, D.; STAMPACCHIA, G. **An Introduction to Variational Inequalities and Their Applications**. Philadelphia: Society for Industrial and Applied Mathematics, 1980. (Classics in Applied Mathematics). ISBN 9780898719451.

KIRK, D. E. **Optimal control theory**: an introduction. Mineola: Dover Publications, 2004. ISBN 9780486434841.

KNOWLES, J. K. On the dissipation associated with equilibrium shocks in finite elasticity. **Journal of Elasticity**, v. 9, n. 2, p. 131–158, Apr. 1979. ISSN 0374-3535.

KNOWLES, J. K.; STERNBERG, E. On the failure of ellipticity and the emergence of discontinuous deformation gradients in plane finite elastostatics. **Journal of Elasticity**, v. 8, n. 4, p. 329–379, Oct. 1978. ISSN 0374-3535.

LEKHNITSKII, S. G. **Anisotropic plates**. New York: Gordon & Breach, 1968. ISBN 9782881242007.

LEWANDOWSKI, M. J.; STUPKIEWICZ, S. Size effects in wedge indentation predicted by a gradient-enhanced crystal-plasticity model. **International Journal of Plasticity**, v. 109, p. 54–78, Oct. 2018. ISSN 0749-6419.

LUENBERGER, D. G.; YE, Y. **Linear and nonlinear programming**. New York: Springer, 2008. (International Series in Operations Research & Management Science, v. 228). ISBN 978-0-387-74502-2.

MERODIO, J.; OGDEN, R. W. Material instabilities in fiber-reinforced nonlinearly elastic solids under plane deformation. **Archive of mechanics**, v. 54, n. 5-6, p. 525–552, 2002. ISSN 2083-8514.

MERODIO, J.; OGDEN, R. W. Remarks on instabilities and ellipticity for a fiber-reinforced compressible nonlinearly elastic solid under plane deformation. **Quarterly of Applied Mathematics**, v. 63, n. 2, p. 325–333, Feb. 2005. ISSN 0033-569X.

MERODIO, J.; SACCOMANDI, G.; SGURA, I. The rectilinear shear of fiber-reinforced incompressible non-linearly elastic solids. **International Journal of Non-Linear Mechanics**, v. 42, n. 2, p. 342–354, Mar. 2007. ISSN 0020-7462.

MURPHY, J. Transversely isotropic biological, soft tissue must be modelled using both anisotropic invariants. **European Journal of Mechanics**: A/Solids, v. 42, p. 90–96, Nov. 2013. ISSN 09977538.

OBEIDAT, K. *et al.* Numerical analysis of elastic problems with injectivity constraints. *In*: EUROPEAN CONFERENCE ON COMPUTATIONAL MECHANICS, 2001. **Proceedings** [...]. Cracow: Fundacja Zdrowia Publicznego "Vesalius", 2001.

PONTRYAGIN, L. S. **Ordinary differential equations**. Reading: Addison-Wesley, 1962. ISBN 9781483156491.

RAIBLE, T. *et al.* Development of a wrinkling algorithm for orthotropic membrane materials. **Computer Methods in Applied Mechanics and Engineering**, v. 194, n. 21-24, p. 2550–2568, June 2005. ISSN 0045-7825.

SCHRÖDER, J. Anisotropie polyconvex energies. *In*: SCHRÖDER J; NEFF, P. (eds.). **Poly-, quasi- and rank-one convexity in applied mechanics**. Vienna: Springer, 2010. (CISM International Centre for Mechanical Sciences, v. 516). p. 53–105.

SCHRÖDER, J.; NEFF, P. Invariant formulation of hyperelastic transverse isotropy based on polyconvex free energy functions. **International Journal of Solids and Structures**, v. 40, n. 2, p. 401–445, Jan. 2003. ISSN 0020-7683.

SILHAVY, M. **The Mechanics and Thermodynamics of Continuous Media**. Berlin: Springer-Verlag, 1997. (Theoretical and Mathematical Physics). ISBN 9783662033890.

SOKOLNIKOFF, I. S. **Mathematical theory of elasticity**. 2nd ed. New York: McGraw-Hill, 1956. ISBN 9780070596290.

SPENCER, A. J. M. Constitutive theory for strongly anisotropic solids. *In*: SPENCER, A. J. M. (ed.). **Continuum theory of the mechanics of fibre-reinforced composites**. Vienna: Springer, 1984, (CISM International Centre for Mechanical Sciences, v. 282). p. 1–32.

STEPANOV, A. B.; ANTMAN, S. S. Radially symmetric steady states of nonlinearly elastic plates and shells. **Journal of Elasticity**, v. 124, n. 2, p. 243–278, Aug. 2016. ISSN 0374-3535.

TING, T. C. T. Remarkable nature of radially symmetric deformation of spherically uniform linear anisotropic elastic solids. **Journal of Elasticity**, v. 53, n. 1, p. 47–64, 1998. ISSN 0374-3535.

TOMMASI, D. *et al.* Incompressible elastic bodies with non-convex energy under dead-load surface tractions. **Journal of Elasticity and the Physical Science of Solids**, v. 65, n. 1, p. 149–168, 2001. ISSN 1573-2681.

VU-QUOC, L.; TAN, X. Optimal solid shells for non-linear analyses of multilayer composites. I. Statics. **Computer Methods in Applied Mechanics and Engineering**, v. 192, n. 9-10, p. 975–1016, Feb. 2003. ISSN 0045-7825.

YAMASHITA, H.; JAYAKUMAR, P.; SUGIYAMA, H. Physics-based flexible tire model integrated with LuGre tire friction for transient braking and cornering analysis. **Journal of Computational and Nonlinear Dynamics**, v. 11, n. 3, p. 1–17, May 2016. ISSN 1555-1415.

APPENDIX

APPENDIX A – LINEARIZATION OF THE STRESS TENSOR

We obtain the linearization of the second Piola-Kirchhoff stress tensor $\mathbf{S}$, given by (3.59). In this appendix, all the linearizations are with respect to $\mathbf{E}$ around the reference configuration, so this statement will be omitted. We begin by linearizing some of the terms in (3.57). We use (3.32.b), (3.51), and the identities, (Gurtin, 1982),

$$\det(\mathbf{A}-\omega\,\mathbf{I}) = -\omega^3 + \operatorname{tr}\mathbf{A}\,\omega^2 - \frac{1}{2}[(\operatorname{tr}\mathbf{A})^2 - \operatorname{tr}(\mathbf{A}^2)]\,\omega + \det\mathbf{A}\,, \tag{A.1}$$

$$(\mathbf{A}+\delta\mathbf{A})^{-1} = \mathbf{A}^{-1} + \frac{\partial(\mathbf{A}^{-1})}{\partial\mathbf{A}}\,\delta\mathbf{A} + o(\delta\mathbf{A}) = \mathbf{A}^{-1} - \mathbf{A}^{-1}\,\delta\mathbf{A}\,\mathbf{A}^{-1} + o(\delta\mathbf{A})\,, \tag{A.2}$$

where $\mathbf{A}, \delta\mathbf{A} \in \text{Lin}$, to write

$$\mathbf{C}^{-1} = \mathbf{I} - 2\,\mathbf{E} + o(\mathbf{E})\,, \tag{A.3}$$

$$I_3 = 1 + 2\operatorname{tr}\mathbf{E} + o(\mathbf{E})\,, \tag{A.4}$$

$$I_3\,\mathbf{C}^{-1} = \mathbf{I} + -2\,\mathbf{E} + (2\operatorname{tr}\mathbf{E})\,\mathbf{I} + o(\mathbf{E}) \tag{A.5}$$

$$I_1\,\mathbf{I} - \mathbf{C} = 2\,\mathbf{I} + (2\operatorname{tr}\mathbf{E})\,\mathbf{I} - 2\,\mathbf{E}\,, \tag{A.6}$$

$$(\mathbf{C}\mathbf{m}_i\otimes\mathbf{m}_i + \mathbf{m}_i\otimes\mathbf{C}\mathbf{m}_i) = 2\,(\mathbf{m}_i\otimes\mathbf{m}_i + \mathbf{E}\,\mathbf{m}_i\otimes\mathbf{m}_i + \mathbf{m}_i\otimes\mathbf{E}\,\mathbf{m}_i)\,, \quad i=1,2\,. \tag{A.7}$$

Substituting (A.5)-(A.7) into (3.57) yields

$$\begin{aligned}\mathbf{S} = 2\Big\{&\mathbf{I}\left[\bar{W}_1 + 2\,\bar{W}_2 + \bar{W}_3 + 2\,(\bar{W}_2+\bar{W}_3)\operatorname{tr}\mathbf{E}\right] - 2\,\mathbf{E}\,(\bar{W}_2+\bar{W}_3)\\ &+ \mathbf{m}_1\otimes\mathbf{m}_1\,(\bar{W}_4 + 2\,\bar{W}_5) + (\mathbf{E}\,\mathbf{m}_1\otimes\mathbf{m}_1 + \mathbf{m}_1\otimes\mathbf{E}\,\mathbf{m}_1)\,2\,\bar{W}_5\\ &+ \mathbf{m}_2\otimes\mathbf{m}_2\,(\bar{W}_6 + 2\,\bar{W}_7) + (\mathbf{E}\,\mathbf{m}_2\otimes\mathbf{m}_2 + \mathbf{m}_2\otimes\mathbf{E}\,\mathbf{m}_2)\,2\,\bar{W}_7\Big\} + o(\mathbf{E})\,.\end{aligned} \tag{A.8}$$

Then, we write $\bar{W}_i(I_1, I_2, ..., I_7) = \bar{W}_i(\mathbf{C})$, $i = 1, 2, ..., 7$, and linearize $\bar{W}_i(\mathbf{C})$. We obtain

$$\bar{W}_i(\mathbf{C}) = \bar{W}(\mathbf{I}+2\,\mathbf{E}) = \bar{W}_i(\mathbf{I}) + \frac{\partial\,\bar{W}_i(\mathbf{C})}{\partial\mathbf{C}}\Big|_{\mathbf{C}=\mathbf{I}}\cdot 2\,\mathbf{E} + o(\mathbf{E})\,, \tag{A.9}$$

$$\begin{aligned}\frac{\partial\,\bar{W}_i}{\partial\mathbf{C}}\Big|_{\mathbf{C}=\mathbf{I}} &= \left(\sum_{j=1}^{7}\frac{\partial\,\bar{W}_i}{\partial I_j}\,\frac{\partial\,I_j}{\partial\mathbf{C}}\right)\Big|_{\mathbf{C}=\mathbf{I}} = \left(\sum_{j=1}^{7}\bar{W}_{ij}\,\frac{\partial\,I_j}{\partial\mathbf{C}}\right)\Big|_{\mathbf{C}=\mathbf{I}}\\ &= (\mathring{W}_{i1} + 2\,\mathring{W}_{i2} + \mathring{W}_{i3})\,\mathbf{I} + (\mathring{W}_{i4} + 2\,\mathring{W}_{i5})\,\mathbf{m}_1\otimes\mathbf{m}_1\\ &\quad + (\mathring{W}_{i6} + 2\,\mathring{W}_{i7})\,\mathbf{m}_2\otimes\mathbf{m}_2\,,\end{aligned} \tag{A.10}$$

where $\mathring{W}_i \triangleq \bar{W}_i(\mathbf{I})$ and $\mathring{W}_{ij} \triangleq \bar{W}_{ij}(\mathbf{I})$, $i,k = 1,2,...,7$. In addition, to obtain (A.10), we used the relations

$$\begin{aligned}
&\frac{\partial I_1}{\partial \mathbf{C}}\Big|_{\mathbf{C}=\mathbf{I}} = \mathbf{I}\,, \qquad\qquad \frac{\partial I_2}{\partial \mathbf{C}}\Big|_{\mathbf{C}=\mathbf{I}} = (I_1\,\mathbf{I} - \mathbf{C})\,\Big|_{\mathbf{C}=\mathbf{I}} = 2\,\mathbf{I}\,,\\
&\frac{\partial I_3}{\partial \mathbf{C}}\Big|_{\mathbf{C}=\mathbf{I}} = \left(I_3\,\mathbf{C}^{-1}\right)\Big|_{\mathbf{C}=\mathbf{I}} = \mathbf{I}\,,\\
&\frac{\partial I_4}{\partial \mathbf{C}}\Big|_{\mathbf{C}=\mathbf{I}} = \mathbf{m}_1 \otimes \mathbf{m}_1\,, \qquad \frac{\partial I_6}{\partial \mathbf{C}}\Big|_{\mathbf{C}=\mathbf{I}} = \mathbf{m}_2 \otimes \mathbf{m}_2\,,\\
&\frac{\partial I_5}{\partial \mathbf{C}}\Big|_{\mathbf{C}=\mathbf{I}} = (\mathbf{C}\mathbf{m}_1 \otimes \mathbf{m}_1 + \mathbf{m}_1 \otimes \mathbf{C}\mathbf{m}_1)\,\Big|_{\mathbf{C}=\mathbf{I}} = 2\,\mathbf{m}_1 \otimes \mathbf{m}_1\,,\\
&\frac{\partial I_7}{\partial \mathbf{C}}\Big|_{\mathbf{C}=\mathbf{I}} = (\mathbf{C}\mathbf{m}_2 \otimes \mathbf{m}_2 + \mathbf{m}_2 \otimes \mathbf{C}\mathbf{m}_2)\,\Big|_{\mathbf{C}=\mathbf{I}} = 2\,\mathbf{m}_2 \otimes \mathbf{m}_2\,.
\end{aligned} \tag{A.11}$$

Next, we use (A.9)-(A.10), (3.58), $\bar{W}_{ij} = \bar{W}_{ji}$, $i,j = 1,2,...,7$, and $\mathbf{E}\cdot\mathbf{I} = \operatorname{tr}\mathbf{E}$ to rewrite some of the terms in (A.8) as

$$\begin{aligned}
\bar{W}_1 + 2\,\bar{W}_2 + \bar{W}_3 = {}& 2\operatorname{tr}\mathbf{E}\,(\mathring{W}_{11} + 4\,\mathring{W}_{22} + \mathring{W}_{33} + 4\,\mathring{W}_{12} + 2\,\mathring{W}_{13} + 4\,\mathring{W}_{23})\\
&+ 2\,\mathbf{m}_1\cdot\mathbf{E}\,\mathbf{m}_1\,(\mathring{W}_{14} + 2\,\mathring{W}_{15} + 2\,\mathring{W}_{24} + 4\,\mathring{W}_{25} + \mathring{W}_{34} + 2\,\mathring{W}_{35})\\
&+ 2\,\mathbf{m}_2\cdot\mathbf{E}\,\mathbf{m}_2\,(\mathring{W}_{16} + 2\,\mathring{W}_{17} + 2\,\mathring{W}_{26} + 4\,\mathring{W}_{27} + \mathring{W}_{36} + 2\,\mathring{W}_{37})\\
&+ o(\mathbf{E})\,,
\end{aligned} \tag{A.12}$$

$$\begin{aligned}
\bar{W}_4 + 2\,\bar{W}_5 = {}& 2\operatorname{tr}\mathbf{E}\,(\mathring{W}_{14} + 2\,\mathring{W}_{24} + \mathring{W}_{34} + 2\,\mathring{W}_{15} + 4\,\mathring{W}_{25} + 2\,\mathring{W}_{35})\\
&+ 2\,\mathbf{m}_1\cdot\mathbf{E}\,\mathbf{m}_1\,(\mathring{W}_{44} + 4\,\mathring{W}_{55} + 4\,\mathring{W}_{45})\\
&+ 2\,\mathbf{m}_2\cdot\mathbf{E}\,\mathbf{m}_2\,(\mathring{W}_{46} + 2\,\mathring{W}_{47} + 2\,\mathring{W}_{56} + 4\,\mathring{W}_{57}) + o(\mathbf{E})\,,
\end{aligned} \tag{A.13}$$

$$\begin{aligned}
\bar{W}_6 + 2\,\bar{W}_7 = {}& 2\operatorname{tr}\mathbf{E}\,(\mathring{W}_{16} + 2\,\mathring{W}_{26} + \mathring{W}_{36} + 2\,\mathring{W}_{17} + 4\,\mathring{W}_{27} + 2\,\mathring{W}_{37})\\
&+ 2\,\mathbf{m}_1\cdot\mathbf{E}\,\mathbf{m}_1\,(\mathring{W}_{46} + 2\,\mathring{W}_{47} + 2\,\mathring{W}_{56} + 4\,\mathring{W}_{57})\\
&+ 2\,\mathbf{m}_2\cdot\mathbf{E}\,\mathbf{m}_2\,(\mathring{W}_{66} + 4\,\mathring{W}_{77} + 4\,\mathring{W}_{67}) + o(\mathbf{E})\,,
\end{aligned} \tag{A.14}$$

$$\bar{W}_2 + \bar{W}_3 = \mathring{W}_2 + \mathring{W}_3 + O(\mathbf{E})\,, \qquad \bar{W}_5 = \mathring{W}_5 + O(\mathbf{E})\,, \qquad \bar{W}_5 = \mathring{W}_5 + O(\mathbf{E})\,, \tag{A.15}$$

Substituting (A.12)-(A.15) into (A.8) yields (3.59).

APPENDIX B – DERIVATION OF THE TERMS IN $\delta\mathcal{E}_a$

We derive the expressions (3.107) for $\delta\mathcal{E}_a^W$, (3.108) for δT , and (3.109) for δB, which are used in (3.102) to evaluate $\delta\mathcal{E}_a$. Let us first determine the variation of a functional G having the form

$$G = G(\mathbf{f}, \lambda) \triangleq \int_{\mathcal{B}} g(\mathbf{x}, \mathbf{f}, \nabla\mathbf{f}, \lambda)\, \mathrm{d}\mathbf{x}\,. \tag{B.1}$$

Later, we determine $\partial\mathcal{E}_a^W$, δT, and ∂B by taking particular expressions for g in (B.1).

We use the admissible fields given by (3.101) to obtain

$$\begin{aligned}
\Delta G \triangleq G(\mathbf{f}^*, \lambda^*) - G(\mathbf{f}, \lambda) &= \int_{\mathcal{B}^*} g(\mathbf{x}^*, \mathbf{f}^*, \nabla^*\mathbf{f}^*, \lambda^*)\, \mathrm{d}\mathbf{x}^* - \int_{\mathcal{B}} g(\mathbf{x}, \mathbf{f}, \nabla\mathbf{f}, \lambda)\, \mathrm{d}\mathbf{x} \\
&= \int_{\mathcal{B}} \left[g(\mathbf{x} + \delta\mathbf{x}, \mathbf{f} + \delta\mathbf{f}, \nabla\mathbf{f} + \delta\nabla\mathbf{f}, \lambda + \delta\lambda)\, \det(\mathbf{I} + \nabla\delta\mathbf{x}) - g(\mathbf{x}, \mathbf{f}, \nabla\mathbf{f}, \lambda)\right] \mathrm{d}\mathbf{x} \\
&\sim \int_{\mathcal{B}} \left[g(\mathbf{x} + \delta\mathbf{x}, \mathbf{f} + \delta\mathbf{f}, \nabla\mathbf{f} + \delta\nabla\mathbf{f}, \lambda + \delta\lambda)\, (1 + \mathrm{Div}\, \delta\mathbf{x}) - g(\mathbf{x}, \mathbf{f}, \nabla\mathbf{f}, \lambda)\right] \mathrm{d}\mathbf{x}\,,
\end{aligned} \tag{B.2}$$

where ∇^* denotes the gradient with respect to $\mathbf{x}^*$, $\mathcal{B}^* = \mathbf{x}^*(\mathcal{B})$, and $\sim$ denotes equality except for terms of order greater than one relative to $\delta\mathbf{f}$, $\delta\lambda$, or $\delta\mathbf{x}$.

Now, let $\overline{\delta\mathbf{f}}(\mathbf{x}) \triangleq \mathbf{f}^*(\mathbf{x}) - \mathbf{f}(\mathbf{x})$ and $\overline{\delta\lambda}(\mathbf{x}) \triangleq \lambda^*(\mathbf{x}) - \lambda(\mathbf{x})$, then it is possible to verify that, (Gelfand; Fomin, 1963),

$$\delta\mathbf{f} \sim \overline{\delta\mathbf{f}} + \nabla\mathbf{f}\, \delta\mathbf{x}\,, \qquad \delta\nabla\mathbf{f} \sim \nabla\overline{\delta\mathbf{f}} + (\nabla\nabla\mathbf{f})\, \delta\mathbf{x}\,, \qquad \delta\lambda \sim \overline{\delta\lambda} + \nabla\lambda \cdot \delta\mathbf{x}\,. \tag{B.3}$$

Using Taylor's theorem and (B.3) to expand the first term of the integrand in (B.2) and keeping only terms that are linear with respect to $\delta\mathbf{f}$, $\delta\lambda$, and $\delta\mathbf{x}$, we obtain the first variation of G as

$$\begin{aligned}
\delta G &= \int_{\mathcal{B}} \left[\frac{\partial g}{\partial \mathbf{x}} \cdot \delta\mathbf{x} + \frac{\partial g}{\partial \mathbf{f}} \cdot \delta\mathbf{f} + \frac{\partial g}{\partial \nabla\mathbf{f}} \cdot \delta\nabla\mathbf{f} + \frac{\partial g}{\partial \lambda}\, \delta\lambda + g\, \mathrm{Div}\, \delta\mathbf{x}\right] \mathrm{d}\mathbf{x}\,, \\
&= \int_{\mathcal{B}} \left[\frac{\partial g}{\partial \mathbf{x}} \cdot \delta\mathbf{x} + \frac{\partial g}{\partial \mathbf{f}} \cdot (\overline{\delta\mathbf{f}} + \nabla\mathbf{f}\, \delta\mathbf{x}) + \frac{\partial g}{\partial \nabla\mathbf{f}} \cdot (\nabla\overline{\delta\mathbf{f}} + \nabla\nabla\mathbf{f}\, \delta\mathbf{x})\right. \\
&\qquad \left. + \frac{\partial g}{\partial \lambda}\, (\overline{\delta\lambda} + \nabla\lambda \cdot \delta\mathbf{x}) + g\, \mathrm{Div}\, \delta\mathbf{x}\right] \mathrm{d}\mathbf{x}\,,
\end{aligned} \tag{B.4}$$

where $g \equiv g(\mathbf{x}, \mathbf{f}, \nabla\mathbf{f}, \lambda)$. Then, we use the relations, (Gurtin, 1982),

$$\begin{aligned}
&\frac{\partial g}{\partial \mathbf{x}} \cdot \delta\mathbf{x} + \frac{\partial g}{\partial \mathbf{f}} \cdot (\nabla\mathbf{f}\, \delta\mathbf{x}) + \frac{\partial g}{\partial \nabla\mathbf{f}} \cdot (\nabla\nabla\mathbf{f}\, \delta\mathbf{x}) + \frac{\partial g}{\partial \lambda}\, (\nabla\lambda \cdot \delta\mathbf{x}) \\
&= \nabla g \cdot \delta\mathbf{x} = \mathrm{Div}\, (g\, \delta\mathbf{x}) - g\, \mathrm{Div}\, \delta\mathbf{x}\,,
\end{aligned} \tag{B.5}$$

$$\frac{\partial g}{\partial \nabla\mathbf{f}} \cdot \nabla\overline{\delta\mathbf{f}} = \mathrm{Div} \left[\left(\frac{\partial g}{\partial \nabla\mathbf{f}}\right)^T \overline{\delta\mathbf{f}}\right] - \overline{\delta\mathbf{f}} \cdot \mathrm{Div} \left(\frac{\partial g}{\partial \nabla\mathbf{f}}\right), \tag{B.6}$$

to rewrite (B.4) as

$$\begin{aligned}\delta G = \int_{\mathcal{B}} \Bigg\{ \mathrm{Div}\left[\left(\frac{\partial g}{\partial \nabla \mathbf{f}}\right)^T \overline{\delta \mathbf{f}} + g\,\delta \mathbf{x}\right] \\ - \overline{\delta \mathbf{f}} \cdot \left[\mathrm{Div}\left(\frac{\partial g}{\partial \nabla \mathbf{f}}\right) - \frac{\partial g}{\partial \mathbf{f}}\right] + \frac{\partial g}{\partial \lambda}\,\overline{\delta \lambda}\Bigg\}\,\mathrm{d}\mathbf{x}\,.\end{aligned} \tag{B.7}$$

Except for the term involving λ, (B.7) is similar to the expression presented by Gelfand and Fomin (1963), who considered g depending only on $\mathbf{x}$, $\mathbf{f}$, and $\nabla \mathbf{f}$.

Using (B.7) with $g = W_a$, $g = -p \det \mathbf{F}$, and $g = \mathbf{b} \cdot \mathbf{f}$ we obtain, respectively, $\delta \mathcal{E}_a^W$, δT for the pressure load, and δB as presented in (3.103)-(3.106). The expression of δT for the dead load is classical since T does not depend on λ and $\delta \mathbf{x} = 0$ on $\partial \mathcal{B}$, so that $\mathbf{x}^*(\mathbf{x}) = \mathbf{x}$ on $\partial \mathcal{B}$. For convenience, the expressions (3.103)-(3.106) are reproduced below

$$\delta \mathcal{E}_a^W = \int_{\mathcal{B}} \left[\mathrm{Div}\left(\frac{\partial {W_a}}{\partial \mathbf{F}}^T \overline{\delta \mathbf{f}} + W_a\,\delta \mathbf{x}\right) - \overline{\delta \mathbf{f}} \cdot \mathrm{Div}\left(\frac{\partial W_a}{\partial \mathbf{F}}\right) + \frac{\partial W_a}{\partial \lambda}\,\overline{\delta \lambda}\right] \mathrm{d}\mathbf{x}, \tag{3.103}$$

$$\delta T = \begin{cases} \int_{\partial_2 \mathcal{B}} \mathbf{t} \cdot \delta \mathbf{f}\,\mathrm{d}\mathbf{x}\,, & \text{(dead load)}\,, \\ -p \int_{\mathcal{B}} \left[\mathrm{Div}\left(\frac{\partial {J}}{\partial \mathbf{F}}^T \overline{\delta \mathbf{f}} + J\,\delta \mathbf{x}\right) - \overline{\delta \mathbf{f}} \cdot \mathrm{Div}\left(\frac{\partial J}{\partial \mathbf{F}}\right)\right] \mathrm{d}\mathbf{x}\,, & \text{(pressure load)}\,, \end{cases} \tag{3.104}$$

$$\delta B = \int_{\mathcal{B}} \left\{\mathrm{Div}\left[(\mathbf{b} \cdot \mathbf{f})\,\delta \mathbf{x}\right] + \mathbf{b} \cdot \overline{\delta \mathbf{f}}\right\} \mathrm{d}\mathbf{x}\,, \tag{3.105}$$

$$\overline{\delta \mathbf{f}} = \delta \mathbf{f} - \mathbf{F}\,\delta \mathbf{x}\,, \qquad \overline{\delta \lambda} = \delta \lambda - \nabla \lambda \cdot \delta \mathbf{x}\,, \tag{3.106}$$

where, as before, $J = \det \mathbf{F}$.

Let us now obtain (3.107)-(3.109) by considering $\delta \mathcal{E}_a^W$, δT, and δB separately. For $\delta \mathcal{E}_a^W$, we apply the divergence theorem in (3.103) and use both (3.110) and $\partial W_a / \partial \lambda = c$ to write

$$\begin{aligned}\delta \mathcal{E}_a^W = &\int_{\Sigma \cup \mathcal{S}} [\mathbf{P}_a^T\,\overline{\delta \mathbf{f}} + W_a\,\delta \mathbf{x}]_+^- \cdot \mathbf{N}\,\mathrm{d}A + \int_{\partial \mathcal{B}} (\mathbf{P}_a^T\,\overline{\delta \mathbf{f}} + W_a\,\delta \mathbf{x}) \cdot \mathbf{N}\,\mathrm{d}A \\ &+ \int_{\mathcal{B}} \left[-\overline{\delta \mathbf{f}} \cdot \mathrm{Div}\,\mathbf{P}_a + c\,\overline{\delta \lambda}\right] \mathrm{d}\mathbf{x}\,,\end{aligned} \tag{B.8}$$

where the integral on Σ and $\mathcal{S}$ appears due to the discontinuity of $\mathbf{F}$. Substituting (3.106) into (B.8) and recalling that $\delta \mathbf{f} = \mathbf{0}$ on $\partial_1 \mathcal{B}$ and $\delta \mathbf{x} = \mathbf{0}$ on $\partial \mathcal{B}$, we obtain

$$\begin{aligned}\delta \mathcal{E}_a^W = &\int_{\Sigma \cup \mathcal{S}} \left\{\delta \mathbf{f} \cdot [\mathbf{P}_a]_+^- \mathbf{N} + \delta \mathbf{x} \cdot \left[W\,\mathbf{N} + \mathbf{F}^T\,\mathbf{P}_a\,\mathbf{N}\right]_+^-\right\} \mathrm{d}A \\ &+ \int_{\partial_2 \mathcal{B}} \delta \mathbf{f} \cdot \mathbf{P}_a\,\mathbf{N}\,\mathrm{d}A \\ &+ \int_{\mathcal{B}} \left[-\left(\delta \mathbf{f} \cdot \mathrm{Div}\,\mathbf{P}_a - \delta \mathbf{x} \cdot \mathbf{F}^T\,\mathrm{Div}\,\mathbf{P}_a\right) + c\,(\delta \lambda - \nabla \lambda \cdot \delta \mathbf{x})\right] \mathrm{d}\mathbf{x}\,.\end{aligned} \tag{B.9}$$

Then, we use $\mathcal{B} = \mathcal{B}_= \cup \mathcal{B}_>$, $c = 0$ in $\mathcal{B}_=$, and both $\delta \lambda = 0$ and $\nabla \lambda = 0$ in $\mathcal{B}_>$ to obtain (3.107).

For δT, we apply the divergence theorem in (3.104) and use $\partial J/\partial \mathbf{F} = \operatorname{cof} \mathbf{F}$ to rewrite δT as

$$\begin{aligned}\delta T = -p \Bigg\{ & \int_{\Sigma \cup \mathcal{S}} \left[(\operatorname{cof} \mathbf{F})^T \, \overline{\delta \mathbf{f}} + J \, \delta \mathbf{x} \right]_+^- \cdot \mathbf{N} \, \mathrm{d}A \\ & + \int_{\partial \mathcal{B}} \left[(\operatorname{cof} \mathbf{F})^T \, \overline{\delta \mathbf{f}} + J \, \delta \mathbf{x} \right] \cdot \mathbf{N} \, \mathrm{d}A + \int_{\mathcal{B}} \left[-\overline{\delta \mathbf{f}} \cdot \operatorname{Div} (\operatorname{cof} \mathbf{F}) \right] \mathrm{d}\mathbf{x} \Bigg\} .\end{aligned} \tag{B.10}$$

We substitute (3.106.a) into (B.10) and use the Piola's identity $\operatorname{Div} (\operatorname{cof} \mathbf{F}) = \mathbf{0}$ together with $\delta \mathbf{f} = \mathbf{0}$ on $\partial_1 \mathcal{B}$ and $\delta \mathbf{x} = \mathbf{0}$ on $\partial \mathcal{B}$ to find that

$$\begin{aligned}\delta T = & - p \int_{\Sigma \cup \mathcal{S}} \left[(\operatorname{cof} \mathbf{F})^T \, \delta \mathbf{f} - (\operatorname{cof} \mathbf{F})^T \, \mathbf{F} \delta \mathbf{x} + J \, \delta \mathbf{x} \right]_+^- \cdot \mathbf{N} \, \mathrm{d}A \\ & - p \int_{\partial_2 \mathcal{B}} \delta \mathbf{f} \cdot \operatorname{cof} \mathbf{F} \, \mathbf{N} \, \mathrm{d}A \, .\end{aligned} \tag{B.11}$$

Then, since $\operatorname{cof} \mathbf{F} \triangleq J \, \mathbf{F}^{-T}$, we have that $(\operatorname{cof} \mathbf{F})^T \mathbf{F} \, \delta \mathbf{x} = J \, \delta \mathbf{x}$ and, thus, (B.11) yields (3.108).

Finally, for δB, we apply the divergence theorem in (3.105) to find that

$$\delta B = \int_{\partial \mathcal{B}} (\mathbf{b} \cdot \mathbf{f}) \, \delta \mathbf{x} \cdot \mathbf{N} \, \mathrm{d}A + \int_{\mathcal{B}} \mathbf{b} \cdot \overline{\delta \mathbf{f}} \, \mathrm{d}\mathbf{x} \, , \tag{B.12}$$

where we used the continuity of $\mathbf{f}$ and $\mathbf{b}$. Then, (3.109) follows from (B.12) by using (3.106.a) and $\delta \mathbf{x} = \mathbf{0}$ on $\partial \mathcal{B}$.

APPENDIX C – STANDARD NUMERICAL PROCEDURE

We use a standard numerical procedure to try solving the disk MP defined in Section 4.1. This minimization problem can be written in a discrete form as

$$\min_{\mathbf{s}\in\mathbb{R}^m} \mathcal{F}(\mathbf{s})\,, \qquad \mathcal{F}(\mathbf{s}) = \mathcal{E}_h(\mathbf{s})\,, \tag{C.1}$$

where, recalling from Section 4.4.1, $\mathbf{s} = (s_1, s_2, ..., s_m)$ is related to the approximated minimizer $\mathbf{u}_h$ of the disk MP by (4.47) and $\mathcal{E}_h(\mathbf{s}) \triangleq \check{\mathcal{E}}(u_h)$, where $\check{\mathcal{E}}$ is given by (4.12).

We solve the minimization problem (C.1) using the Newton-Raphson method with a unidirectional search as explained in Section 4.4.1 to solve the inner problem in (4.51). We refer to this procedure as the *standard numerical procedure* because it does not formulate the disk MP as a bi-level minimization problem like we do in Section 4.4.1. Here, we consider only the orthotropic St Venant-Kirchhoff material and use the same meshes and geometrical, material, and numerical parameters used in Section 4.4.2. Recall from this section that the deformation field is non-smooth for $p > \bar{p} = 0.013773$.

For $p = 0.005 < \bar{p}$ and $p = \bar{p}$, we have verified that, as the mesh is refined, the approximate solutions obtained by the standard numerical procedure converge to the smooth solution predicted in Section 4.3.2. For $p > \bar{p}$, however, the approximate solutions do not converge to the non-smooth solution predicted in that section. Recall from there that the non-smooth solution has a jump discontinuity in its derivative. We comment on the non-convergent results below.

In Figures 20 and 21, we show ν and P_{rr}, respectively, versus the radius R in a vicinity of the inner surface of the disk for $p = 0.05 > \bar{p}$ using different meshes. This is the same pressure p used to obtain the numerical results presented in Section 4.4.2. Recall from Section 4.3.2 that a non-smooth solution is expected in this case, which has a jump discontinuity in its derivative. We see from Figure 20 that this jump occurs near the radius $R = 0.003$. Away from this radius, the curves are smooth and similar to each other. Near this radius, however, ν oscillates. We have verified that the discriminant $D(\tau, P_{rr})$, given by (4.42), is positive and close to zero near $R = 0.003$. Therefore, the oscillations occur in an interval where the corresponding point (τ, P_{rr}) belongs to $\mathcal{D}_>$ and is close to the interface with $\mathcal{D}_<$. In addition, it is clear from Figure 20 that the jumps in ν do not satisfy (4.33), which means that these numerical results do not correspond to minimizers of the total potential energy. In spite of the oscillations of ν, observe from Figure 21 that P_{rr} is continuous for all considered meshes, which means that the traction continuity condition (4.29) is satisfied.

The reason for this oscillatory behavior is not clear. In Section 3.4, we have seen that the traction continuity and the dissipation-free conditions, given by, respectively,

Figure 20 – Radial stretch ν versus radius R using $q = 4, 6, 8, 10$.

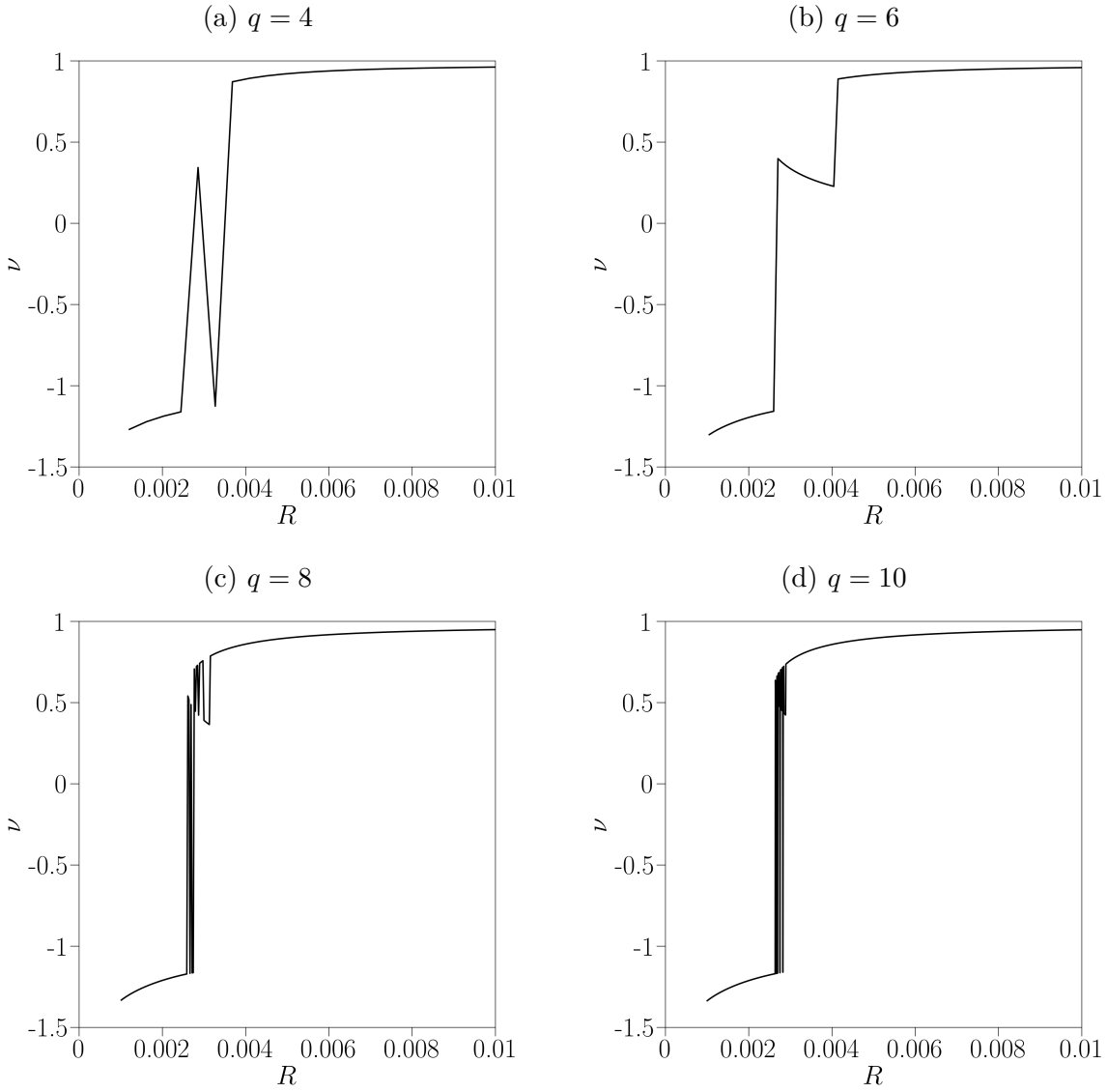

Source: The author.

(3.87) and (3.88), are necessary conditions for a deformation field to be a minimizer of the total potential energy. Recall from Section 3.4 that the traction continuity condition (3.87), which corresponds to (4.29) in the disk problem, can be found by perturbing the minimizer of the energy functional while holding $\mathcal{S}$ fixed, whereas (3.88), which yields (4.33) in the disk problem, is found by perturbing $\mathcal{S}$. This motivated the inclusion of the radius $R_{\mathcal{S}}$ of the surface $\mathcal{S}$, which, recalling from Section 4.2.2, is cylindrical in the disk problem, as a variable of the numerical procedure presented in Section 4.4.1.

Figure 21 – Radial normal stress P_{rr} versus radius R using $q = 4, 6, 8, 10$.

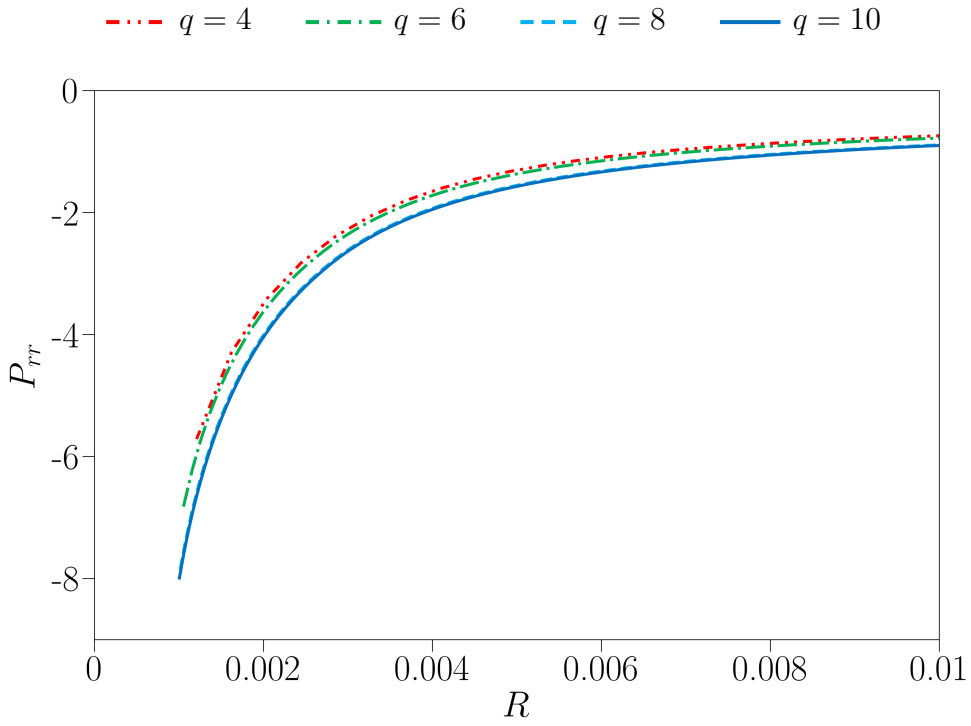

Source: The author.


EESC • USP